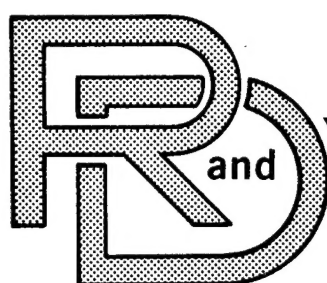


3013

TECHNICAL LIBRARY
REFERENCE COPY

701



CENTER

LABORATORY

TECHNICAL REPORT

NO. 12583

20010820 002



FAILURE OF TANK TRACK PADS,
INVESTIGATION INTO THE
TECHNICAL REPORT FOR FY-79 AND FY-80

Department of Army Project Number 1L161102AF22

October 29, 1980

by Lawrence Livermore National Laboratory
Livermore, California

Reproduced From
Best Available Copy

Approved for Public Release,
Distribution Unlimited

U.S. ARMY TANK-AUTOMOTIVE COMMAND
RESEARCH AND DEVELOPMENT CENTER
Warren, Michigan 48090

AN 44682
1-44762

UNCLASSIFIED

SECURITY CLASSIFICATION OF THIS PAGE (When Data Entered)

REPORT DOCUMENTATION PAGE		READ INSTRUCTIONS BEFORE COMPLETING FORM
1. REPORT NUMBER 12583	2. GOVT ACCESSION NO.	3. RECIPIENT'S CATALOG NUMBER
4. TITLE (and Subtitle) INVESTIGATION INTO THE FAILURE OF TANK TRACK PADS- TECHNICAL REPORT FOR FY-79 AND FY-80		5. TYPE OF REPORT & PERIOD COVERED FINAL REPORT October 1978 - October 1980
		6. PERFORMING ORG. REPORT NUMBER UCID 19035
7. AUTHOR(s) D. R. Lesuer, M. Zaslowsky, S. V. Kulkarni, R. H. Cornell, D. M. Hoffman		8. CONTRACT OR GRANT NUMBER(s) 1L161102AF22
9. PERFORMING ORGANIZATION NAME AND ADDRESS Lawrence Livermore National Laboratory P.O. Box 808, Livermore, California 94550		10. PROGRAM ELEMENT, PROJECT, TASK AREA & WORK UNIT NUMBERS
11. CONTROLLING OFFICE NAME AND ADDRESS U.S. Army Tank-Automotive Command Research and Development Center Warren, Michigan 48090		12. REPORT DATE October 29, 1980
14. MONITORING AGENCY NAME & ADDRESS (if different from Controlling Office)		13. NUMBER OF PAGES 133
		15. SECURITY CLASS. (of this report)
		15a. DECLASSIFICATION/DOWNGRADING SCHEDULE
16. DISTRIBUTION STATEMENT (of this Report) Approved for Public Release, Distribution Unlimited		
17. DISTRIBUTION STATEMENT (of the abstract entered in Block 20, if different from Report)		
18. SUPPLEMENTARY NOTES		
19. KEY WORDS (Continue on reverse side if necessary and identify by block number) Track pads Tank track Styrene Butadiene Rubber Hysteretic Heat Generation		
20. ABSTRACT (Continue on reverse side if necessary and identify by block number) This report describes a two-year study into the failure of tank track pads. Emphasis here is primarily on pads associated with the T-142 track. Temperature was recognized as an important parameter, and a thermal model has been developed which employs a finite element thermal analysis code at LLNL. The model involves a plane section of T-142 track and utilizes convective boundary conditions. The model does an excellent job of predicting temperature data obtained in the field on the T-142 track. The maximum predicted temperature at the center of the pad after 6,000 s (1.67 hr.) of continuous operation is		

BLOCK 20:

132°C (270°F).

The structural response of the pad to the loading provided by the tank has also been analyzed using a mechanical model which includes a section of T-142 track, a roadwheel, and supporting terrain. The output of the model has been presented in the form of stress contour plots showing the normal stress and effective stress generated in the pad.

Field data relevant to the problem has been collected at the Yuma Proving Grounds. Surface and internal pad temperatures have been measured on an M-103 tank as a function of running time and pad manufacturer.

Experimental work has also been done to assess crack growth, fatigue strength, and residual tear strength after fatigue. In addition, material properties required for the structural and thermal models were evaluated. We also examined the changes in physical properties and chemical characteristics brought about by running pads on a tank at the Yuma Proving Grounds. The thermal diffusivity was observed to decrease by about 20% due to field testing, while the tear strength decreased between 20% and 30% depending upon the terrain.

TABLE OF CONTENTS

	<u>Page</u>
List of Tables.	3
List of Figures	4-7
Executive Summary8-10
1. INTRODUCTION.	11
1-1. Scope of the Problem.	11
1-2. FY 79 Work.	13
1-3. FY 80 Work.	14
2. FY 79 REPORT.	15
2-1. Temperature Analysis.	15
2-1. Structural Analysis	35
2-3. Materials Characterization.	36
2-4. Failure Studies	50
3. FY 80 ACTIVITIES.	59
3-1. Field Analysis.	59
3-2. Analytical Work	69
3-3. Experimental Work	107
REFERENCES.	127
APPENDIX A.	128
APPENDIX B.	133

LIST OF TABLES

<u>Table No.</u>	<u>Caption</u>	<u>Page No.</u>
1	Hysteric Heat Generation Rate for T-142 Shoe.	16
	as a Function of Tank Speed	
2	Thermal Conductivity for SBR From Vender A.	18
3	Specific Heat for SBR From Vender A	19
4	Carbon Black in SBR from Vender A	41
5	Thermogravimetric Analysis of SBR From Vender A	44
6	ASTM D624-73 Tear Test Results for Shoe No. 1	47
7	Residual Tear Test Results (Room Temperature 24°C).	60
8	Test Schedule	67
9	Heat Capacity For SBR From Vendor B	75
10	Thermal Conductivity For SBR From Vender B.	76
11	Temperature Differences Between Model Predictions	84
	And Field Data	
12	Shear Relaxation Modulus Parameters	100
13	Concentration of Nonmetals As Percent By Weight	109
14	Concentration of Metals (As PPM).	110
	In New Tank Tread Rubbers	
	From Different Manufacturers	
15	Extractables, Styrene Content in SBR's and Molecular.	111
	Weights Between Crosslinks in New Tank Tread Rubbers from	
	Various Manufacturers	
16	Absorption Peak Assignments For Infrared Spectra.	117
	of Pyrolyzates of Treads	
17	Constituents in the Chloroform-Acetone Extract.	118-120
	Identified by GC-MS	
18	Effect of Field Testing on Density of Tank Tread SBR.	122
19	Effect of Field Testing on the Thermal Diffusivity.	123
	of Tank Tread SBR	
20	Tear Resistance of Field Tested Pads Testing Temperature. . .	125
	22°C	
21	Tear Resistance of Field Tested Pads Testing Temperature. . .	126
	204°C	

LIST OF FIGURES

		<u>Page No.</u>
Figure 1	The T-142 tank track shoe and relevant sections of track.	12
Figure 2	Flow diagram showing codes and post processors used in this study. The outputs generated are indicated in the diagram.	20
Figure 3	Finite element mesh used in the FY 79 TACO and NIKE2D analyses. Mesh represents a plane section of T-142 track including the pad and supporting terrain.	23
Figure 4	Outline of finite element mesh showing different materials used in the analysis.	24
Figure 5	Surfaces held to constant temperature in the FY 79 thermal model.	25
Figure 6	Temperature-time response for point 1 within the tank track pad. Boundary conditions are shown in Figure 5.	26
Figure 7	Temperature-time response for point 2 within the tank track pad. Boundary conditions are shown in Figure 5.	27
Figure 8	Temperature-time response for central point at the surface of the tank track pad. Boundary conditions are shown in Figure 5.	28
Figure 9	Contours of constant temperature after 2000 s (0.56 hr) at 32 km/hr (20 MPH) as predicted using the boundary conditions shown in Figure 5.	29
Figure 10	Contours of constant temperature after 4000 s (1.11 hr) at 32 km/hr (20 MPH) as predicted using the boundary conditions shown in Figure 5.	30
Figure 11	Contours of constant temperature after 6000 s (1.67 hr) at 32 km/hr (20 MPH) as predicted using the boundary conditions shown in Figure 5.	31
Figure 12	Temperature profile across the pad from the supporting terrain to the steel backing plate. Profile is for pad after 2000 s (0.56 hr) at 32 km/hr (20 MPH).	32
Figure 13	Temperature profile across pad after 4,000 s (1.11 hr).	33
Figure 14	Temperature profile across pad after 6,000 s (1.67 hr).	34
Figure 15-1	Three element standard linear solid used in the viscoelastic material model contained in NIKE2D.	37

	<u>Page No.</u>
Figure 15-2 Relaxation behavior of the shear modulus as predicted by the model in 15-1. The curve can be described by the equation shown.	37
Figure 16 Storage modulus (G'), loss modulus (G''), and tan delta (δ) plotted versus temperature (-150°C to 50°C). Data determined in low strain torsion experiments.	38
Figure 17 Storage modulus (G'), loss modulus (G''), and tan delta (δ) plotted versus temperature (40°C to 220°C). Data determined in low strain torsion experiments.	39
Figure 18 Bulk modulus of SBR as a function of temperature.	40
Figure 19 TGA plot showing percent weight lost by a sample of SBR as a function of temperature.	43
Figure 20 Sample used in tear resistance tests. Sample is per ASTM D-624-73 Die C.	45
Figure 21 Photograph of typical tear test fractures. Static fractures are shown in (a) while a fatigue fracture is shown in (b).	48
Figure 22 Cube with implanted, oriented cracks used in compression-compression fatigue crack growth tests. Relevant parameters and results are indicated.	51
Figure 23 Photograph of cube used in fatigue crack growth experiments. Cracks were implanted in all six faces.	52
Figure 24 Tear specimen and thermocouple used in tension-tension fatigue tests.	54
Figure 25 Fatigue strength versus number of cycles to failure for two different shoes from Vender A. A tear specimen was used and its temperature is indicated in parentheses.	55
Figure 26 Temperature versus time curve for a tear sample cycled to $s = 0.57$.	56
Figure 27-1 Fracture surface of static loaded tear specimen.	57
Figure 27-2 Fracture surface of fatigue loaded tear specimen.	58
Figure 28 Thermocouple injector for internal pad temperature measurements in the field.	62
Figure 29 Thermocouple calibration pad section.	63
Figure 30 Internal temperature measurement errors.	64
Figure 31 Surface temperature measurement errors.	65

Figure 32	Internal and surface temperature versus time for pads from Vender C tested at the Yuma Proving Grounds.	68
Figure 33	Pad wear observations for T-142 tank track.	70
Figure 34	Load-displacement data for compression-compression fatigue test between the stress levels of 0.18 MPa (26 psi) and 2.1 MPa (305 psi) at a frequency of 2 Hz.	72
Figure 35	Schematic temperature-time curve illustrating determination of Q from the local temperature use at $t = 0$ seconds.	73
Figure 36	Finite element computer mesh used in the FY 80 thermal model.	77
Figure 37	Loss modulus (G") as a function of temperature over the temperature range of interest to the thermal model.	79
Figure 38	Variation of heat generation rate with temperature used in the thermal model. The loss modulus curve is from Figure 37.	80
Figure 39	Boundary conditions used in the FY 80 thermal model.	81
Figure 40	Temperature-time response for a point 16 mm (0.625 in.) below the surface of the pad as predicted by the thermal model using the heat generation rate from Figure 38. The temperature-time response measured during field testing is shown as a solid line. The predicted results show a maximum deviation of 60°C with the measured results. Also shown in the figure is the temperature-time response assuming a constant heat generation rate.	83
Figure 41	Contours of constant temperature after 2,000 s (0.56 hr) at 32 km/hr (20 MPH).	85
Figure 42	Contours of constant temperature at 4,000 s (1.11 hr) at 32 km/hr (20 MPH).	86
Figure 43	Contours of constant temperature after 6,000 s (1.67 hr) at 32 km/hr (20 MPH).	87
Figure 44	Temperature profile across the pad from the bottom of the pad to the steel backing plate. Profile is for pad after 2,000 s (0.56 hr) at 32 km/hr (20 MPH).	89
Figure 45	Temperature profile across the pad after 4,000 s (1.11 hr).	90
Figure 46	Temperature profile across the pad after 6,000 s (1.67 hr).	91

Figure 47	Temperature-time response for nodes 10, 97, and 202.	92
	Nodes are identified in Figure 49.	
Figure 48	Temperature-time response for nodes 37, 406, and 503.	93
	Nodes are identified in Figure 49.	
Figure 49	Location of nodes whose temperature-time response is	94
	shown in Figures 47 and 48.	
Figure 50	Temperature-time response for the surface of the pad	95
	assuming constant and variable heat transfer coefficients (h). Results are compared with actual field data.	
Figure 51	Finite element mesh used in the FY 80 mechanical	97
	model. The influence of the roadwheel has been incorporated into the analysis. Loading conditions are shown in the figure.	
Figure 52	Outline of the finite element mesh shown in Figure 43	98
	showing the materials used in the analysis.	
Figure 53	Typical stress-strain loop for a viscoelastic material	99
	showing the short-time and long-time shear relaxation moduli.	
Figure 54	Schematic diagram of the track on the M60 tank showing	101
	variation in tension along the track.	
Figure 55	Interfacial pressure between the roadwheel and the	103
	roadwheel path generated as the roadwheel is displaced downward.	
Figure 56	Deformation produced in the tank track shoe and related	104
	track components due to the full applied load of the roadwheel.	
Figure 57	Contours of constant normal stress σ_{zz} produced in	105
	the tank track shoe and roadwheel path due to the full applied load of the roadwheel.	
Figure 58	Contours of constant effective stress produced in the	106
	tank track shoe and roadwheel path due to the full applied load of the roadwheel.	
Figure 59	Infrared spectra of the pyrolyzates from new from	113
	Vender B tread.	
Figure 60	Infrared spectra of the pyrolyzates from new from	114
	Vender A tread.	
Figure 61	Infrared spectra of the pyrolyzates from new from	115
	Vender D tread.	
Figure 62	Infrared spectra of the pyrolyzates from new from	116
	Vender C tread.	

Summary

This report describes a two-year study into the failure of tank track pads. These pads are made of styrene butadiene rubber (SBR) which is bonded to a steel backing plate. This assembly is bolted to the bottom of the T-142 track and supports the weight of the tank. This pad shows a rather limited and highly varying service life depending largely upon the type of terrain over which the tank is run. In addition, the mechanism of failure is dependent upon the type of terrain. This project is primarily concerned with failure mechanisms that most severely limit service life.

The objective of this study is to obtain information which can be used to extend the in-service life of tank track shoes. Several parallel and complementary paths are being taken. One is through finite element computer analysis of the pads structural and thermal response to tank operation. Such an analysis provides valuable insight into the problem. In addition, we are developing a failure model for the T-142 shoe which, when interfaced with the structural and thermal computer models, will help identify operating situations and conditions that produce failure. Secondly, the information gained in this program will help identify relevant properties and parameters to be included in production or product specifications to help insure product quality. Extending pad service life by the use of improved rubber blends or possible changes in processing procedures is also under investigation. This effort involves studying the mechanical and chemical degradation that the rubber experiences under field conditions.

The emphasis in FY 79 was primarily analytical and centered upon developing better insight into the problem. The temperature buildup in pads for the T-142 track was studied using a simple computer model and TACO, a finite element heat transfer code. The model represented a cross section of the T-142 track including the tank track pad. Boundary conditions were taken as constant temperatures at the boundaries. A preliminary assessment of failure was also made. In addition, experiments were performed in which crack growth, fatigue strength, and residual tear strength after fatigue were studied.

In FY 80, a more advanced thermal computer model was used. This model included the influence of convective boundary conditions on the temperature buildup in pads. The model incorporates the variation in heat capacity and heat generation rate that occurs with temperature. The temperature predictions of the model agree well with field data taken on the T-142 tank track pad. The model predicts a temperature-time response at an interior point of the pad that deviates from field data by no more than 6°C (11°F). The model shows that after 6,000 s (1.67 hr) of running time the maximum pad temperature of 132°C (270°F) occurs near the center of the pad. The results of the model have been plotted as constant temperature contours, temperature-location profiles across the pad, and temperature-time histories for points within the pad. The structural response of the pad to the loading provided by the tank was analyzed using a mechanical model and NIKE2D, a finite element computer code for analyzing the static and dynamic behavior of two-dimensional solids. The model uses a section of track and roadwheel, and simulates the movement of the roadwheel onto and over the roadwheel path. Calculations were done for the pad traversing a flat surface. Contour plots showing the normal stress and effective stress generated in the pad were obtained. The largest compressive normal stress over a significant volume of material was found to be 2.5 MPa (360 psi). The equivalent stress, which is a measure of the stress producing distortion in the pad, was found to be 2 MPa (290 psi). These stresses are quite low, relative to stresses that one might expect for fracture. This result is consistent with the observation that rubber fractures are not produced on paved surfaces.

Field data relevant to the problem were also collected in FY 80. Tests were conducted on an M-103 tank at the Yuma Proving Grounds. The tank was run over a paved surface, and the surface and internal pad temperatures were measured as a function of running time and pad manufacturer.

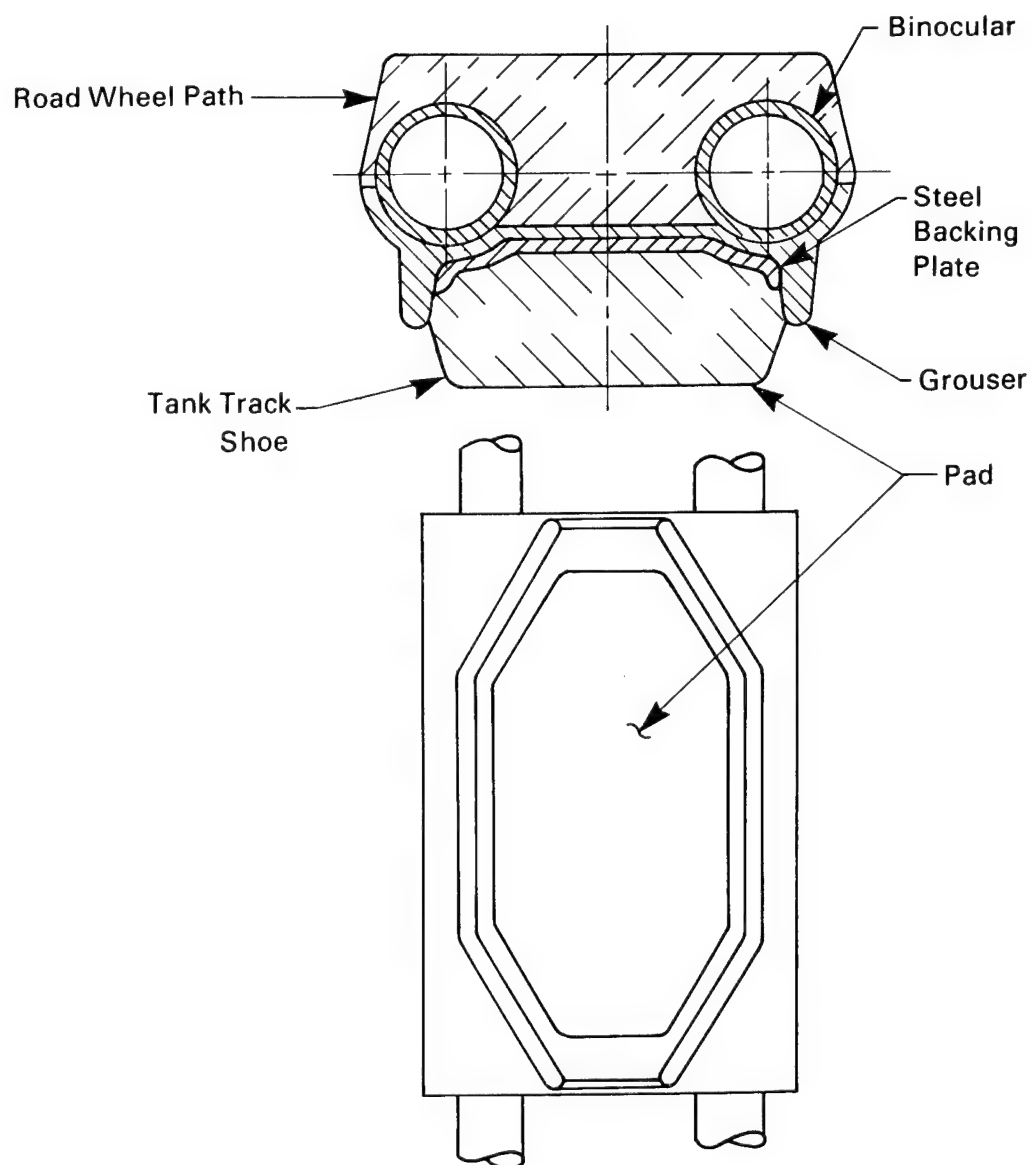
Physical and chemical characterization of the as-manufactured SBR was also performed. Some of this information was needed for the computer analyses. We also examined the changes in physical properties and chemical characteristics brought about by running pads on a tank at the Yuma Proving Grounds. The thermal diffusivity was observed to decrease by about 20% due to field testing, while the tear strength decreased between 20% and 30% depending on the terrain. These changes occur due to damage accumulation introduced during field testing.

Our studies in the next year will work from the computer models developed in FY 80. The structural model will study the response of the pad to the sharp projections and non-smooth contours encountered in cross-country operations. Field testing with the T-142 track will be done to assess the validity of the model predictions. In addition, we plan to develop a failure criterion for the model. Our studies into damage accumulation in SBR will continue.

1. INTRODUCTION

1-1. Scope of the Problem: The M60 Series Tank uses the T-142 tank track shoe. The shoe is made of Styrene Butadiene Rubber (SBR) which is bonded to a steel backing plate. These shoes are bolted to the bottom of the T-142 tank track and support the weight of the tank. The shoe and relevant section of track are shown in cross-section in Figure 1. This shoe shows a rather limited and highly varying service life depending largely upon the type of terrain over which the tank is run. On paved roads, the service life of the pad is limited by abrasion and up to about 3,400 km (2,000 miles) of service can be obtained. On gravel or cross country terrain, service life of the pad is limited to about 1,500 km (900 miles) and 420 km (250 miles), respectively. In addition, the mode of failure has changed from abrasion to modes that are identified in the field as cutting and chunking. Cutting is believed to result from "road hazards" and is probably associated with materials tear resistance. Chunking, on the other hand, is believed to be related to a fatigue crack initiation and propagation mechanism. A fourth type of failure, called a blowout, can also occur in tank track shoes. A high internal pad temperature is believed to be a significant factor in this failure. This program is primarily concerned with the failure processes that most severely limit service life -- chunking, cutting, and blowout.

The objective is to obtain information which can be used to extend the in-service life of tank track shoes. Several parallel and complementary paths are being taken. One is through finite element computer analysis of the pads' structural and thermal response to tank operation. Such an analysis provides valuable insight into the problem. In addition, we are developing a failure model for the T-142 shoe, which, when interfaced with the structural and thermal computer models, will help identify operating situations and conditions that produce failure. Secondly, the information gained in this program will help identify relevant properties and parameters to be included in production or product specifications to help insure product quality.



Tank Track Pad and Related Track Parts

Figure 1 The T-142 tank track shoe and relevant sections of track.

Extending pad service life by the use of improved rubber blends or possible changes in processing procedures is also under investigation. This effort involves studying the mechanical and chemical degradation that rubber experiences under field conditions.

This report describes work completed during FY 79 and FY 80 at the Lawrence Livermore National Laboratory (LLNL). It is divided into work completed during these years.

1-2. FY 79 Work: The emphasis in FY 79 was primarily analytical. Work completed in this first year centered upon developing a better insight into the problem. The temperature of the pads was recognized as an important parameter. The properties of SBR can be strongly influenced by temperature; indeed excessive temperatures can promote failure. The need for quantitatively understanding this aspect of the problem is enhanced by the facts that an energy dissipative material such as SBR can generate significant amounts of heat during loading and unloading of the pads and the ability of the material to dissipate heat (as measured through its thermal diffusivity) is quite low. Thus, the temperature build-up in pads for the T-142 track was studied using a simple computer model and TACO, a finite element heat transfer code.

The structural response of the pad to the loading provided by the tank was analyzed using a mechanical model and NIKE2D, a finite element code for analyzing the static and dynamic behavior of two-dimensional solids. Such an analysis provides the opportunity for studying the stresses and strains developed within the pad. All codes utilized in this study had been previously developed by the LLNL Mechanical Engineering Department staff.

Material properties required for these analytical studies were determined. Efforts in FY 79 also involved characterizing the SBR used in tank track pads for some of its relevant chemical, physical, and mechanical properties.

A preliminary assessment of failure was also made. Experiments were performed in which crack growth, fatigue strength, and residual tear strength after fatigue were studied.

1-3. FY 80 Work: In FY 80 the program became broader based and combined field testing, computer analysis, and laboratory testing to study failure in SBR with application to the T-142 shoe. The activities this year have centered on the following:

1-3a. Field Analysis: Field data relevant to the problem has been collected and analyzed. This data is essential to understanding the relevant parameters and characteristics of the different failure modes. It also provides valuable feedback on the predictions generated by the computer analyses.

1-3b. Analytical Work: The work done in FY 80 involved an important expansion and refinement of the models used in FY 79. The thermal computer model included the influence of convective boundary conditions on the temperature buildup in pads.

The structural response of the pad was also studied in a much more realistic way, in that the mechanical model represents a section of track and roadwheel and simulates the movement of the roadwheel onto and over the roadwheel path.

1-3c. Experimental Work

1-3c(1). Physical and Chemical Characterization: The as-manufactured SBR pads have undergone both physical and chemical characterization. Some of the physical properties measured are used in the computer codes while other physical properties measured provide a baseline characterization of the material. Likewise, the chemical characterization was done on SBR at the molecular, macromolecular, and composite level. The properties evaluated are examined in a later section of this report.

1-3c(2). Effect of Mileage and Terrain: The effect of mileage and terrain on the chemical degradation and physical properties of tank track pads tested at the Yuma Proving Grounds has been evaluated. Some of those physical properties, when interfaced with the computer analyses, can help to delineate the relevant parameters in the failure process. The chemical characterization provides insight into the changes in structure that produce undesirable changes in properties. Highlights from this study will be presented later in the report.

2. FY 79 REPORT

2-1. Temperature Analysis

2-1a. Material Properties: Material properties required as input for the TACO code include the hysteretic heat generation rate, density, specific heat, and thermal conductivity. A published report provided the heat generation rate.¹ In that study, the heat generation rate of the T-142 tank track pad was obtained by loading the entire pad in a cyclic mode. Data to frequencies of 100 Hz and a maximum force of 44,500 N (10,000 lbs.) were obtained. The hysteretic heat generated in the pad could then be determined as a function of tank weight and speed. We then calculated the heat generation rate and it is presented in Table 1 as a function of vehicle speed.

Density, specific heat, and thermal conductivity were all determined at LLNL on a sample of T-142 tank track pad provided by TARADCOM. The sample was manufactured by Vender A.* Details of all testing procedures used are

*SBR pads from four vendors were examined in this study. The vendors will be referred to as Venders A, B, C, and D.

TABLE 1

HYSTERETIC HEAT GENERATION RATE
FOR T-142 SHOE AS A FUNCTION OF TANK SPEED

<u>Velocity</u> <u>m/s</u>	<u>Heat Generation Rate</u> <u>kW/m³</u>
2.23	27
4.47	53
8.94	107
13.41	160
17.88	213

provided in Appendix A. An immersion density technique was used to determine the density to be 1.191 Mg/m³ (74.4 lb./ft.³).. Thermal conductivity was evaluated from the thermal diffusivity of the material using a flash laser method. The measurement was made at temperatures between 20°C (68°F) and 200°C (392°F). The thermal conductivity is related to the thermal diffusivity by the expression:

$$\alpha = K / \rho c \quad (1)$$

where

α = thermal diffusivity

K = thermal conductivity

ρ = density

c = specific heat

Results are given in Table 2.

The specific heat was evaluated using differential scanning calorimetry at temperatures between -20°C (-4°F) and 200°C (392°F). Results are given in Table 3.

2-1b. Analysis: The computer codes utilized in these studies are shown in a flow diagram in Figure 2. The figure is broken down into the codes and post processors used and the outputs generated. The post processors further analyze the information generated by the codes and manipulate it into desired plots and contours. The finite element mesh is generated by a code called ZONE. This mesh can be used in both TACO, the thermal analysis code, and NIKE2D, the structural response code. The post processor PLOT can operate on the output from ZONE to produce a printout of the geometry or mesh plot being

TABLE 2

THERMAL CONDUCTIVITY FOR SBR FROM VENDER A

Temperature (°C)	Thermal Conductivity $\text{W/m}^{\circ}\text{C} \times 10^{-1}$
20	3.54
40	3.67
80	3.54
120	3.39
160	3.41
200	3.35

TABLE 3
SPECIFIC HEAT FOR SBR FROM VENDER A

Temperature (°C)	Specific Heat (J/kg °C) x 10 ³
20	1.42
40	1.51
80	1.61
120	1.68
160	1.79
200	1.89

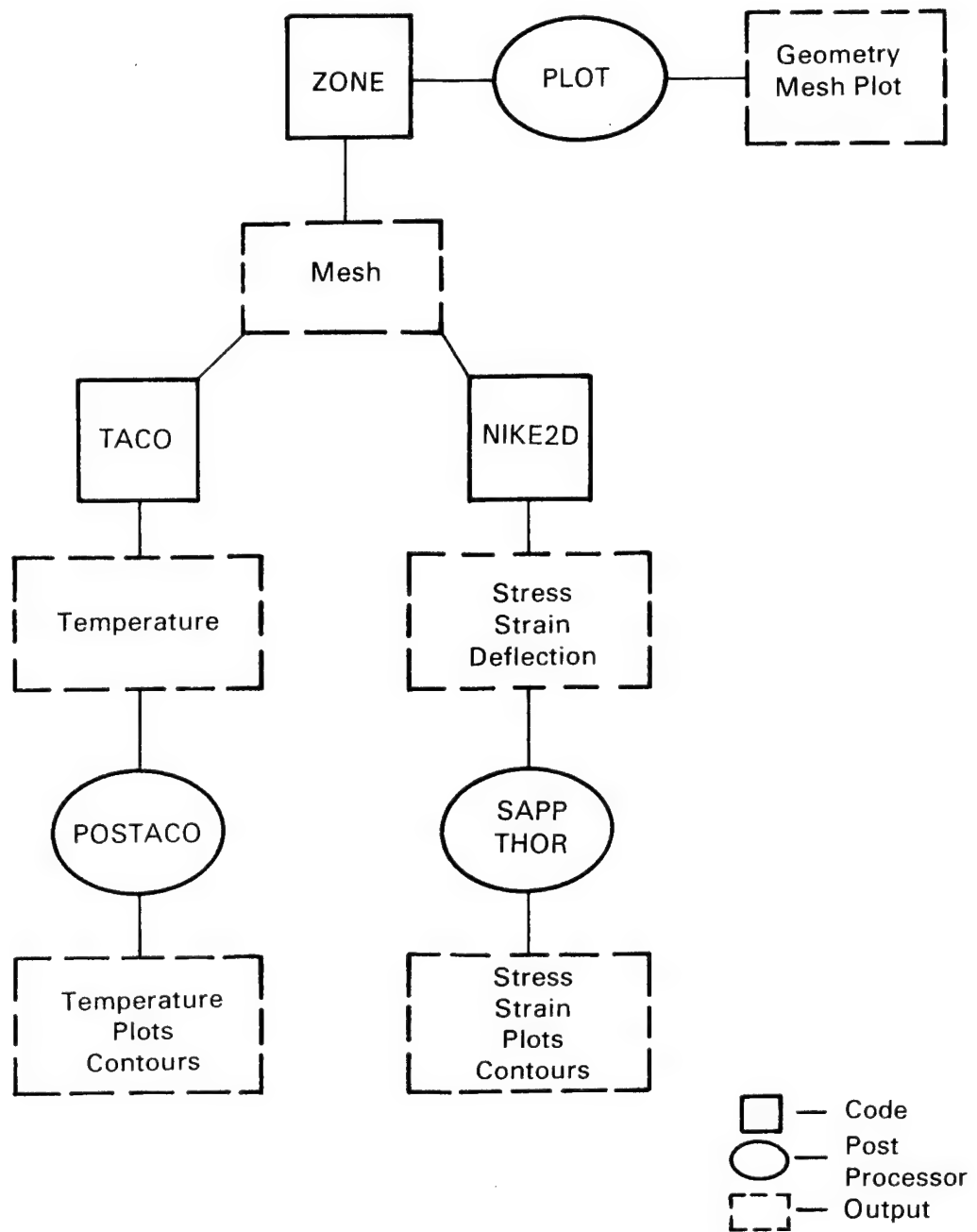


Figure 2 Flow diagram showing codes and post processors used in this study. The outputs generated are indicated in the diagram.

used in the codes. The finite element computer model used in the FY 79 study is shown in Figure 3. The model consists of a plane section of T-142 track including the pad and supporting terrain.

For the thermal model, such a plane section assumes that heat losses at the end of the pad have relatively little influence on the temperatures developed at interior sections. Thus, for interior sections, heat flow occurs only in the plane section being studied. This is a valid assumption due to the high length-to-width ratio of the pad.

The procedures and codes could also be used to analyze different sections of track and different track designs. Notice that the different materials relevant to the problem are represented in the mesh. The delineation of materials is shown in Figure 4. Each of these materials is represented by its own material properties. The properties of a given material can also be varied throughout the mesh. In the present analyses, the properties of a given material were assumed to be uniform throughout the mesh.

The heat transfer calculations performed in this investigation consisted of both transient and steady-state calculations. In this model, the boundary conditions were taken as constant temperatures at the boundaries. This was accomplished by holding the temperature of selected nodes along the boundary to temperatures representative of steady-state conditions. The temperature of the ground was selected as 50°C (122°F) and the temperature of the binocular as 119°C (245°F). The temperature of exterior track surfaces was assumed to be 85°C (185°F). The nodes held to constant temperature are illustrated in Figure 5. The initial temperature of the track was assumed to be 30°C (86°F). The calculated temperatures in pads are very sensitive to the boundary conditions assumed. For the preliminary calculations done here, these values represent reasonable choices. The tank is assumed to operate at 8.94 m/s (20 MPH), and the heat generation rate is 107 kW/m^3 ($10.4 \times 10^3\text{ Btu/hr ft}^3$). The specific heat and thermal conductivity were both taken to be functions of temperature from Tables 2 and 3.

2-1c. Temperature Analysis Results: The temperature response of the T-142 tank track shoe was analyzed for both transient and steady-state solutions. Transient results approach the steady-state results. The rubber in the road wheel path was assumed to have the same properties as the tank track shoe rubber. With time, the temperature at the interior of the shoe exceeds the surface temperature because of heat generation.

The temperature-time response for two locations within the pad (locations A and B in Figure 4) are shown in Figures 6 and 7. The temperature-time response for the surface of the pad (identified as point C in Figure 4) is shown in Figure 8. Transient calculations were performed for times up to 6,000 s (1.67 hr). The steady-state temperatures for all three points are indicated in the figures. At 6,000 s (1.67 hr), the temperatures of all three locations within the pad are still rising. However, the temperatures at 6,000 s have come very close to their steady-state values -- exhibiting a maximum deviation of about 16°C (approx. 61°F) for point A.

The results of thermal model calculations can be plotted as contours of constant temperature. Such plots for transient results after 2,000 s (0.56 hr), 4,000 s (1.11 hr), and 6,000 s (1.67 hr) are shown in Figures 9, 10, and 11. One important observation here is that the rubber of the roadwheel path achieves temperatures comparable to those achieved in the pad. The location of maximum temperature is shown in Figures 9, 10, and 11. Notice that after 4,000 s (1.11 hr) and 6,000 s (1.67 hr) the maximum temperature at the center of the pad is 199°C (390°F) and 222°C (432°F), respectively.

The results of the thermal model can also be presented as profile plots in which the temperature along an arbitrary straight line is plotted. Figures 12, 13, and 14 show such profile plots in which the temperature along the centerline of the pad is plotted from the ground to the steel backing plate for times of 2,000 s (0.57 hr), 4,000 s (1.11 hr), and 6,000 s (1.67 hr). The plots show that a very steep thermal gradient is developed within the pad.

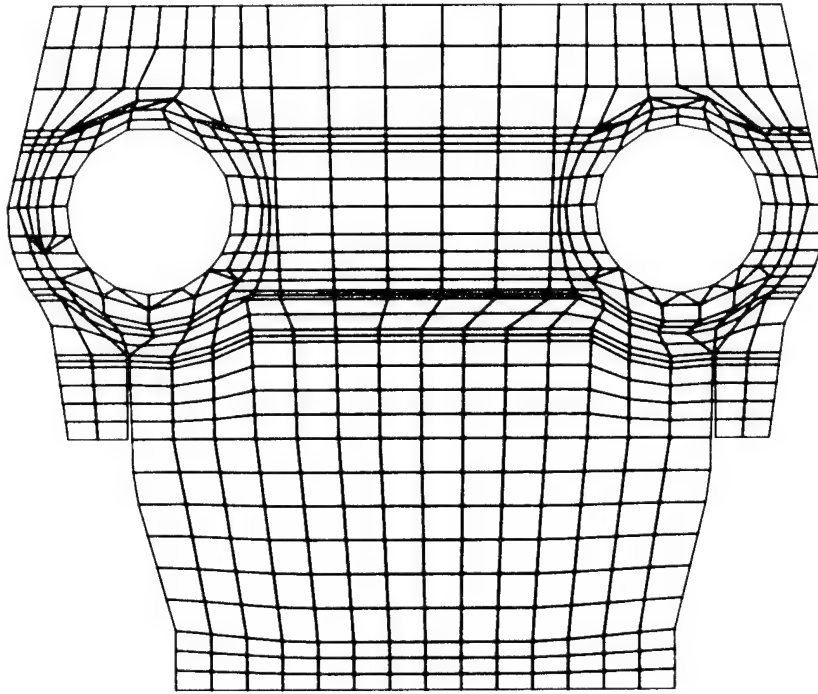


Figure 3 Finite element mesh used in the FY 79 TACO and NIKE2D analyses. Mesh represents a plane section of T-142 track including the pad and supporting terrain.

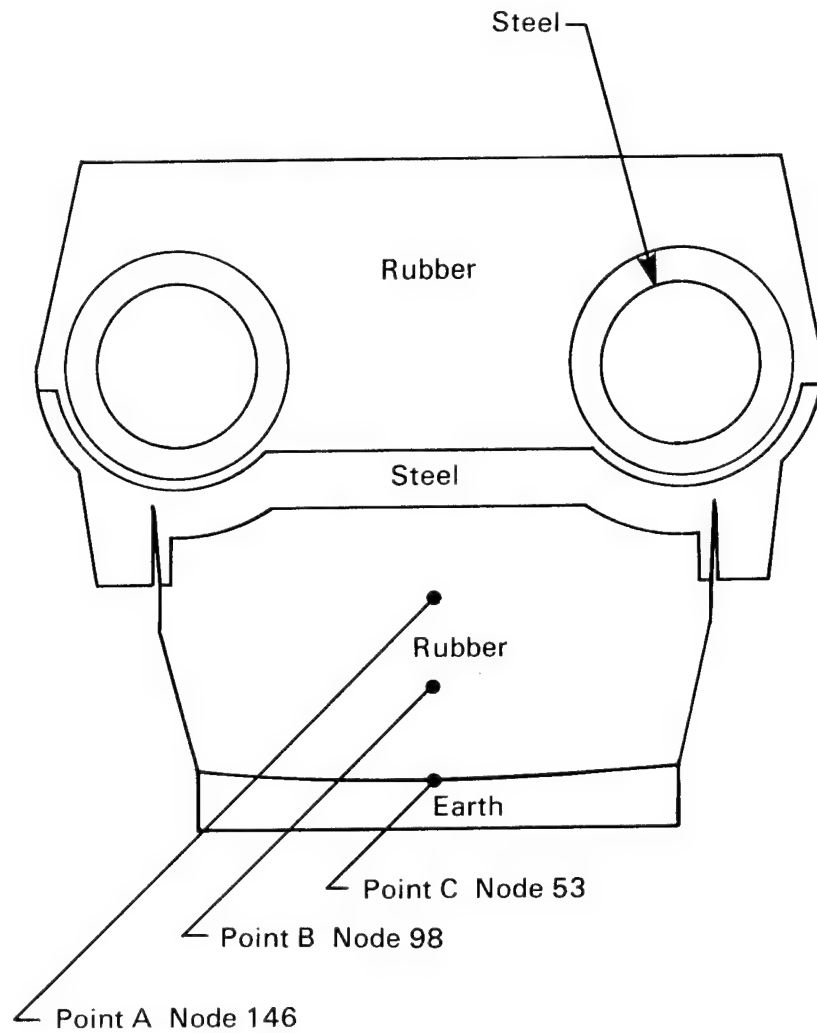


Figure 4 Outline of finite element mesh showing different materials used in the analysis.

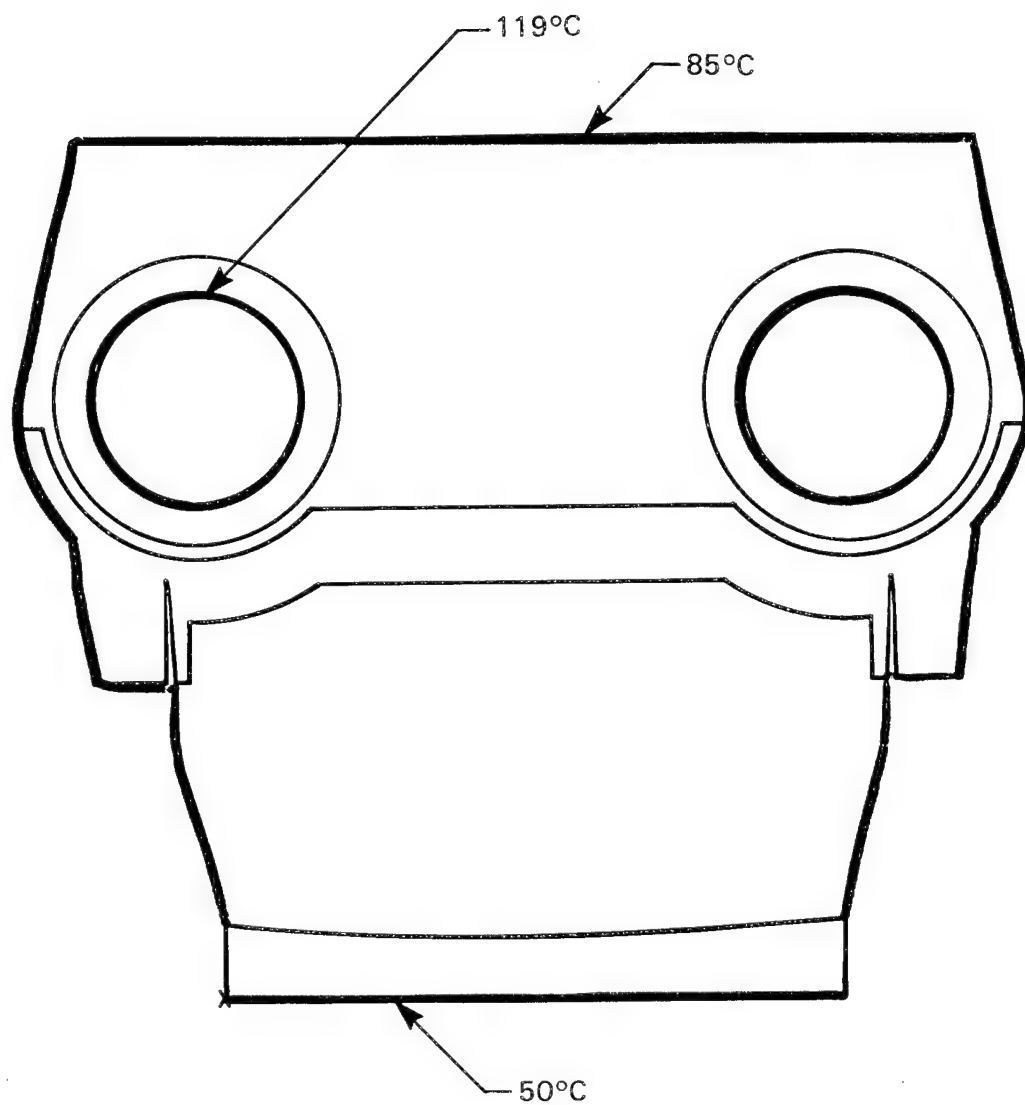
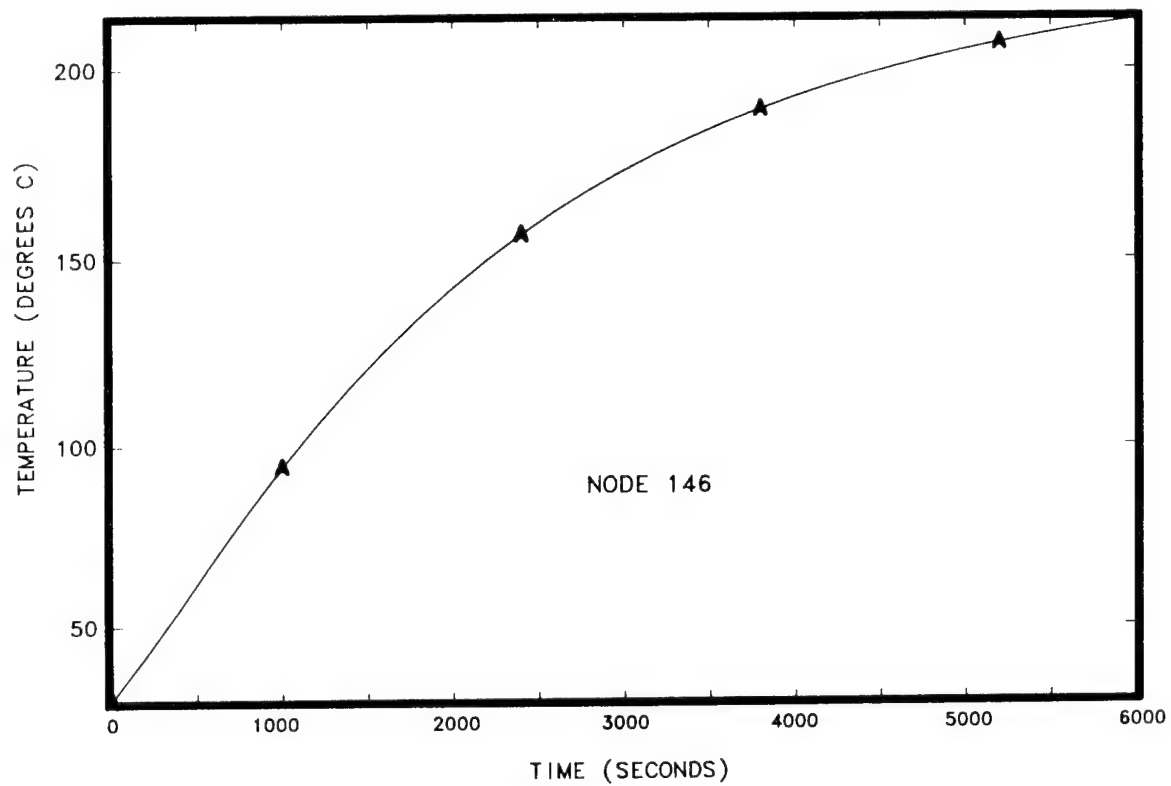


Figure 5 Surfaces held to constant temperature in the FY 79 thermal model.



STEADY STATE TEMPERATURE = 228 DEGREES C

Figure 6 Temperature-time response for point 1 within the tank track pad. Boundary conditions are shown in Figure 5.

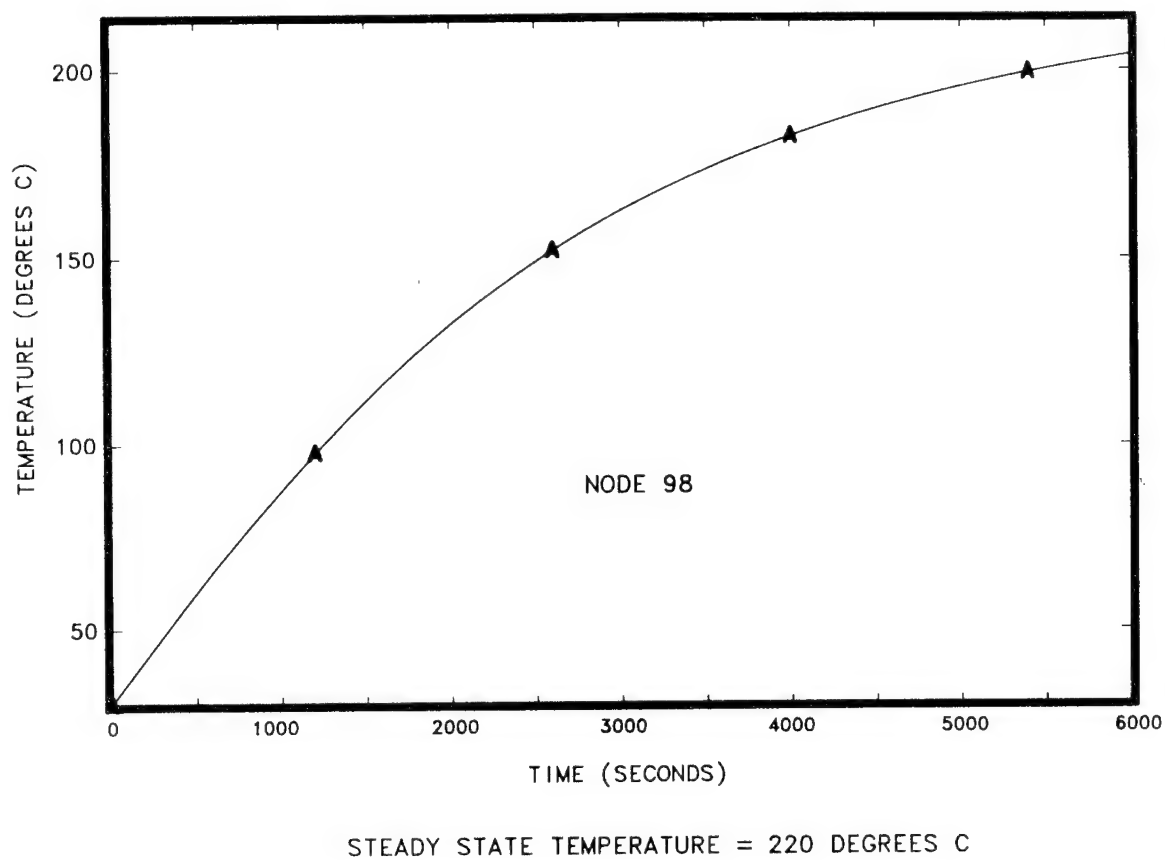


Figure 7 Temperature-time response for point 2 within the tank track pad. Boundary conditions are shown in Figure 5.

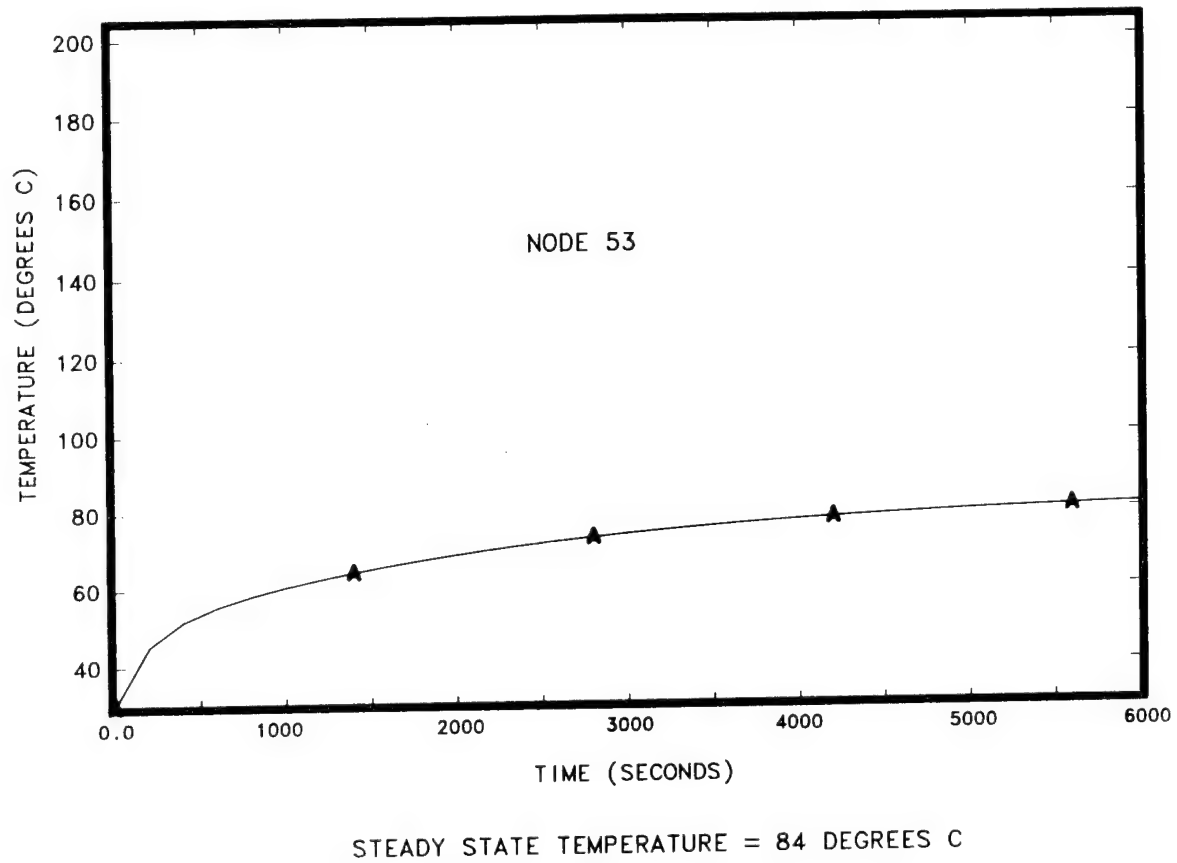
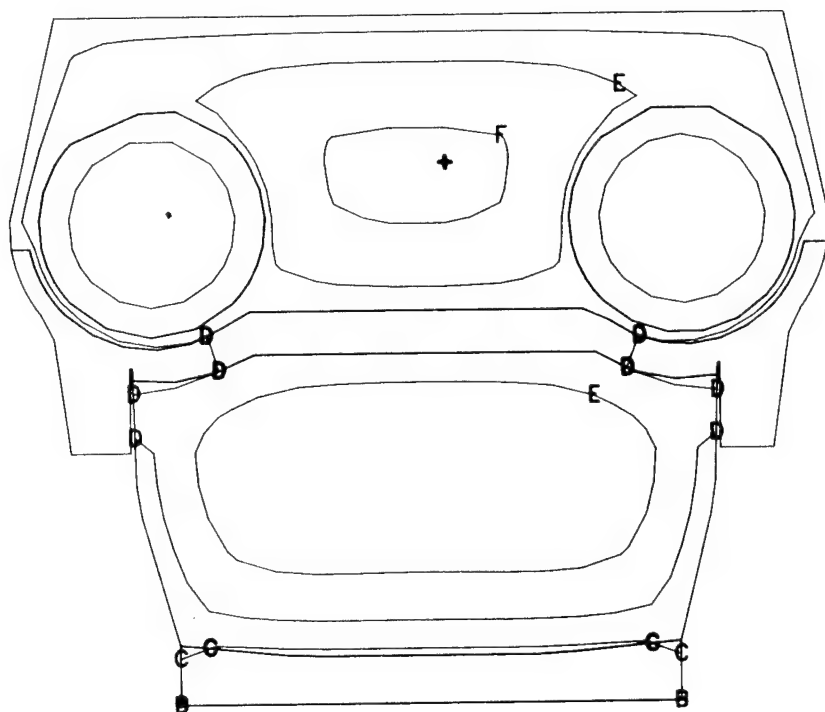


Figure 8 Temperature-time response for central point at the surface of the tank track pad. Boundary conditions are shown in Figure 5.



TEMPERATURE IN
DEGREES C

MAXIMUM AT + =
154.6

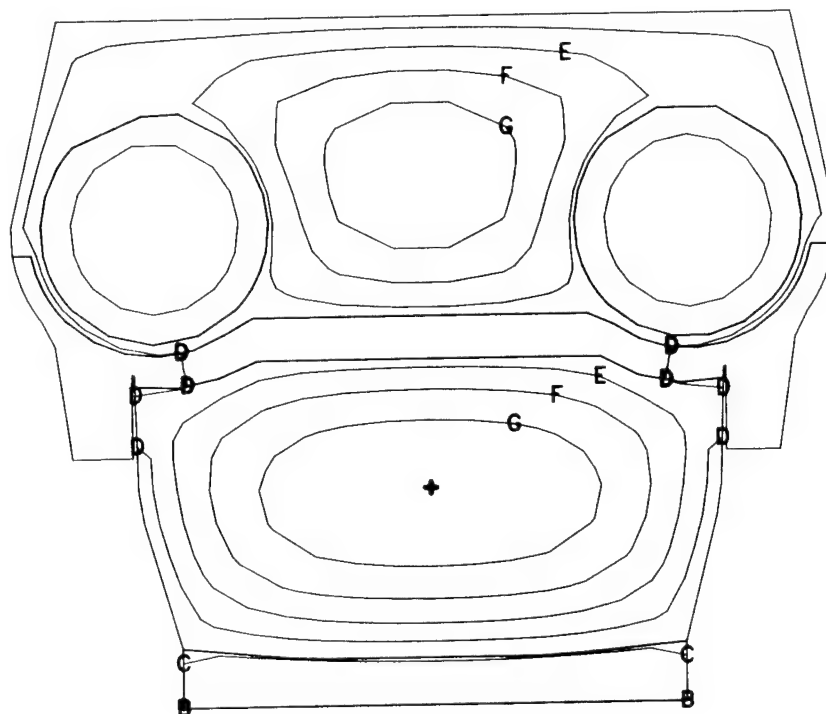
AVERAGE = 111.0

CONTOUR LEVELS

B = 50.0
C = 75.0
D = 100.0
E = 125.0
F = 150.0

TIME = 2000 SECONDS

Figure 9 Contours of constant temperature after 2,000 s (0.56 hr.) at 32 km/hr (20 MPH) as predicted using the boundary conditions shown in Figure 5



TEMPERATURES IN
DEGREES C

MAXIMUM AT + =
198.6

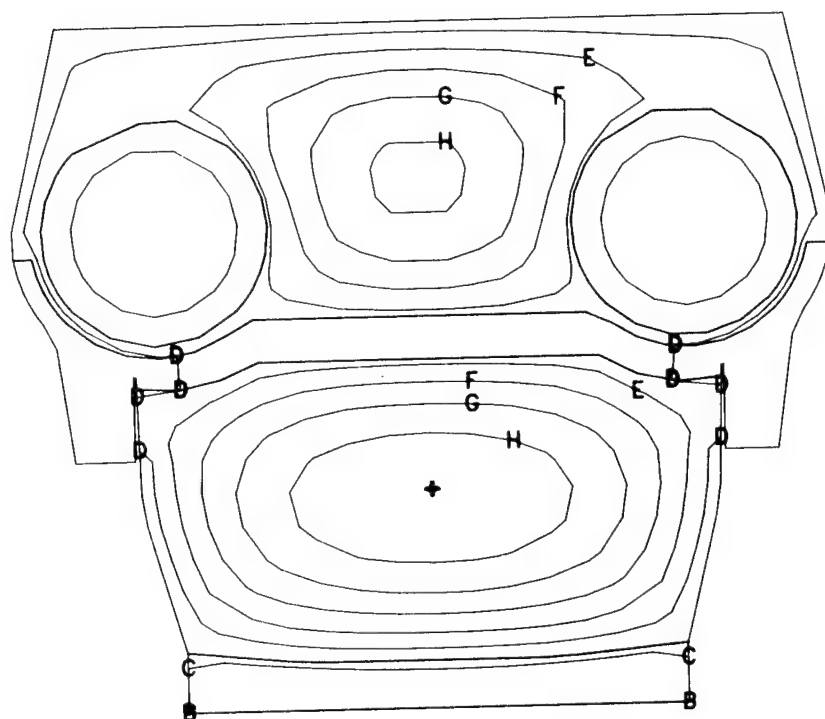
AVERAGE = 119.9

CONTOUR LEVELS

B = 50.0
C = 75.0
D = 100.0
E = 125.0
F = 150.0
G = 175.0

TIME = 4000 SECONDS

Figure 10 Contours of constant temperature after 4,000 s (1.11 hr.) at 32 km/hr (20 MPH) as predicted using the boundary conditions shown in Figure 5



TEMPERATURE IN
DEGREES C

MAXIMUM AT + =
222.2

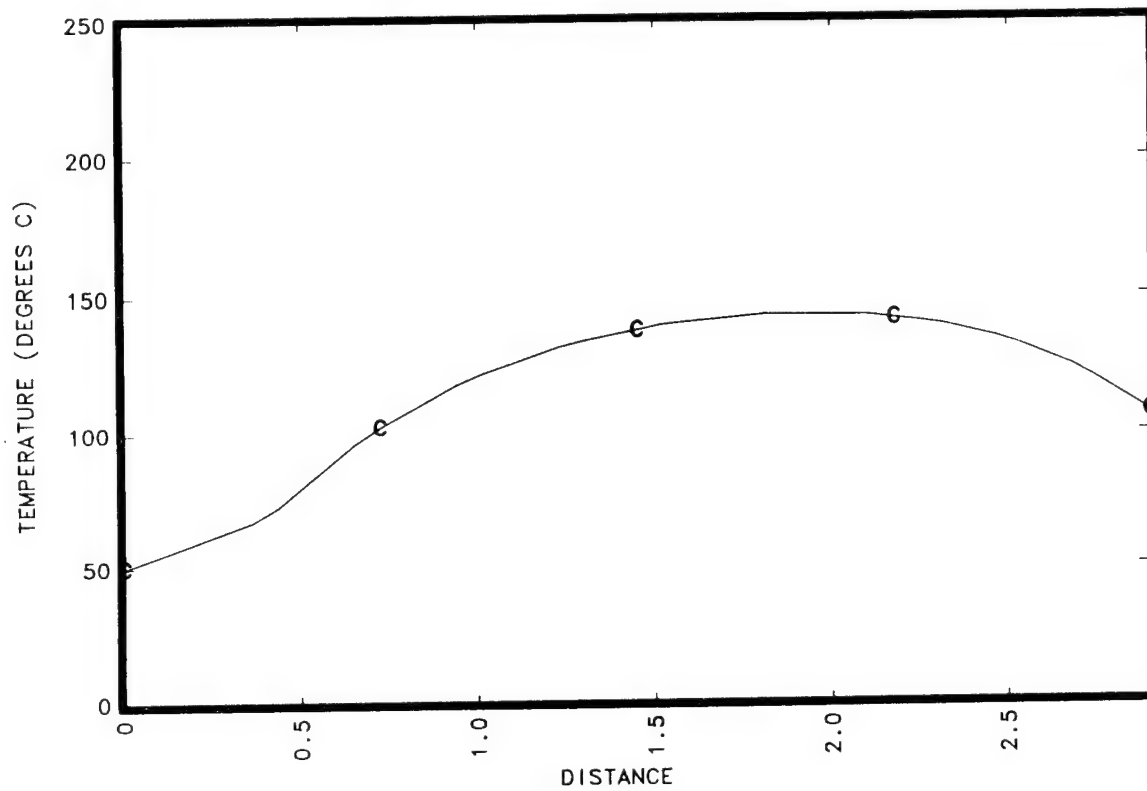
AVERAGE = 123.1

CONTOUR LEVELS

B = 50.0
C = 75.0
D = 100.0
E = 125.0
F = 150.0
G = 175.0
H = 200.0

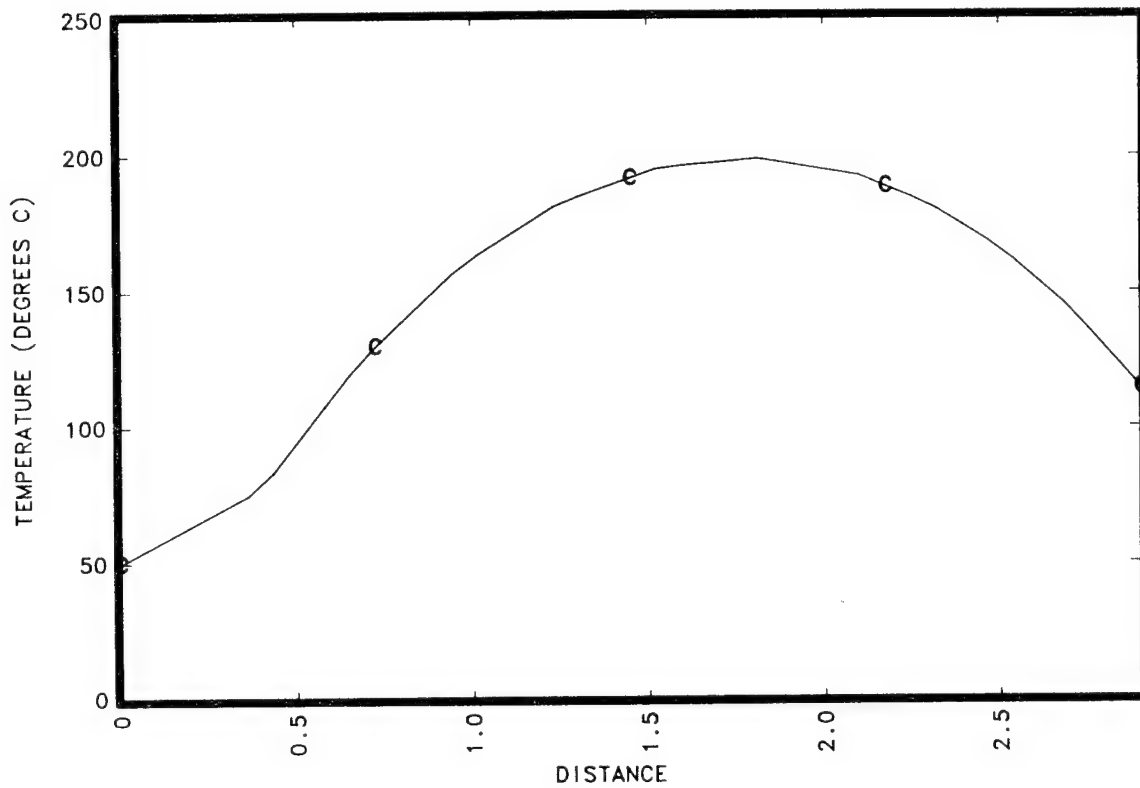
TIME = 6000 SECONDS

Figure 11 Contours of constant temperature after 6,000 s (1.67 hr.) at 32 km/hr (20 MPH) as predicted using the boundary conditions shown in Figure 5



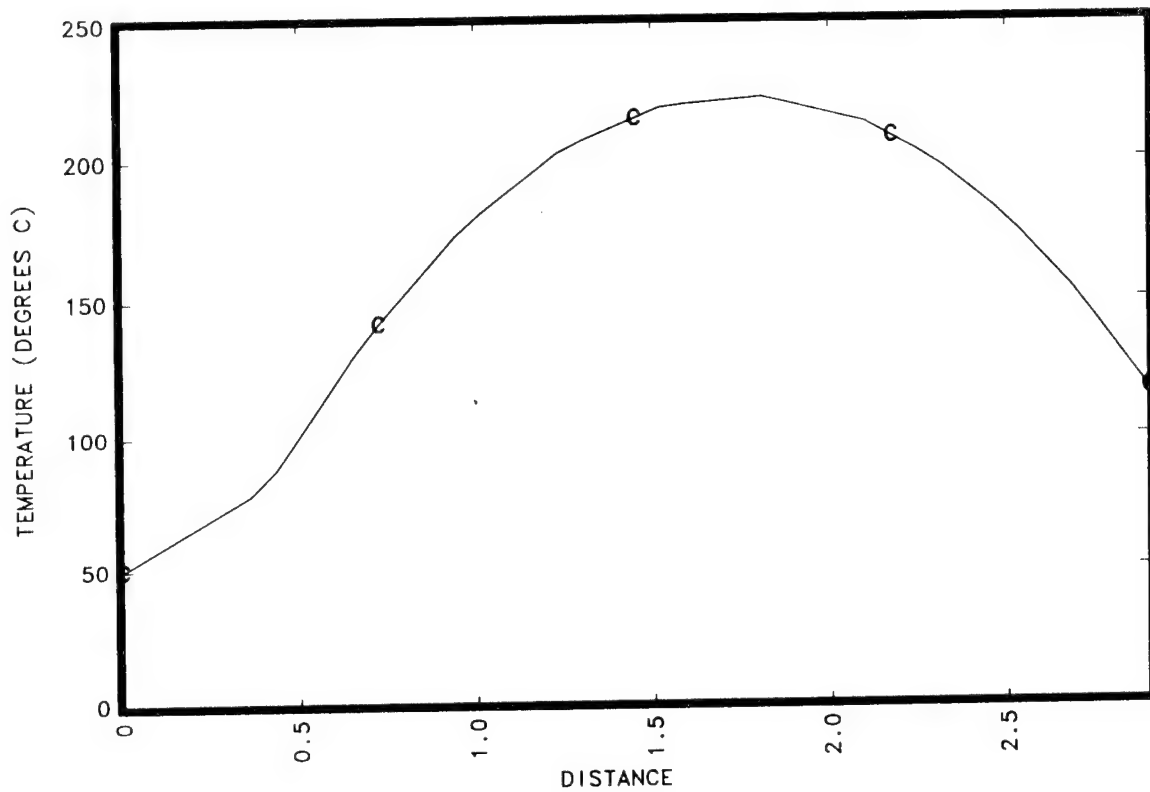
TIME = 2000 SECONDS

Figure 12 Temperature profile across the pad from the supporting terrain to the steel backin gplate. Profile is for pad after 2,000 s (0.56 hr.) at 32 km/hr (20 MPH)



TIME = 4000 SECONDS

Figure 13 Temperature profile across pad after 4000 s (1.11 hr).



TIME = 6000 SECONDS

Figure 14 Temperature profile across pad after 6000 s (1.67 hr).

The results presented above show substantial increases in the temperature of the pad. The FY 80 report presents pad temperature measurements taken in the field on an operating tank. These temperatures are significantly lower than the temperatures predicted by this model. The primary difficulty is that the change in hysteretic heat generation rate with temperature is not incorporated into the model. The thermal model work done in FY 80 incorporates this effect. Further discussion will be presented at that time. The results are also strongly dependent on assumed boundary conditions. The FY 80 report addresses to a limited degree the strength of that influence.

2-2. Structural Analysis: The structural analysis of the track pad completed in FY 79 represented a first approach solution to the problem. These results were largely superseded by analysis work done in FY 80, which will be presented later. Material properties required for this analysis were determined and will be presented here. The NIKE2D code uses a linear viscoelastic material model based upon a three element linear solid. This solid can be represented as two linear springs and a linear dashpot connected as shown in Figure 15-1. The shear relaxation behavior of this solid can be represented as shown in Figure 15-2 by the equation:

$$G(t) = G_{\infty} + (G_0 - G_{\infty}) e^{-B't} \quad (2)$$

where

G_0 = short time shear modulus

G_{∞} = long time shear modulus

B' = decay constant

These quantities can be obtained from the storage modulus and loss modulus in shear and $\tan \delta$ (where δ is the phase lag between stress and strain.) The later quantities were obtained in torsion at very small strains as a function of temperature. Results are presented in Figures 16 and 17 for a frequency of 0.1 Hz and the temperature range of -150°C (-238°F) to 210°C (410°F). The NIKE2D code calculations also require the density and bulk modulus. The bulk modulus of SBR from Vender A was determined at temperatures between -50°C (-58°F) and 400°C (752°F). This information is presented in Figure 18.

2-3. Materials Characterization

2-3a. Chemical

2-3a(1). Carbon Black: Tests were performed to determine the percent carbon black in four samples of tank track shoe from Vender A. These tests were done in part to assess the variation of carbon black in a typical pad. Material properties can be strongly affected by the amount of carbon black, its type, and micron size. Thus, results here on composition variations will provide insight into the origin of observed property variations. Each sample was tested in duplicate, using contiguous pieces. Procedural details for this test and all tests used in this report are given in Appendix A. The results are given in Table 4. The average value of carbon black is 35.1% with a high value of 36.5% and a low value of 34.8%. The variation is insufficient to cause variations observed in material properties for virgin specimens.

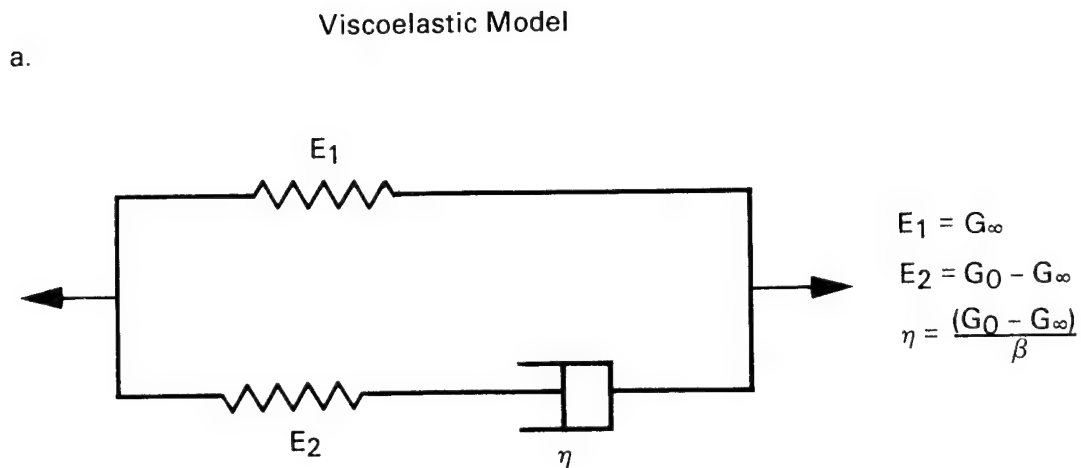


Figure 15-1 Three element standard linear solid used in the viscoelastic material model contained in NIKE2D

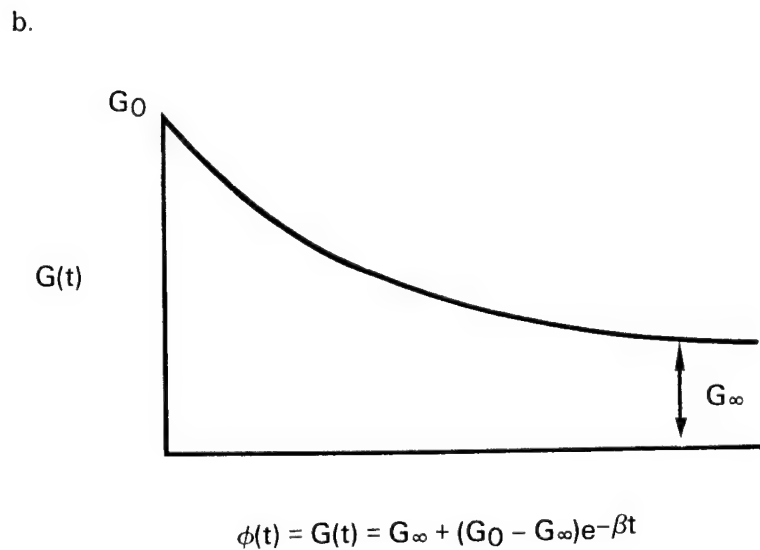


Figure 15-2 Relaxation behavior of the shear modulus as predicted by the model in 15-1. The curve can be described by the equation shown.

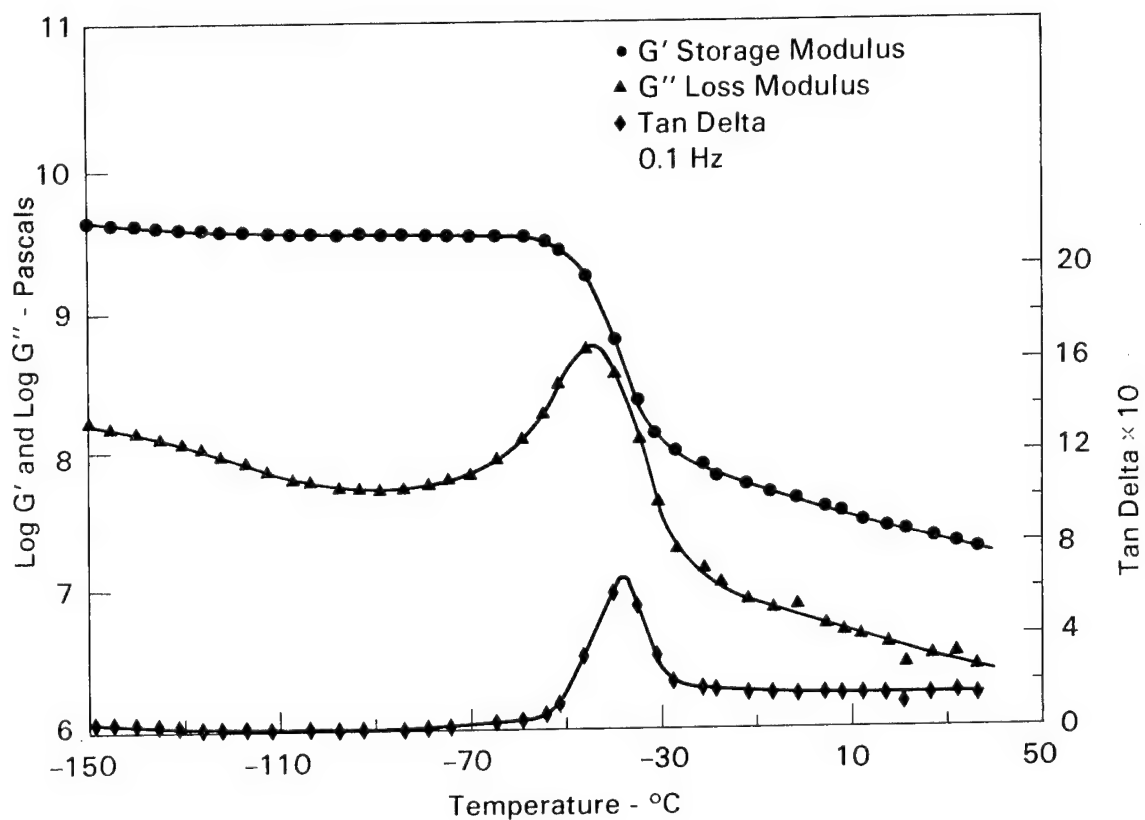


Figure 16 Storage modulus (G'), loss modulus (G''), and tan delta (δ) plotted versus temperature (-150°C to 50°C). Data determined in low strain torsion experiments.

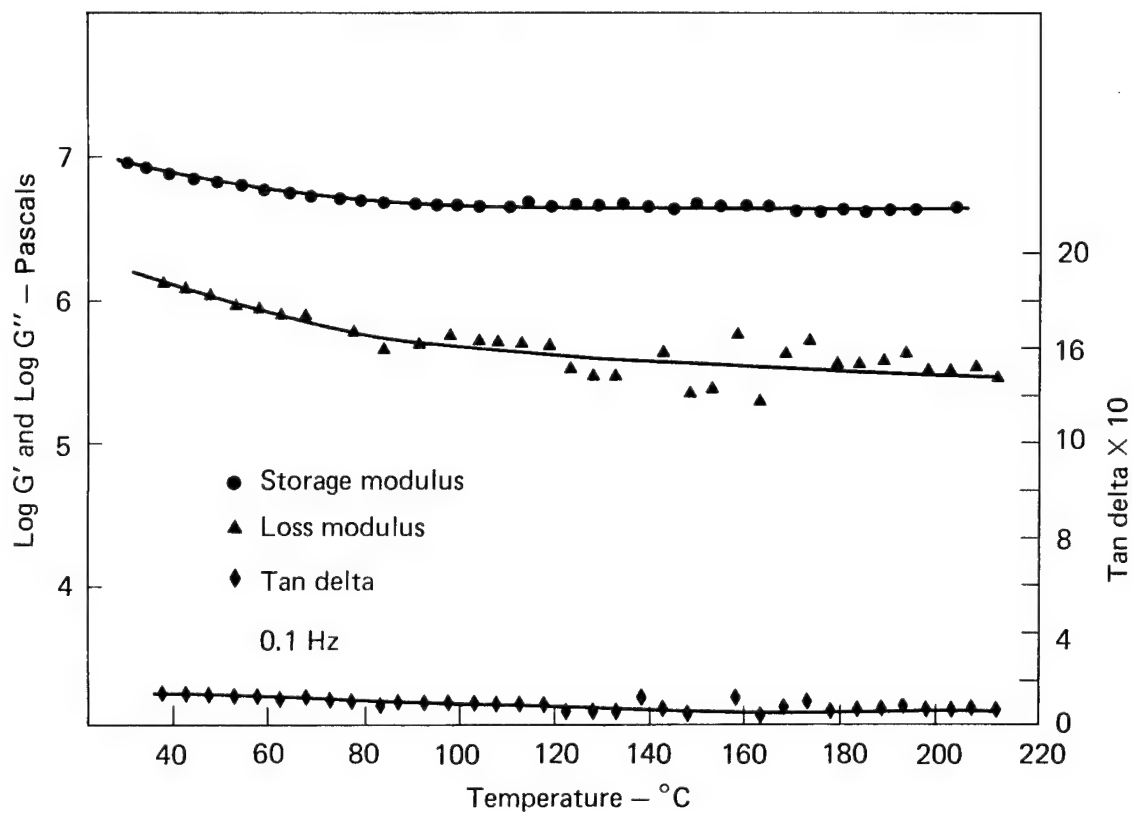


Figure 17 Storage modulus (G'), loss modulus (G''), and tan delta (δ) plotted versus temperature (40°C to 220°C). Data determined in low strain torsion experiments.

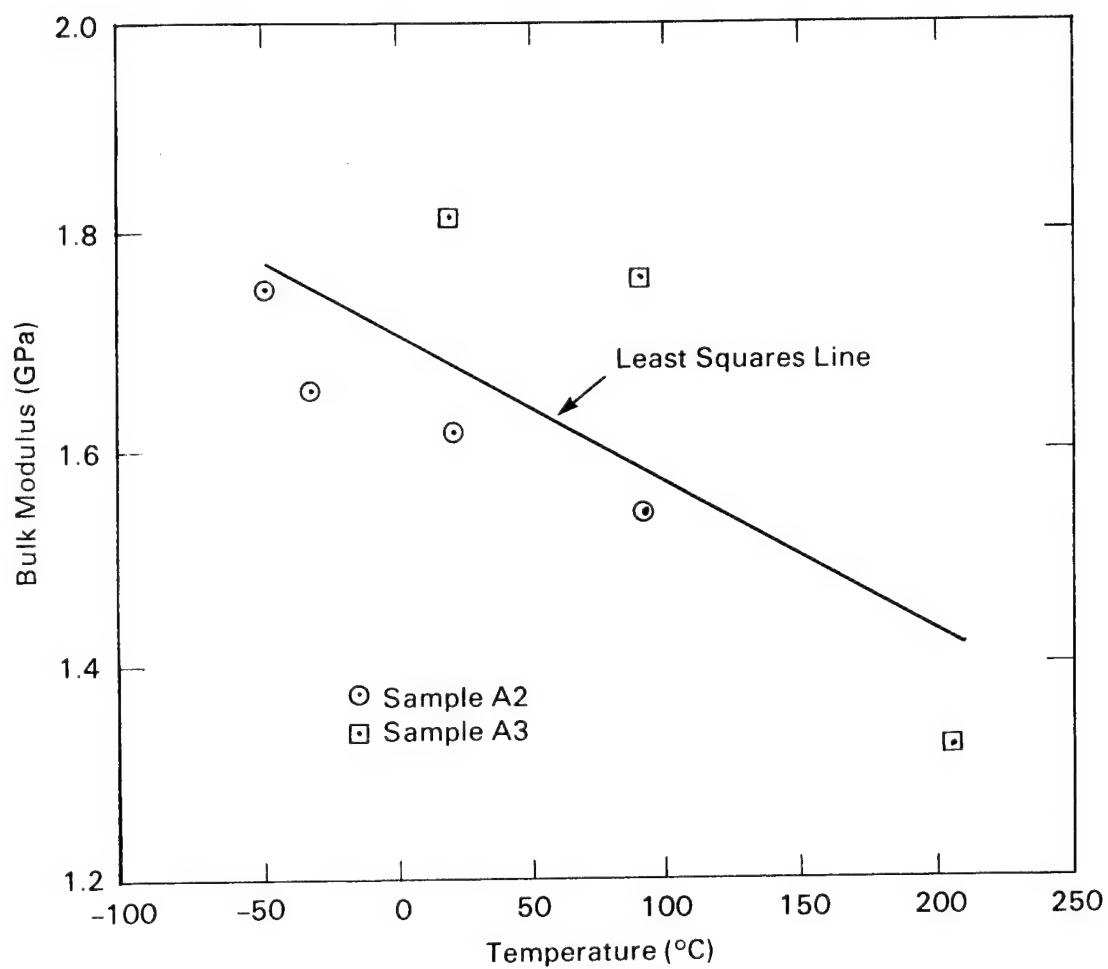


Figure 18 Bulk modulus of SBR as a function of temperature.

TABLE 4

CARBON BLACK IN SBR FROM VENDER A

Sample	% Carbon Black	
	<u>1st Test</u>	<u>2nd Test</u>
A	36.5	36.5
B	34.9	35.0
C	34.8	35.1
D	35.7	35.6

2-3a(2). Thermogravimetric Analysis: A sample of tread from a tank track shoe manufactured by Vender A was analyzed using a Perkin Elmer Thermogravimetric System. Such a system enables one to measure weight changes as a sample is heated at some arbitrary rate in an atmosphere. Such an analysis can provide insight into chemical changes that are occurring in the tread rubber. For this study, a sample was heated at $10^{\circ}\text{C}/\text{min}$ ($18^{\circ}\text{F}/\text{min}$) in a nitrogen atmosphere. The percent weight lost by the sample as a function of temperature is shown in Figure 19. Three weight loss intervals can be detected and are shown in Table 5. At 200°C (392°F), the sample had lost approximately 0.4% weight.

2-3b. Physical - Differential Scanning Calorimetry: A sample of tread rubber from a tank track shoe manufactured by Vender A was analyzed using the differential scanning calorimeter (DSC) between the temperatures -75°C (-103°F) and 200°C (392°F). The DSC measures the amount of heat absorbed or evolved as the sample is heated through the temperature range of interest. The measurements enable one to calculate the heat capacity of the material as previously reported in Table 3. We are also interested in the glass transition temperature (T_g) and any significant exotherms and endotherms encountered during the temperature scan. The glass transition temperature was found to be -46°C (-51°F). The material also exhibited an endotherm between 31°C (88°F) and 80°C (176°F).

2-3c. Mechanical

2-3c(1). Tear Resistance: The tensile behavior of elastomers containing a stress riser is generally characterized by a tear test. This test provides little basic information and its utility lies in ranking a material under different environments and comparing different materials. Different test configurations can be used for determining the tear resistance. The ASTM D-624-73 Die C (shown in Figure 20) was employed here. The sample was tensile loaded to failure. The tests were conducted for different specimen thicknesses,

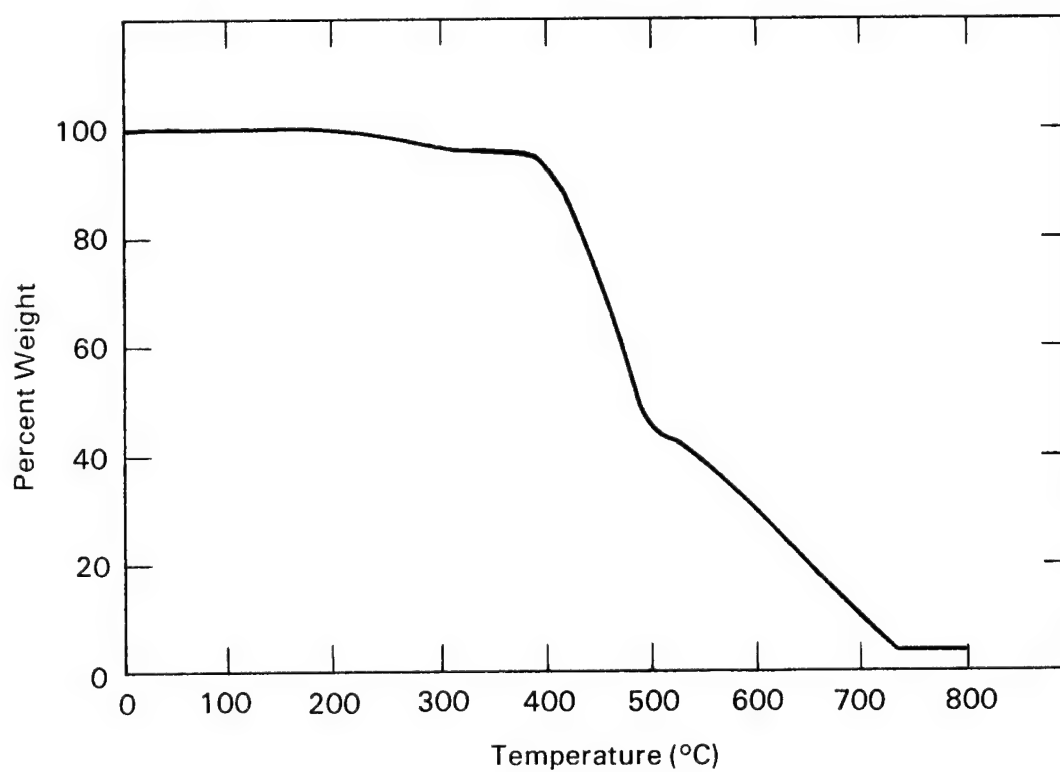
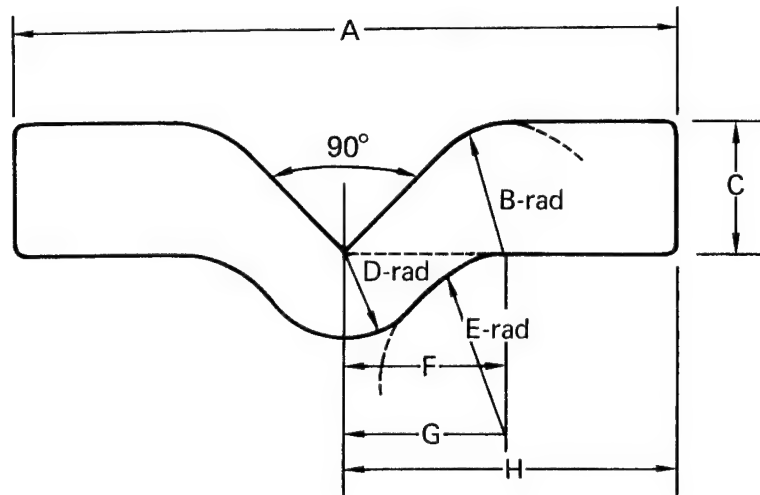


Figure 19 TGA plot showing percent weight lost by a sample of SBR as a function of temperature.

TABLE V

THERMOGRAVIMETRIC ANALYSIS OF SBR FROM VENDER A

Temperature °C	WEIGHT LOSS INTERVALS	
	% Weight Loss	Total % Weight Loss
120 - 380	5.0	5.0
380 - 525	52.5	57.5
525 - 740	39.0	96.5



Dimension	Millimetres		Inches	
	Value	Tolerance	Value	Tolerance
A	102	±0.50	4.0	±0.02
B	19	±0.05	0.75	±0.002
C	19	±0.05	0.75	±0.002
D	12.7	±0.05	0.5	±0.002
E	25	±0.05	1.0	±0.002
F	27	±0.05	1.061	±0.002
G	28	±0.05	1.118	±0.002
H	51	±0.25	2.0	±0.01

Figure 20 Sample used in tear resistance tests. Sample is per ASTM D-624-73 Die C.

loading rates, and temperatures. Samples tested and the results are presented in Table 6. Photographs of some of these samples are shown in Figure 21. The following observations can be made from the limited amount of data.

- o The effect of specimen thickness on tear strength was not discernible. The 5.1 mm (0.2 in) thick specimen (as opposed to 2.5 mm (0.1 in.)) was used in an attempt to approximate the three-dimensional stress field found in an actual shoe. The results suggest that a thickness of 5.1 mm (0.2 in.) is not large enough to observe the effects of a three-dimensional stress field.
- o The results show a rate effect with tear resistance decreasing with increase in rate.
- o The effect of elevated temperature on tear resistance is significant.

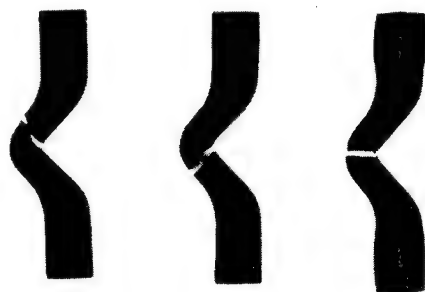
2-3c(2). Poisson's Ratio: The Poisson's ratio (ν) from Vender A tread rubber was evaluated in compression at temperatures of -55°C (-63°F), 22°C (72°F), and 149°C (300°F). At -55°C (-67°F) and 22°C (72°F) $\nu = 0.43$ and 149°C (300°F) $\nu = 0.48$. Evaluating Poisson's ratio involves measuring small transverse strains which is difficult, especially at high and low temperature. Thus, there is inherent error in the values reported. The trend of increasing Poisson's ratio with increasing temperature is correct since the material is more fluid at high temperature than at low temperature.

TABLE 6

ASTM D624-73 TEAR TEST RESULTS FOR SHOE NO. 1

Specimen Thickness, mm (Nominal)	Cross-Head Rate, mm/s	Temp °C	No. of Specimens	Average Tear Strength N/mm
5.1	8.5	22.2	1	45.7
5.1	0.085	22.2	1	54.8
5.1	0.85	22.2	4	51.5
2.5	0.85	22.2	5	49.9
2.5	0.85	204.4	5	13.7

(a)



(b)



Figure 21 Photograph of typical tear test fractures. Static fractures are shown in (a) while a fatigue fracture is shown in (b)

2-3c(3). WLF Equation: In a previous section, we presented data on the storage and loss modulus in shear and $\tan \delta$ at low strains as a function of temperature. Data were also generated on tread rubber from Vender A for five different frequencies (10, 3.1, 1, 0.32, 0.1 Hz) at temperatures between -153°C (-243°F) and 38°C (100°F). From these data, the constants in the Williams, Landel, Ferry equation (WLF equation) can be determined. This equation enables one to determine the shift factor for time-temperature superposition, and thus the shear moduli at temperatures and frequencies different from those used in Figures 16 and 17. The equation can be represented as

$$\log a_T = \frac{C_1(T - T_R)}{C_2 + (T - T_R)} \quad (3)$$

where

a_T = shift factor

T = temperature

T_R = reference temperature

C_1 = Constant

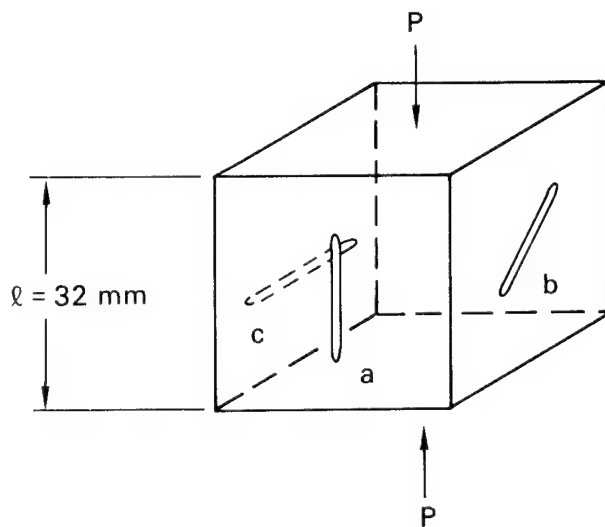
C_2 = Constant

Using a reference temperature of -51°C (-60°F) (approximately the glass transition temperature) $C_1 = 33.2$ and $C_2 = 103.3$. These values are only valid for about a 100°C (180°F) range above the glass transition temperature.

2-4. Failure Studies

2-4a. Mechanical Tests: In addition to the standard mechanical tests presented in the previous section, additional non-standard tests were done to study, in a preliminary way, the crack growth and fatigue in this material.

2-4a(1). Crack Growth: The behavior of the pad will be different for different loadings (tension, compression, shear, combined loads). Since it was not possible to investigate the different modes of fracture (Modes I, II, and III) during this phase of the study, it was decided to perform an exploratory compression/ compression fatigue test on a 31.8 mm (1.25 in.) cube machined from a shoe from Vender A (Figure 22). Flaws "a", "b", and "c" were implanted in a manner such that the crack tips would be subjected predominantly to tensile, shear, and compressive stresses, respectively. The tensile stresses in crack "a" arise due to the barreling of the cube. The cube was cycled between nominal stress values of 0.20 MPa (29 psi) and 2.98 MPa (430 psi) for 2,750,000 cycles at a frequency of 3 Hz. These stresses and frequency are representative of nominal values experienced by a uniformly loaded tank track pad. The amount of crack growth is indicated in Figure 22. A photograph of the actual cube is shown in Figure 23. Cracks "a" and "b" have extended beyond their original lengths, while crack "c" has not experienced any growth. Thus, both tensile stresses and shear stresses can propagate cracks in this material. However, very little can be concluded from the relative amount of growth in cracks "a" and "b", since the magnitude of the tensile stresses present in crack "a" are largely unknown. Relative to actual fracture of the sample, the amount of crack growth is small considering the large number of cycles employed.



$$P_{\max} = 3 \text{ kN}$$

$$P_{\min} = 0.2 \text{ kN}$$

$$f = 3 \text{ Hz}$$

$$N = 2,750,000 \text{ cycles}$$

$$= N_1$$

$$\text{Initial flaw size} = 19 \text{ mm}$$

$$\text{Initial flaw depth} = 10 \text{ mm}$$

$$\text{Rectangular shaped flaw}$$

$$\text{Crack 'a': } (a/l)_{N=1} = 0.6$$

$$(a/l)_{N=N_1} = 0.66$$

$$\text{Crack 'b': } (b)_{N=N_1} = 22 \text{ mm}$$

$$\text{Crack 'c': No growth}$$

Figure 22 Cube with implanted, oriented cracks used in compression-compression fatigue crack growth tests. Relevant parameters and results are indicated.

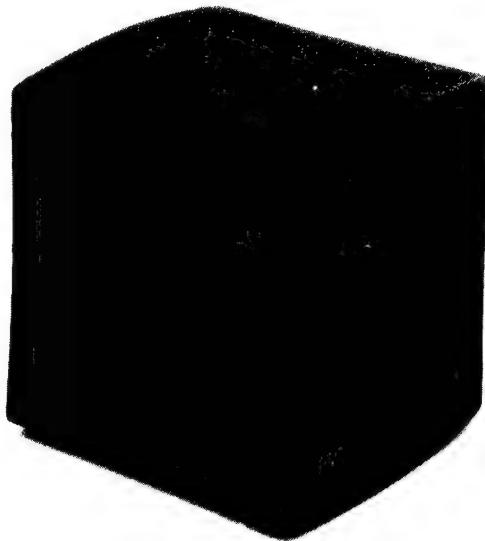


Figure 23 Photograph of cube used in fatigue crack growth experiments.
Cracks were implanted in all six faces

2-4a(2). Fatigue Tests: The objective of the fatigue tests was to develop an understanding of the fatigue response of the pad rubber material containing a stress concentration. To this end, fatigue tests were performed by cycling tear specimens between selected tensile loads until fracture. Specimens from two different shoes manufactured by Vender A were used. In the results reported below, these two shoes are designated shoe No. 1 and shoe No. 2. In all tests, the ratio between maximum and minimum tensile load (R) was 0.5 and the cycle frequency was 5 Hz. The temperature of the sample was monitored using a thermocouple as shown in Figure 24. The maximum tensile load used in the experiments is represented as a ratio between the maximum load and the static fracture load for a tear specimen (S). The static fracture load was measured for these samples and found to be 133 N (29.90 lbs). A plot of S versus number of cycles to failure is shown in Figure 25. Visual observation of the sample indicated that for all samples tested less than 1,000 cycles was needed for the formation of the first visible crack. The steady-state temperatures obtained are indicated in Figure 25. Figure 26 shows the temperature rise curve for a sample cycled to $S = 0.57$. The following conclusions can be drawn from these limited test data:

- o The steady-state temperature increases with S level.
- o There appears to be an endurance limit at $S = 0.5$.
- o The fatigue resistance of shoe No. 1 is better than shoe No. 2. This could be attributed to material variability.

A photograph of a sample after fracture is shown in Figure 21.

The fracture surfaces of both fatigue and static tear test specimens were examined in the scanning electron microscope. The fracture surfaces at two levels of magnification are shown in Figure 27.

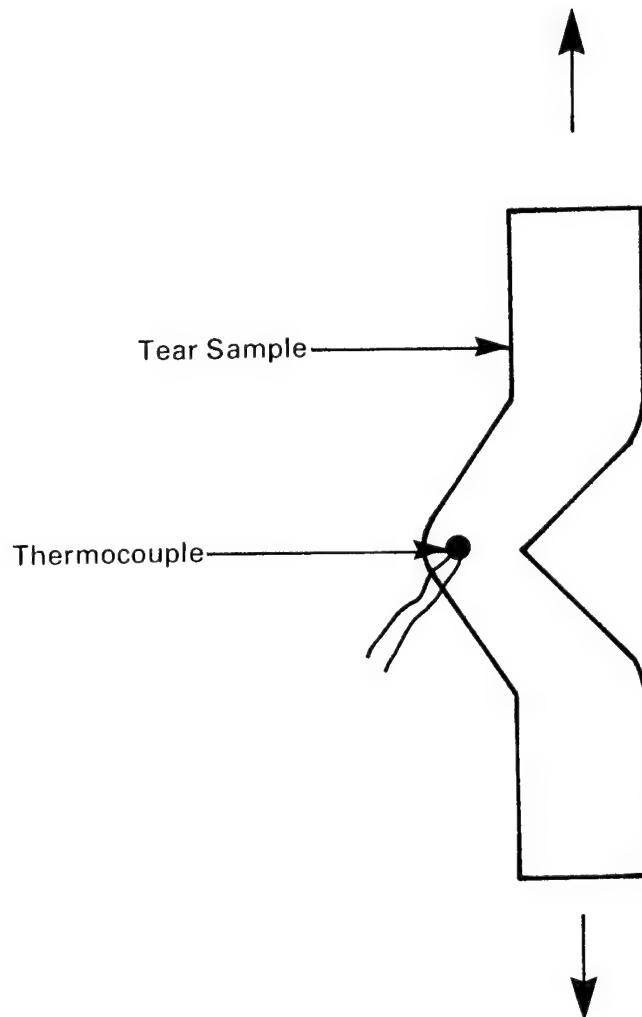


Figure 24 Tear specimen and thermocouple used in tension-tension fatigue tests.

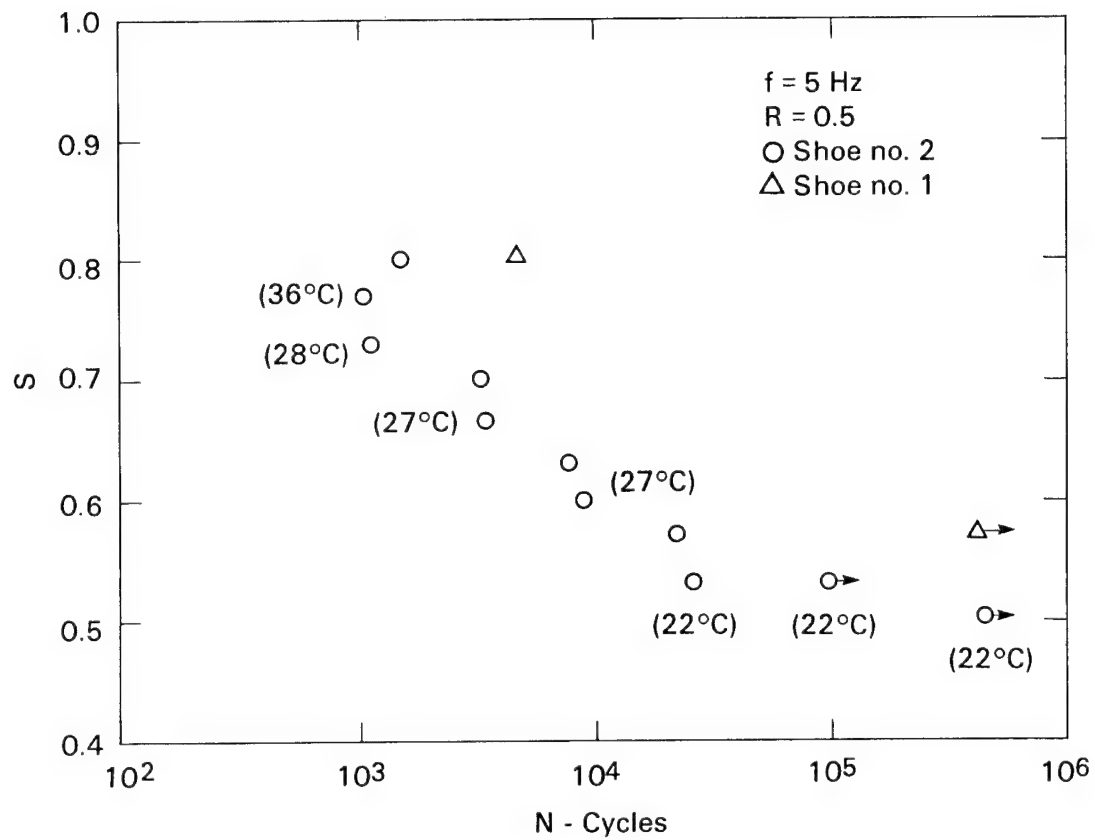


Figure 25 Fatigue strength versus number of cycles to failure for two different shoes from vender A. A tear specimen was used and its temperature is indicated in parentheses.

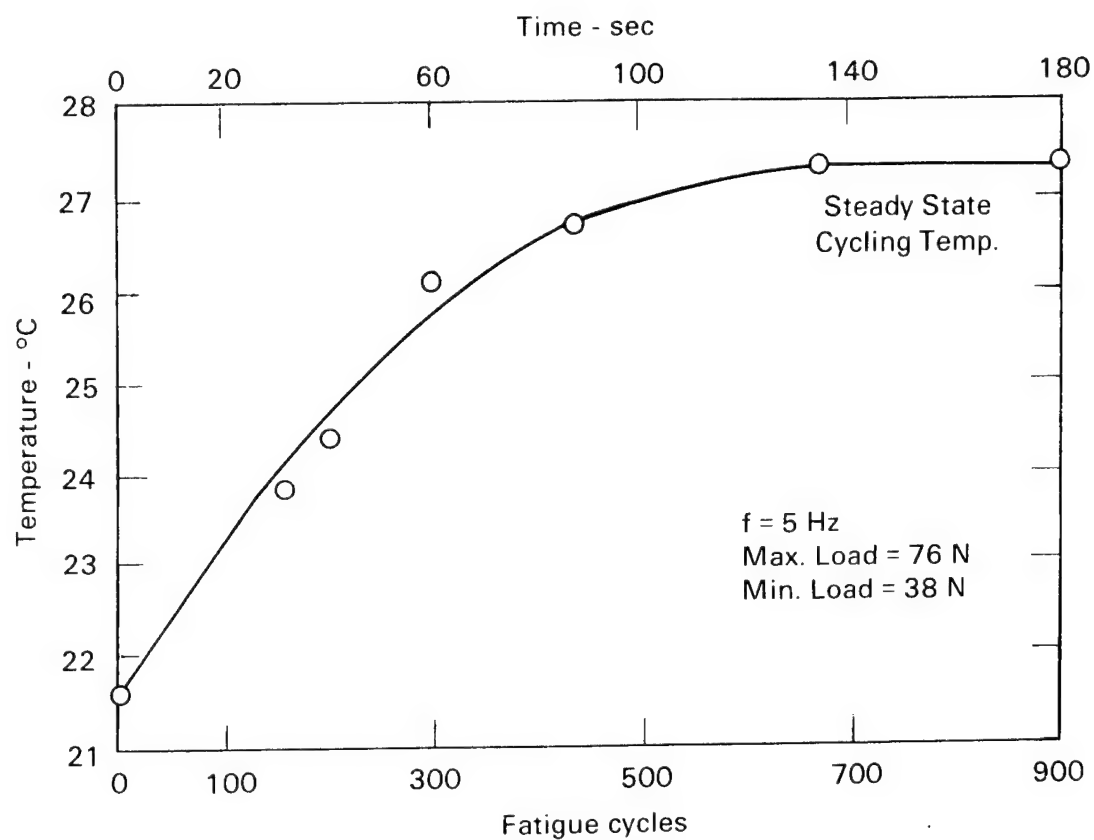
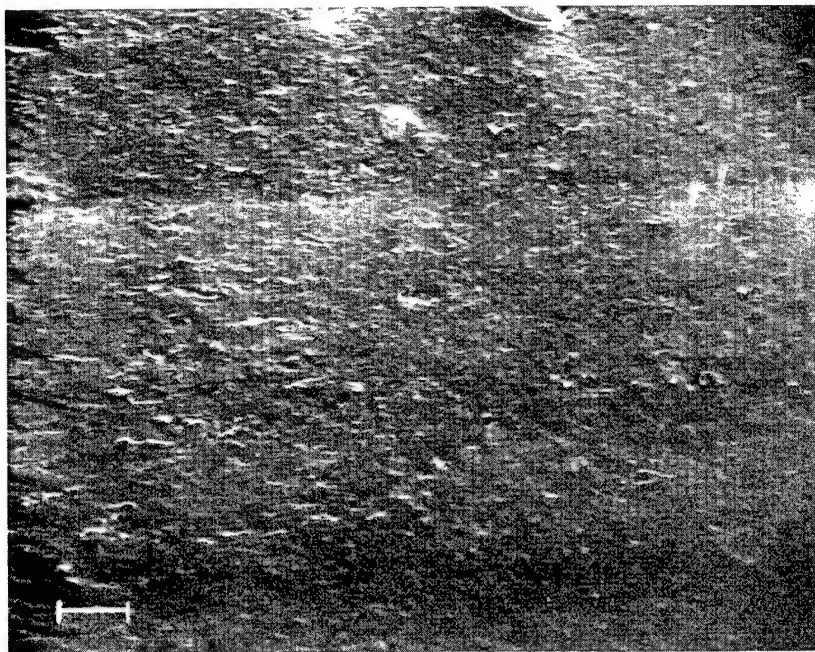


Figure 26 Temperature versus time curve for a tear sample cycled to $s = 0.57$

100 μm



1 μm

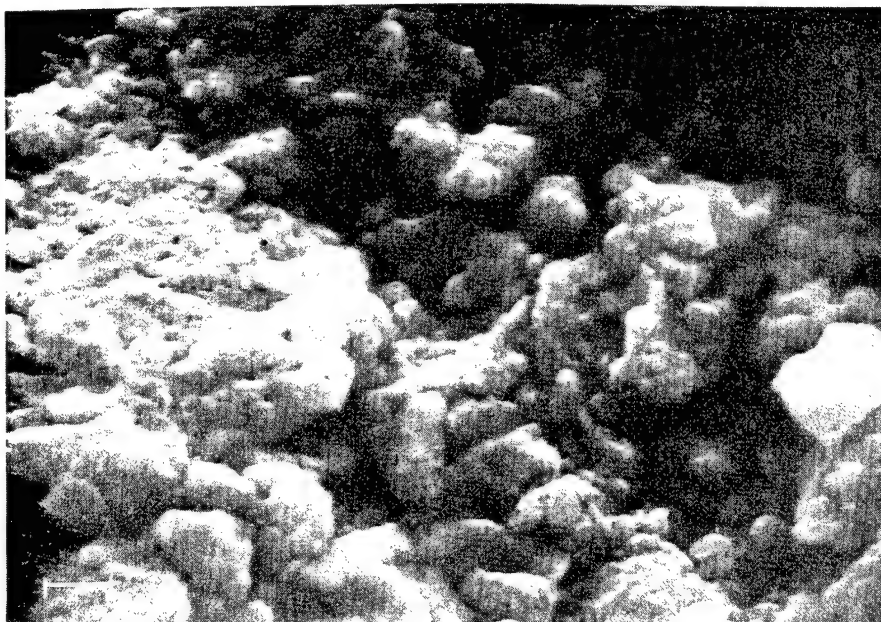


Figure 27-1 Fracture surface of static loaded tear specimen

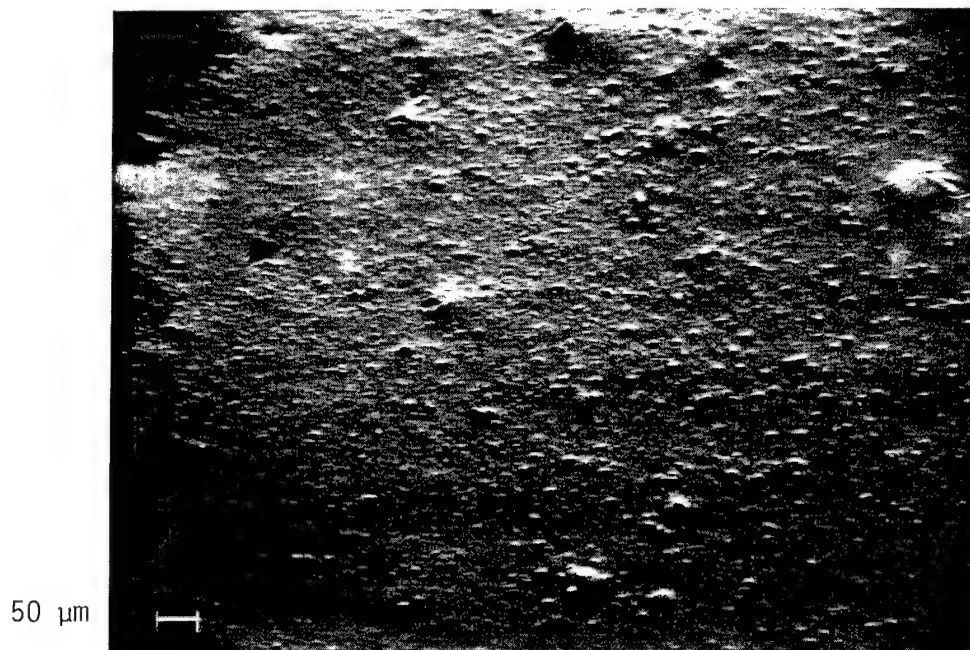


Figure 27-2 Fracture surface of fatigue loaded tear specimen

At low magnification, both static and fatigue fracture surfaces are relatively featureless. However, at higher magnifications, the static fracture surface shows distinct droplets or globules. This fracture morphology has been observed before in rubber fracture. In the fatigue fracture surface the globules are essentially absent.

2-4a(3). Residual Tear Tests: Residual tear tests were also conducted after cycling some specimens to a predetermined number of cycles. Such tests will provide insight into whether the fatigue loading is compromising the inherent tear resistance of the material. Samples were cycled for 10,000 or 100,000 cycles at $S = 0.57$. The subsequent tear strength is indicated in Table 7. Only three samples were tested and some scatter is evident. However, for $N = 10,000$ cycles, there does appear to be a decrease in residual tear resistance.

3. FY 80 ACTIVITIES

3-1. Field Analysis: Field testing of the T-142 tank track shoe was completed on May 13, 1980, at the Yuma Proving Grounds. The purpose of this testing was to obtain information which would assist in correlating field behavior of the tank pads to laboratory experiments and the computer modeling work previously described. This task was broken down into four main categories:

1. Measure pad temperature (surface and internal) and hardness as a function of tank speed, mileage, and running time;
2. Observe and measure wear pattern on pad;
3. Observe pad, track, and tank motion during operation;
4. Study various terrains on which the pads are being tested.

TABLE 7

RESIDUAL TEAR TEST RESULTS (ROOM TEMPERATURE - 24°C)

Specimen No.	Cross-Head Rate, mm/s	Specimen Thickness, mm	Fatigue History	Failure Load Nt	Tear Strength N/mm
2-17-C	0.85	2.49	S=0.57, R=0.5 N=10 ³	110	44.3
2-17-D	0.85	2.49	S=0.57, R=0.5 N=10 ³	128	51.3
2-17-F	0.85	3.05	S=0.57, R=0.5 N=10 ⁴	130	42.6

An M103 tank with predominantly T-142 tank track shoes was used during the field testing. The paved Yuma test track, reported to be approximately 8 km (5 miles) long, was used for the current set of tests. The tank was driven at 32 km/hr (20 MPH), and measurements were taken after stopping the tank every 4 km. Temperatures were measured at the pad's surface by a commercial surface thermometer and at the interior of the pad by thermocouples which were injected by a specially constructed pneumatic ram apparatus (Figure 28). Air and pavement temperatures were also monitored.

The thermometers were calibrated in the laboratory using sections of rubber cut from a T-142 pad (Figure 29). The pad section was heated in water until the internal and bath temperatures were the same. The pad section was then removed from the bath. An internal temperature measurement was quickly made with the injection thermocouple apparatus. The injected thermocouple data were then compared to the bath temperature. Actual pad temperatures were higher than the measured temperatures. The maximum difference was 10°C (18°F) at 100°C (212°F) (Figure 30).

The surface thermometer was calibrated in a similar manner. The temperature of the probe was compared with the foil thermocouple which was bonded to the surface of the pad section. The differences between these two readings were relatively large and were attributed to conductive heat loss from the rubber surface into the surface probe. Because of this premise, surface temperature error was related to the difference between actual surface temperature and ambient (in air) surface thermometer temperature as measured by the thermometer itself. This error is shown in Figure 31.

Test pads were chosen to provide a distribution of "previous" mileage and manufacturer. Five pads from Vender C with varying mileage, were used in the first test. These included: one with 720 km (450 miles), three with 1530 km (950 miles), and one with 2,330 km (1,450 miles). In the second test, pads from Venders A and B, each with 3,200 km (2,000 miles), were employed. The test procedure was as follows:

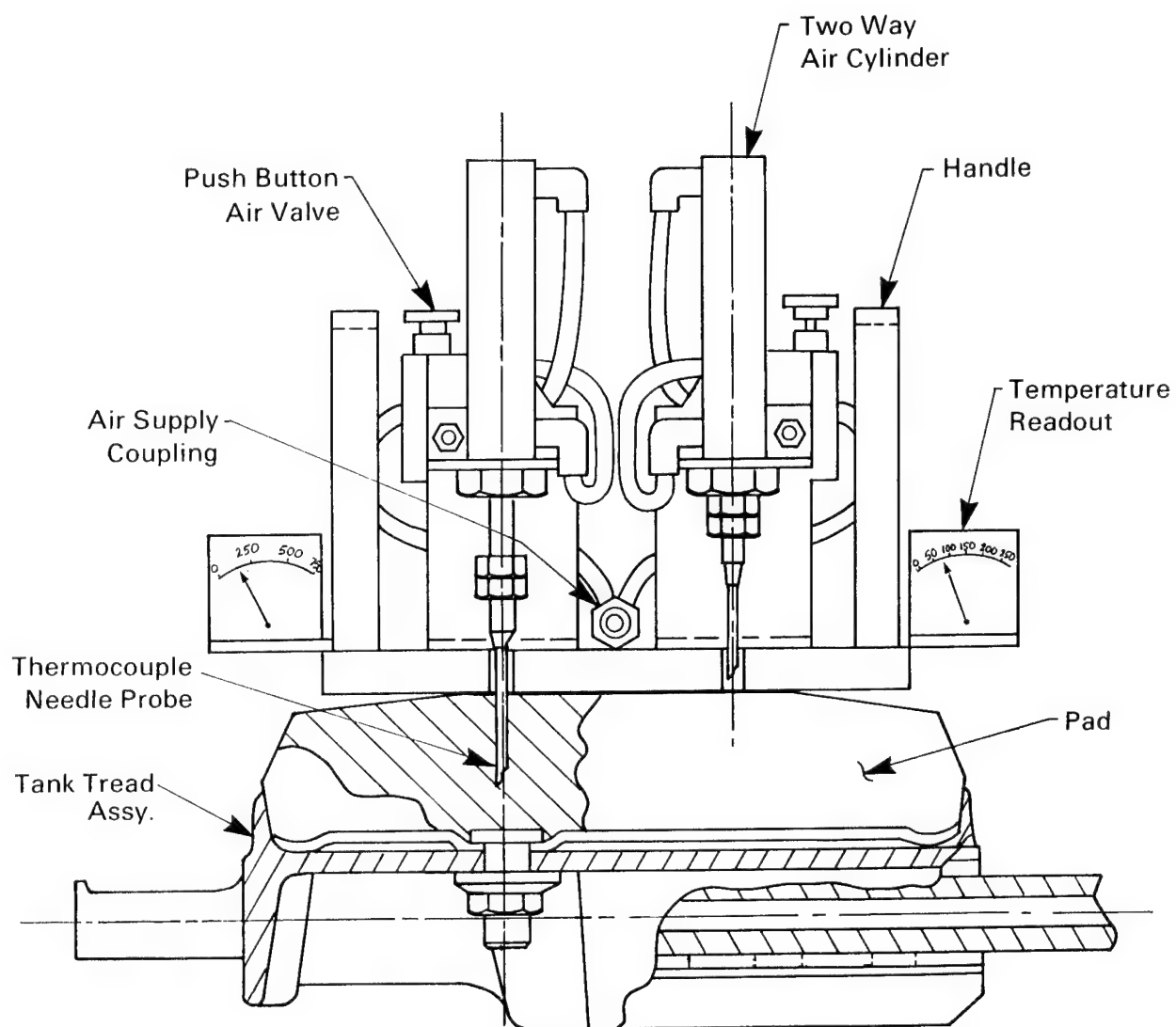


Figure 28 Thermocouple injector for internal pad temperature measurements in the field.

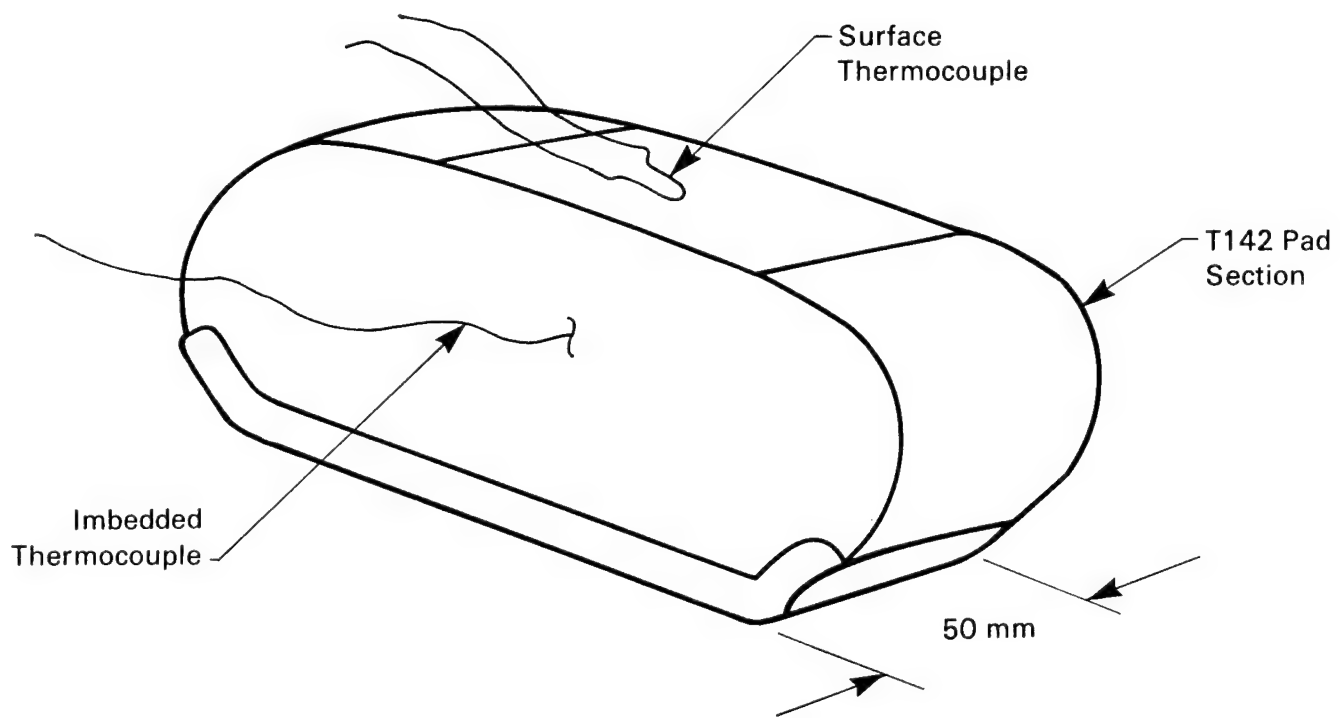


Figure 29 Thermocouple calibration pad section.

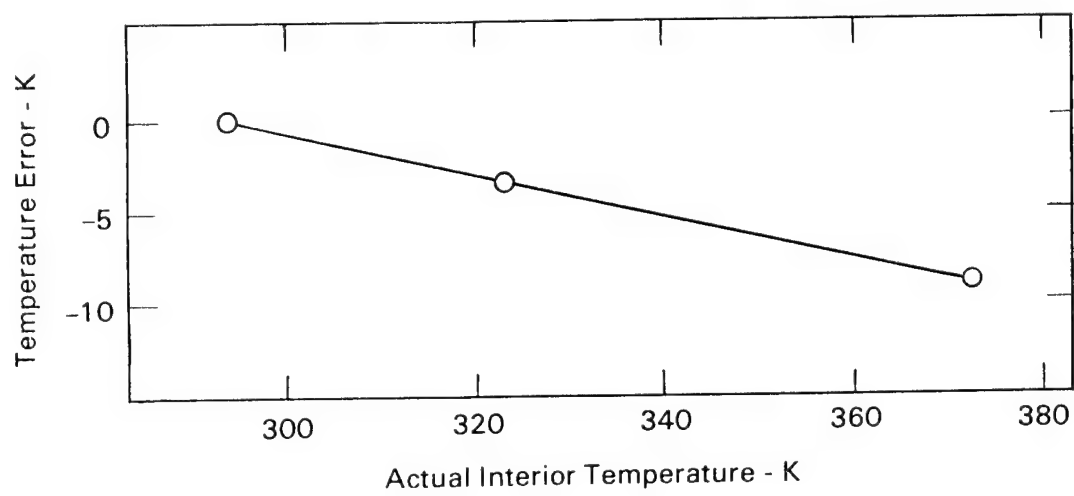


Figure 30 Internal temperature measurement errors.

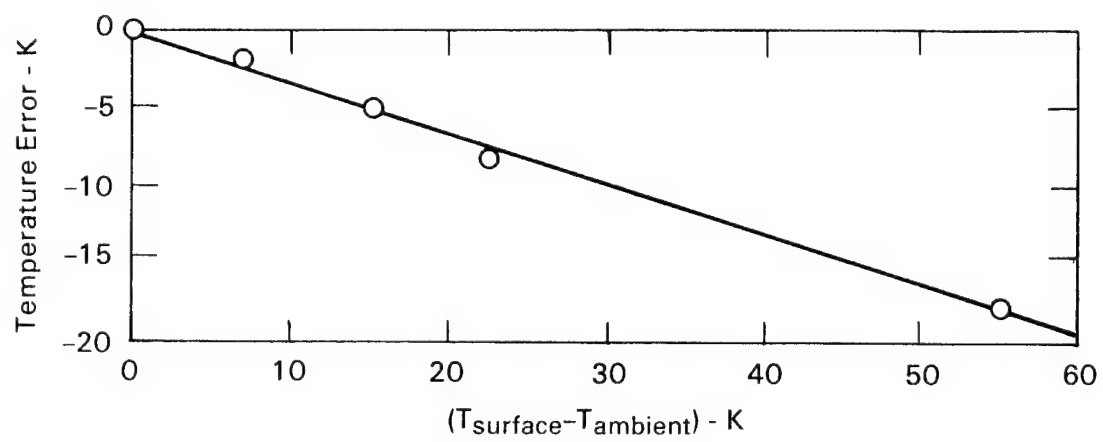


Figure 31 Surface temperature measurement errors.

1. Measure initial conditions

- Surface temperature
- Internal temperature, depth 15.9 mm (0.625 in.)
- Durometer hardness
- Visual inspection
- Air temperature
- Ground temperature

2. Run the tank the per prescribed schedule, (See Table 8). Record length of run time and mileage.

3. Stop -- Measure the pad temperature and hardness on each of the test pads. (Note: Pads were not left on ground since this will tend to cool the surface quickly.)

4. Record the length of time the tank is stopped.

5. Return to No. 2.

Test results for pads from Vender C are shown in Figure 32 for both internal and surface temperatures. Test results are expressed as pad temperature versus time. No significant relationship could be drawn between pad mileage (prior to the current test) and heat-up rate. Further, during the few minutes stop-time in which measurements were made, no appreciable temperature drop was observed. The results for pads from Venders A and B showed that correlation of temperature curves for the three manufacturers were excellent for surface temperature (maximum deviation was 1°C (2°F)); whereas, the 15.9 mm (0.625 in) penetration temperature exhibited some variation (maximum deviation was 7°C (13°F)).

The following data and observations were obtained:

1. Air temperature ranged from $27-30^{\circ}\text{C}$ ($80-86^{\circ}\text{F}$) during the testing of pads from Vender C and increased to about 34°C (93°F) later in the day for the testing of pads from Venders A and B. The pavement temperature was between 47.4 to 50.5°C ($118-123^{\circ}\text{F}$) for all tests.

TABLE 8
TEST SCHEDULE

Trial No.	Mileage	Approx. Running Time (km)	Comments
1	0	0 sec	Initialize
2	4.0	420 sec	
3	8.0	975 sec	
4	16.1	1895 sec	Heat-Up
5	24.1	2805 sec	
6	32.2	3735 sec	
7	40.2	4640 sec	
8	48.3	5550 sec	
9	48.3	5700 sec	
10	48.3	6475 sec	Cool-Down
11	48.3	7525 sec	

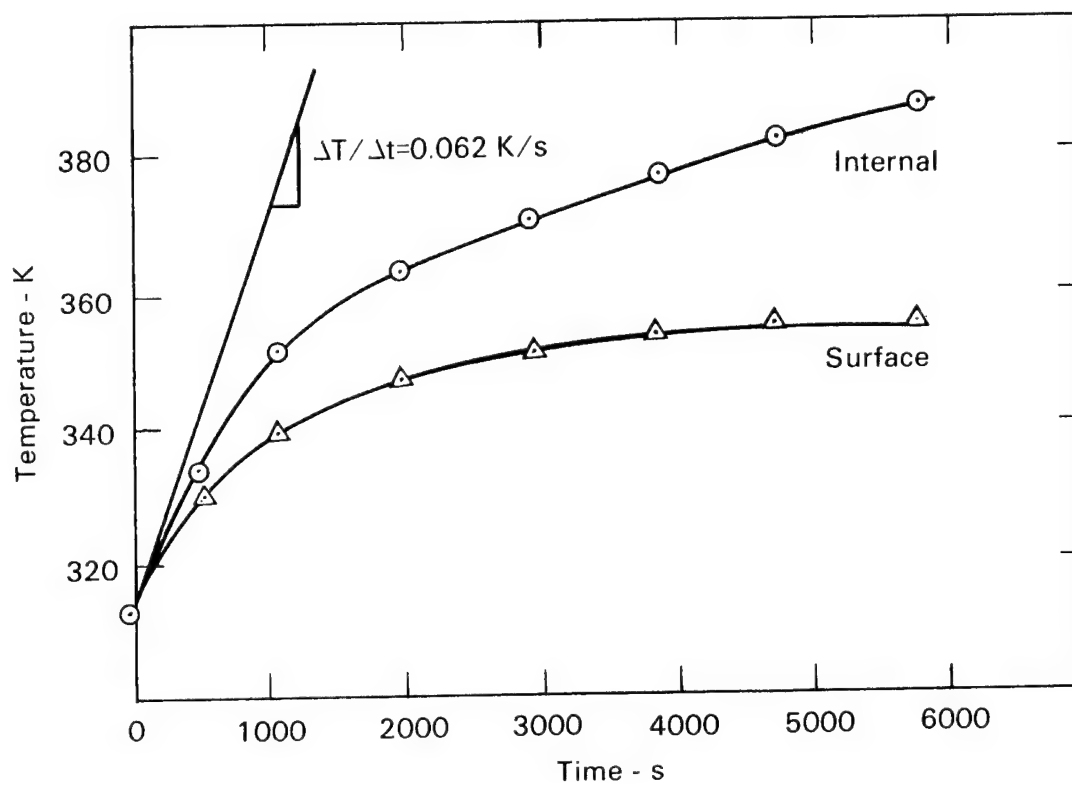


Figure 32 Internal and surface temperature versus time for pads from vender C tested at the Yuma Proving Grounds.

2. After 5,550 seconds (1.5 hrs) at about 32 km/hr (20 MPH) (calculated @ 37 km/hr (23 MPH)) the pad temperature still increases. The steady-state temperature at the interior of the pad could not be deduced from this data.

3. The durometer hardness did not vary significantly throughout the test. Average values were around 57 to 58.

4. Primary wear and chunking occurs along trailing edge of pad with respect to roadwheel motion (Figure 33). Wear on this edge was as much as 6.4 mm (0.25 in.) more than forward edge.

3-2. Analytical Work

3-2a. Temperature Analysis

3-2a(1). Material Properties: In the FY 79 report, relevant thermal properties required for using the TACO code were presented. The heat generation rate was determined from data resulting from other studies.¹ However, this property is sensitive to composition and processing practices; thus, the hysteretic heat generation rate was determined for a sample of tread rubber from Vender A. The sample, a right circular cylinder with a diameter of 13 mm (0.5 in.) and a length of 25 mm (1 in.), was subjected to sinusoidal loading in compression between stress levels of 0.18 MPa (26 psi) and 2.1 MPa (305 psi) at a frequency of 2 Hz. Thin pieces of Teflon sheets were placed between the end faces of the sample and the compression surfaces to reduce the effects of friction. The load level and frequency are representative of those experienced by tank track shoes. The temperature change in the sample (produced due to hysteretic heat generation) was monitored as a function of time with a thermocouple. Experimental details are presented in Appendix A.

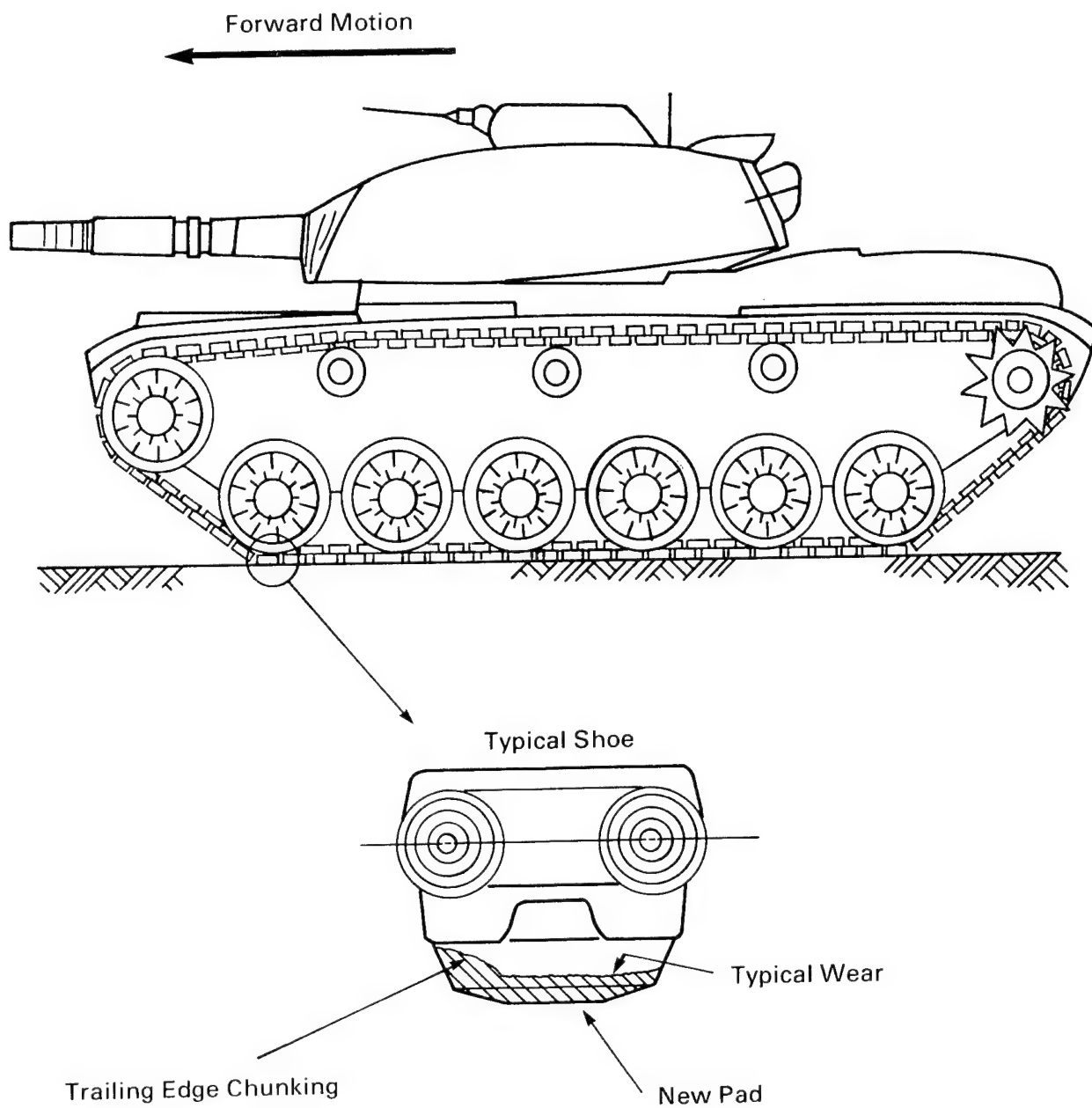


Figure 33 Pad wear observations for T-142 tank track.

The load-displacement data obtained in these experiments are shown in Figure 34. The hysteretic heat generation rate can be obtained in two ways. The first method employs the load-displacement data shown in Figure 34. The mechanical energy dissipated in the material is a function of the area within the loop. This mechanical energy loss becomes heat within the sample. This approach produced a value of 121 kW/m^3 ($11.7 \times 10^3 \text{ Btu/hr ft}^3$). The second method for obtaining the hysteretic heat generation rate is from the temperature-time curve illustrated schematically in Figure 35. The heat flow equation for an object which is internally generating heat is

$$K \nabla^2 T + \dot{Q} = \rho C_p \frac{dT}{dt} \quad (4)$$

where K = thermal conductivity
 T = temperature
 \dot{Q} = heat generation rate
 ρ = density
 C_p = specific heat

If the object is initially at the same temperature as its surroundings and suddenly starts to generate internal heat at a rate \dot{Q} , its initial temperature rise $(dT/dt)_{t=0}$ is $\dot{Q} / \rho C_p$. This happens because at $t = 0$ there are no temperature gradients, therefore $\nabla^2 T = 0$. Also, at early times just after $t = 0$, the value of $K \nabla^2 T$ may still be very small allowing the temperature history to continue following the path $\dot{Q} / \rho C_p$ for a short time period. The duration of this linear behavior depends on material properties, heat generation rate and geometry of the object. The slope $\Delta T / \Delta t$ shown in Figure 35 is equivalent to $(dT/dt)_{t=0}$. Thus heat generation can be calculated by the relation

$$\dot{Q} = \rho C_p (\Delta T / \Delta t). \quad (5)$$

This method produced a heat generation rate of 96 kW/m^3 ($9.3 \times 10^3 \text{ Btu/hr ft}^3$).

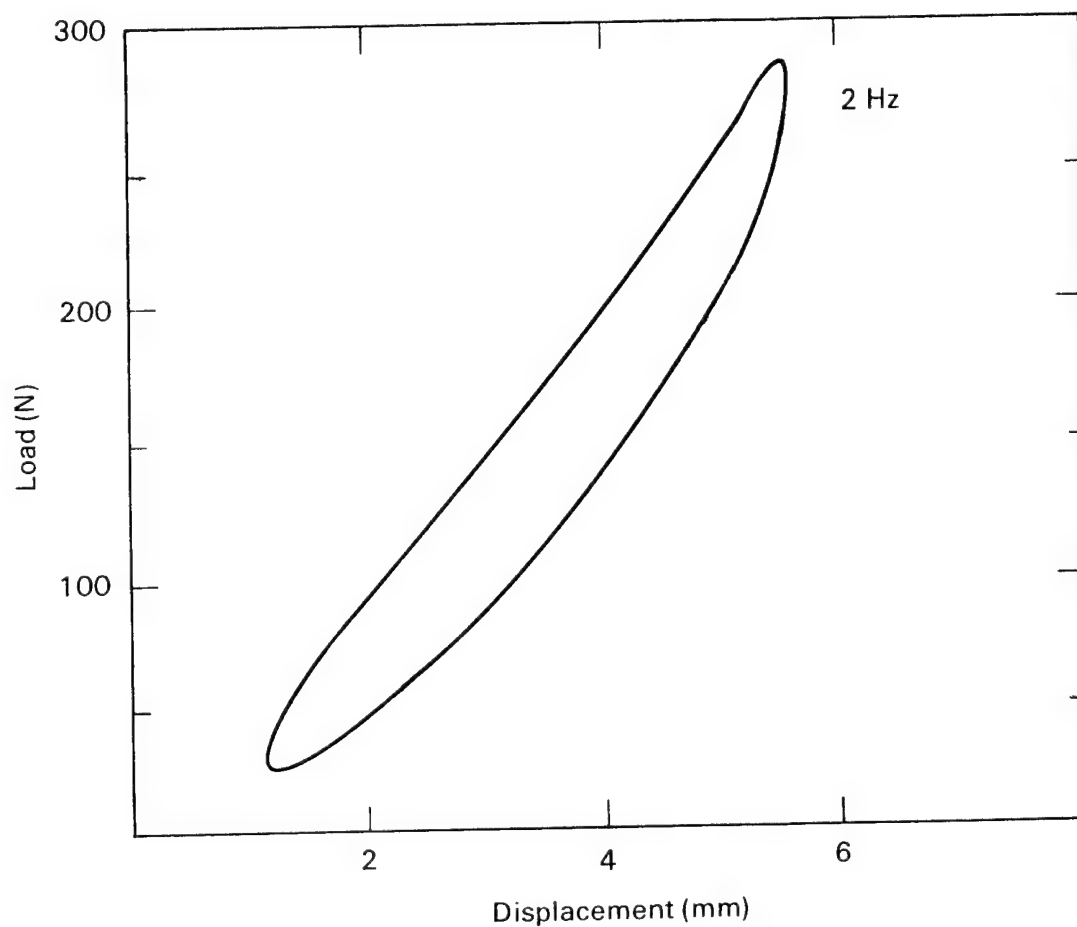


Figure 34 Load-displacement data for compression-compression fatigue test between the stress levels of 0.18 MPa (26 psi) and 2.1 MPa (305 psi) at a frequency of 2 Hz

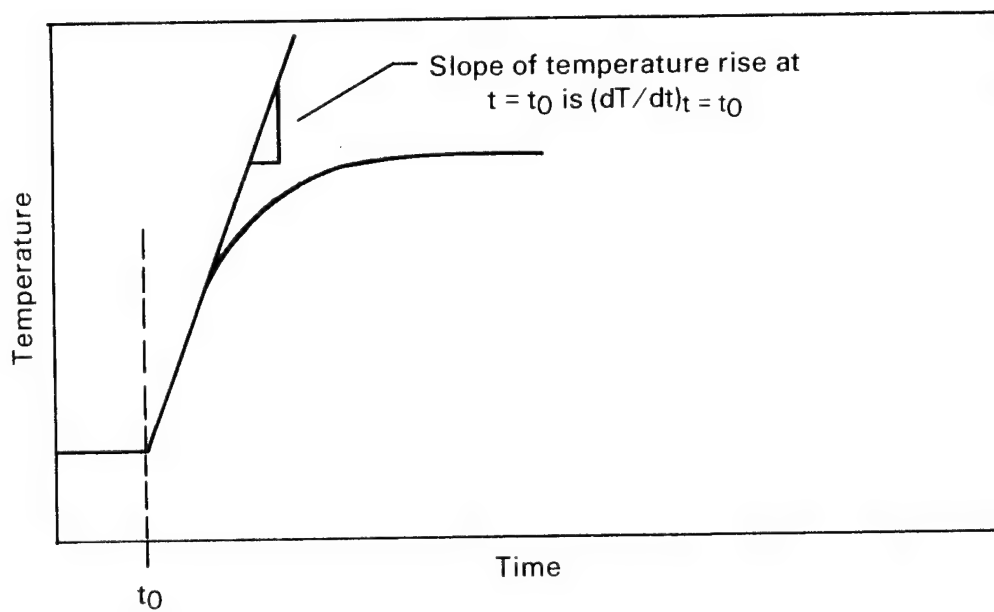


Figure 35 Schematic temperature-time curve illustrating determination of Q from the local temperature rise at $t = 0$ seconds.

The most reliable value of hysteretic heat generation rate (Q) was obtained from field test data. The hysteretic heat generation rate is a function of strain amplitude, stress state, and loading frequency. Thus Q can best be obtained on full-sized pads under actual vehicle loading conditions. The field data in Figure 32 was analyzed using Equation 5. The heat generation rate was found to be 108 kW/m^3 ($10.4 \times 10^3 \text{ Btu/hr ft}^3$). This value will be used in all subsequent thermal calculations.

The heat capacity for the tread rubber from Vender B was evaluated using differential scanning calorimetry. The values were determined on two samples as a function of temperature. Results are given in Table 9. The heat capacity measurements reported here are about 5 to 10% higher than values for Vender B reported earlier. The DSC scan noted a glass transition temperature of -42°C (-44°F) for both samples and an endotherm from about $75\text{--}100^\circ\text{C}$ ($167^\circ\text{--}212^\circ\text{F}$) peaking at 92°C (198°F).

The thermal conductivity for the tread rubber from a Vender B was evaluated using a four-inch diameter hot plate method. Experimental details are outlined in Appendix A. The values were determined as a function of temperature between -10°C (14°F) and 190°C (374°F). Results are reported in Table 10.

3-2a(2). Analysis: The finite element mesh used in the FY 80 thermal model is shown in Figure 36. Specifying thermal boundary conditions is a very important yet very difficult part of any temperature analysis. For the case of a moving tank, the pads are primarily cooled by conduction when they are in contact with the ground and by convection when the pads are off the ground. In addition, the heat transfer problem will be affected by films on the pad (such as dirt), pad condition, air movement, and air temperature. For this problem, convective boundary conditions were used. Such an approach provides a more realistic and generally applicable model than presented in the FY 79 report.

TABLE 9

HEAT CAPACITY FOR SBR FROM VENDER B

Temperature (°C)	Heat Capacity (J/kg °C) x 10 ³	
	Sample 1	Sample 2
-75	0.8351	0.8267
-50	0.9578	0.9619
-25	1.288	1.285
0	1.355	1.372
25	1.426	1.481
50	1.592	1.568
75	1.768	1.727
100	1.866	1.892
125	1.910	1.967
150	1.966	2.017
175	1.988	1.997
200	1.980	1.936

TABLE 10
THERMAL CONDUCTIVITY FOR SBR FROM VENDER B

Temperature (°C)	Thermal Conductivity W/m°C x 10 ⁻¹
-10	3.16
40	3.17
90	3.22
140	3.32
190	3.20

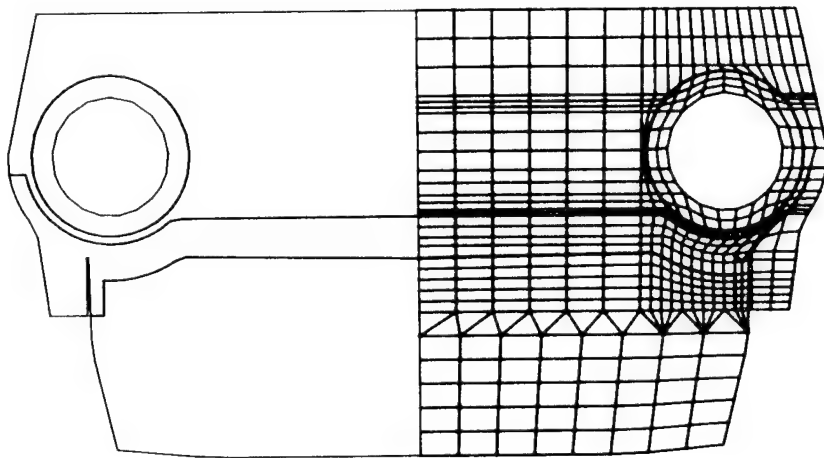


Figure 36 Finite element computer mesh used in the FY 80 thermal model.

The material properties required in the thermal analysis work were described in the FY 79 report. For this study, values representative of tread rubber from Vender B were used. The thermal conductivity was taken as $0.317 \text{ w/m}^0\text{C}$ ($0.183 \text{ Btu/hr ft}^0\text{F}$) (representative of values in Table 10), and the density was taken as 1.16 Mg/m^3 (72.4 lbs/ft^3). The heat capacity was used as a function of temperature from Table 9. The heat generation rate was also recognized to be a strong function of temperature. This is evident from the data on the variation of loss modulus with temperature (Figure 16). This data has been plotted in Figure 37 over the temperature range of interest. As described in a previous section, the heat generation rate is related to the mechanical energy dissipated in the material during cyclic loading. The energy dissipated per cycle (E) is in turn proportional to the loss modulus (G'') as defined by the following expression²

$$E = \pi G'' e_o^2 \quad (6)$$

Where e_o is the strain amplitude experienced during cyclic loading. Thus the heat generation rate (\dot{Q}) was taken to vary with temperature in the same manner as G'' as shown in Figure 38. The room temperature value of \dot{Q} was taken from the field data analyzed in the previous section. The information shown in Figure 38 represents a significant decrease in heat generation rate with temperature.

The convective heat transfer at the boundary is represented in TACO by the equation

$$q = h (T, t) (T - T_\infty) \quad (7)$$

where

- q = heat flow across the boundary
- h = convection film coefficient
- T_∞ = temperature
- T = equilibrium temperature (in our case, the air temperature)
- t = time

The boundary conditions used in this problem are shown in Figure 39. The heat transfer coefficient was selected so that the correct temperature-time

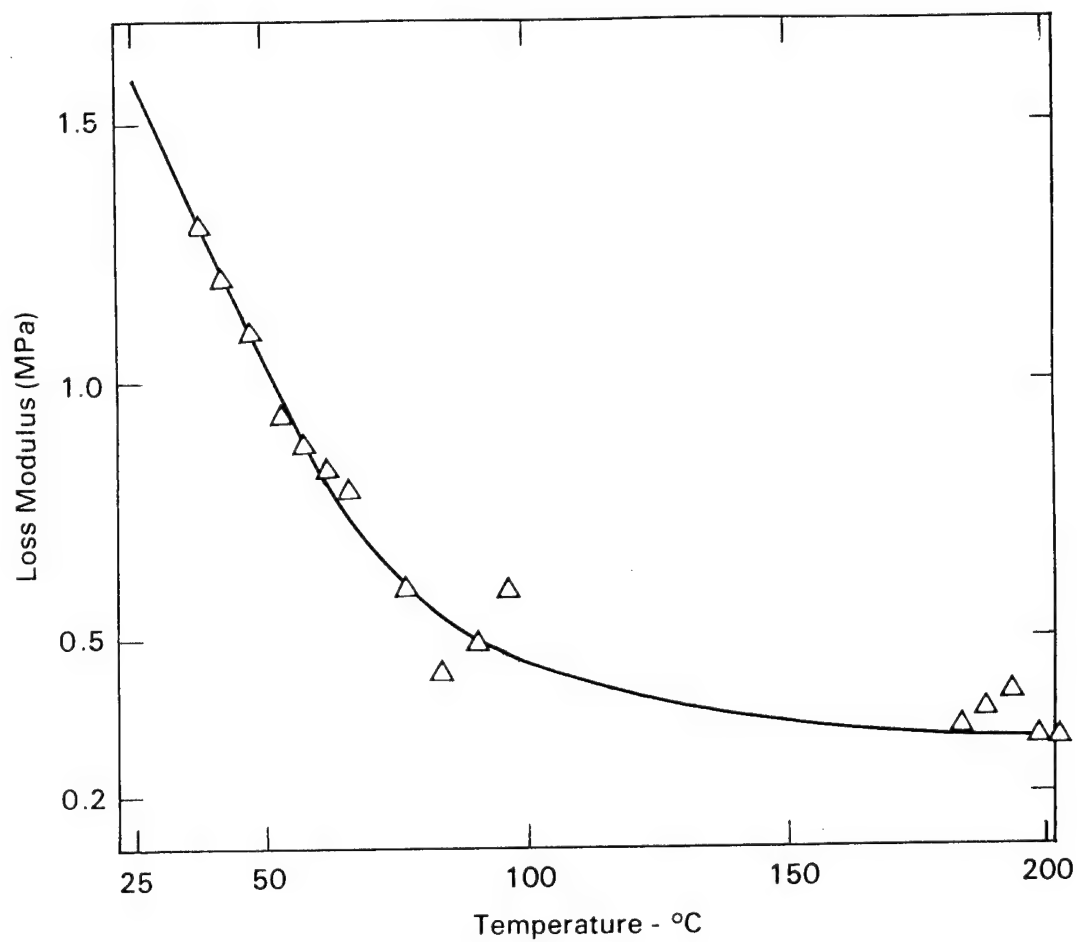


Figure 37 Loss modulus (G'') as a function of temperature over the temperature range of interest to the thermal model.

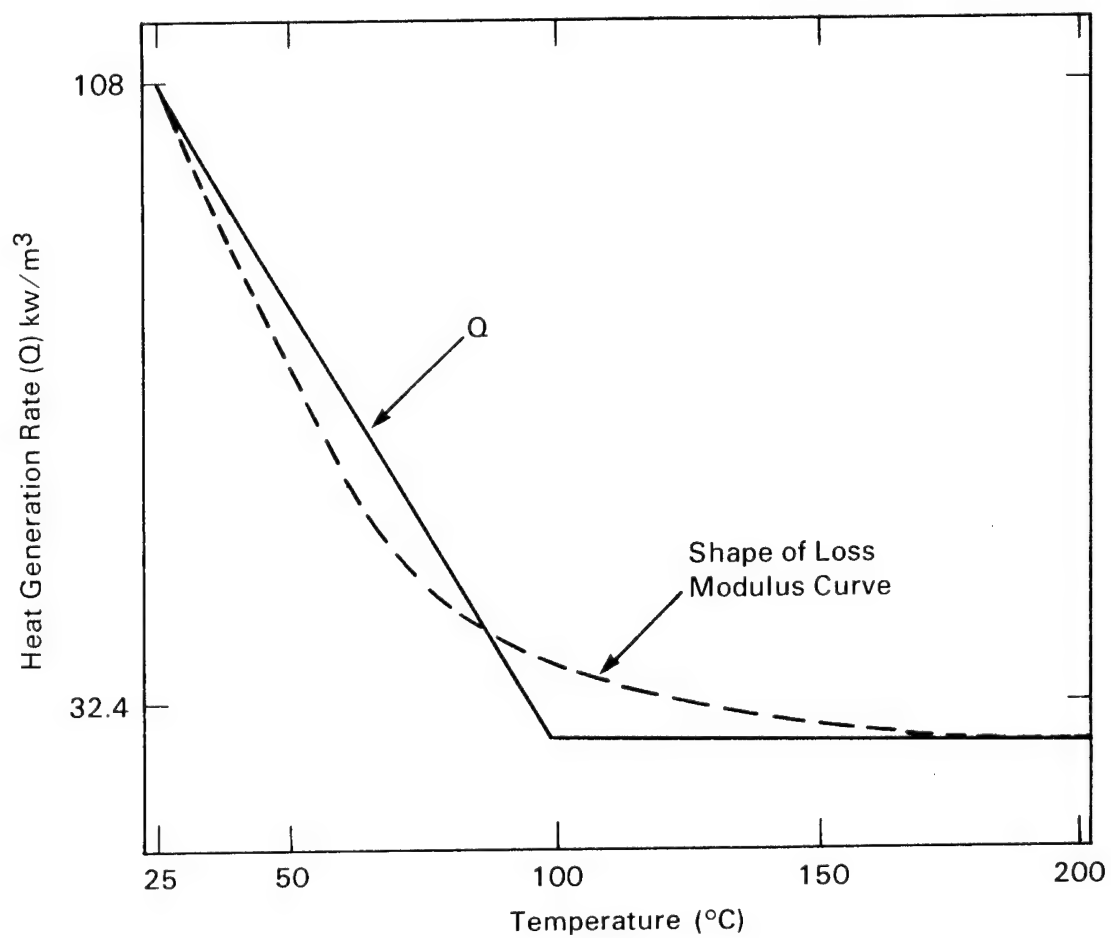


Figure 38 Variation of heat generation rate with temperature used in the thermal model. The loss modulus curve is from Figure 37.

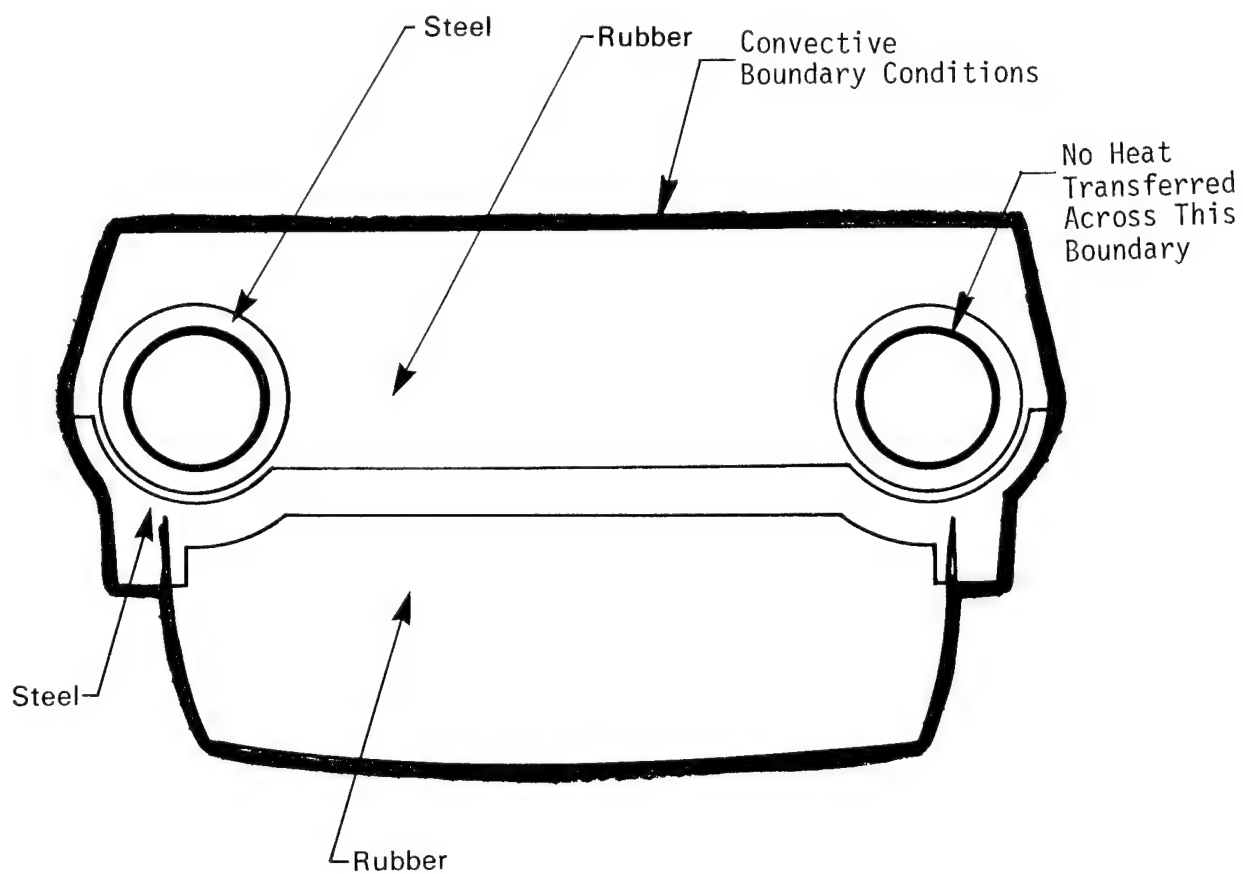


Figure 39 Boundary conditions used in the FY 80 thermal model.

profile was obtained as measured in the field and presented in Figure 32. The heat transfer coefficient obtained using this procedure was $17 \text{ W/m}^2\text{C}$ ($3.0 \text{ Btu/hr ft}^2\text{F}$). This value of h is within a factor of 3 of theoretical values that one can calculate from classical heat transfer theory assuming forced convection over a horizontal plate. Thus the value obtained has reasonable theoretical foundation. All external surfaces were assumed to convect heat in the same manner. The air temperature was assumed to be 35°C (95°F).

3-2a(3). Results and Discussion: The temperature-time response predicted by the thermal model for the interior of the pads shows excellent agreement with the temperature-time history measured in the field. The information is plotted in Figure 40. The solid curve represents the temperature-time measurements taken 16 mm (0.625 in.) below the surface of the pad, while the individual points represent the temperature-time response for the same point in the pad as predicted by the computer model. The difference between the actual data and the predictions of the thermal model are given in Table 11. The maximum deviation is 6°C (11°F). It is important to note the significant influence that the decreasing heat generation rate has on the temperatures achieved at the center of the pad. The TACO code was run with a constant heat generation rate, and the temperature-time response for a point 16 mm (0.625 in.) below the surface is presented in the figure. Notice that the temperatures for constant heat generation rate are significantly higher than those obtained for the decreasing rate. The condition of constant heat generation has produced an interior pad temperature of almost 200°C (392°F) after 5,500 s (1.5 hrs), whereas the decreasing rate has produced a temperature of 112°C (234°F). These results suggest that significant changes in the interior temperature of the pads can be obtained by decreasing the loss modulus over the temperature regime of interest.

Temperature profiles after 2,000 s (0.56 hr.), 4,000 s (1.11 hr.), and 6,000 s (1.67 hr) are shown in Figures 41, 42, and 43. One should note that for all three time intervals the maximum temperature in the pad and the road-wheel path are about equal. These maximum temperatures are 100°C (212°F)

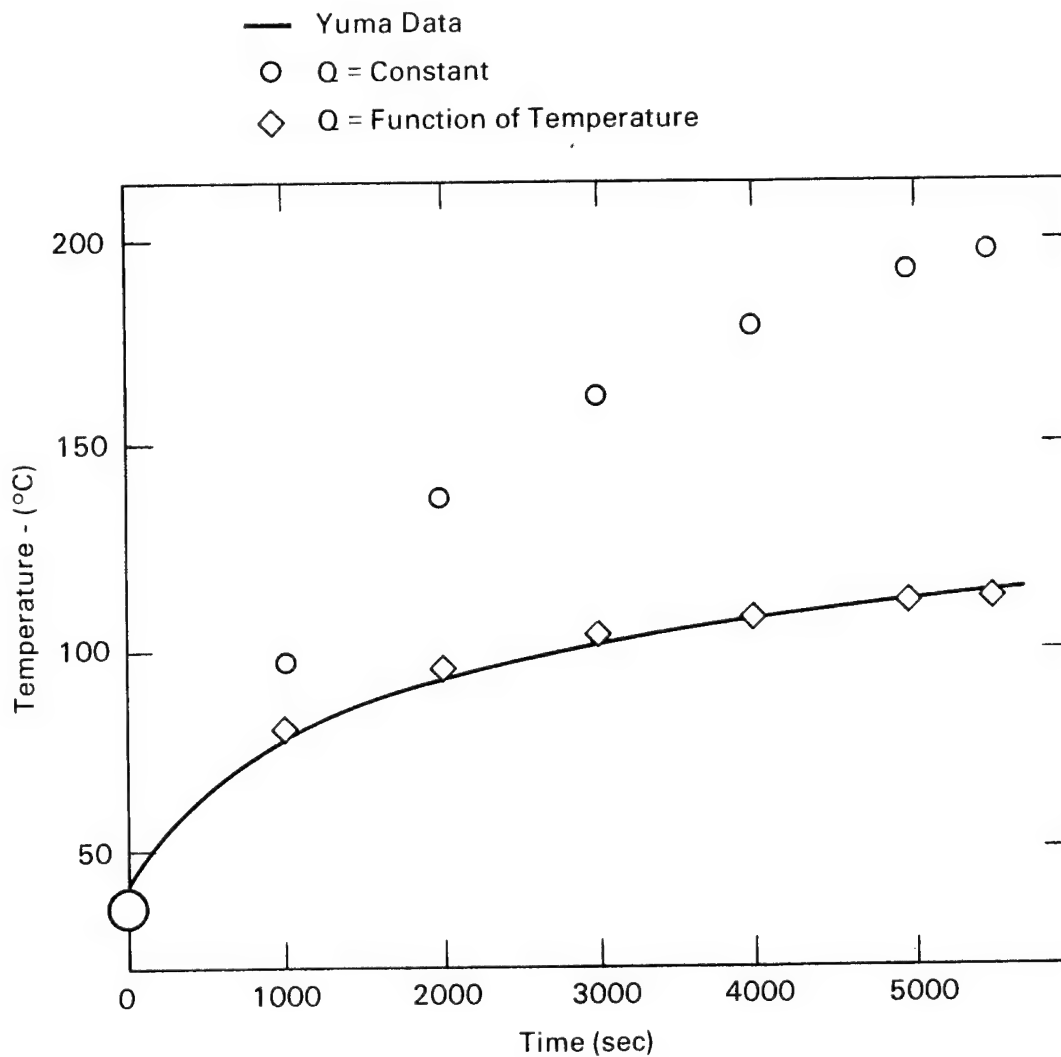


Figure 40 Temperature-time response for a point 16 mm (0.625 in.) below the surface of the pad as predicted by the thermal model using the heat generation rate from Figure 38. The temperature-time response measured during field testing is shown as a solid line. The predicted results show a maximum deviation of 6° C with the measured results. Also shown in the figure is the temperature-time response assuming a constant heat generation rate.

TABLE 11

TEMPERATURE DIFFERENCES BETWEEN MODEL
PREDICTIONS AND FIELD DATA

Time (s)	Temperature Difference °C $T_{\text{model}} - T_{\text{Yuma}}$
0	-
1000	1
2000	6
3000	6
4000	4
5000	4
5500	5

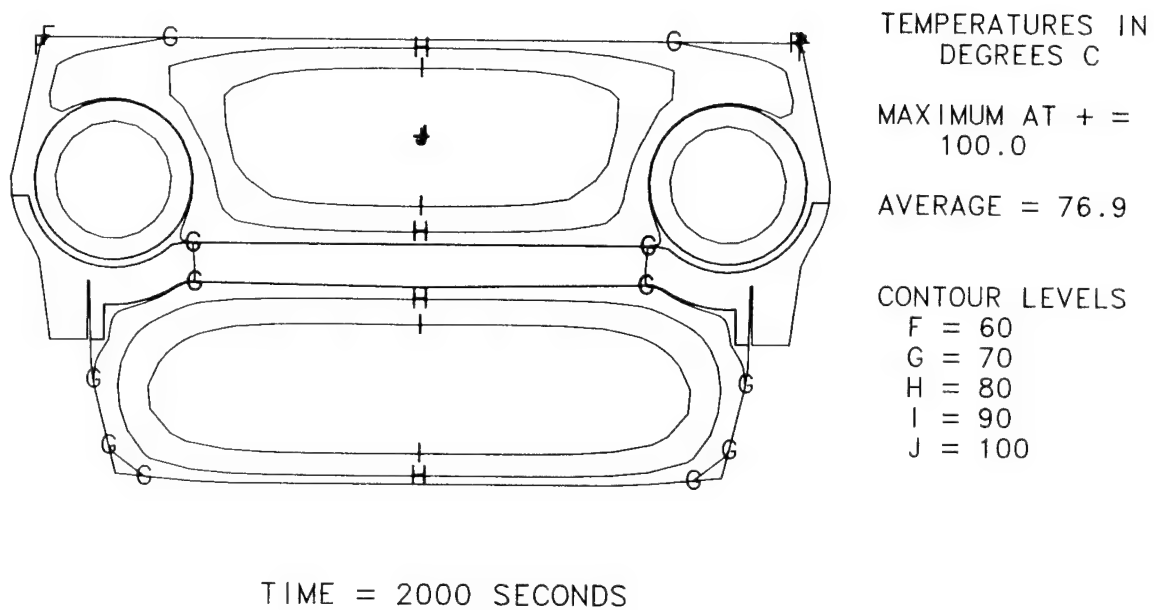


Figure 41 Contours of constant temperature after 2,000 s (0.56 hr.) at
32 km/hr (20 MPH)

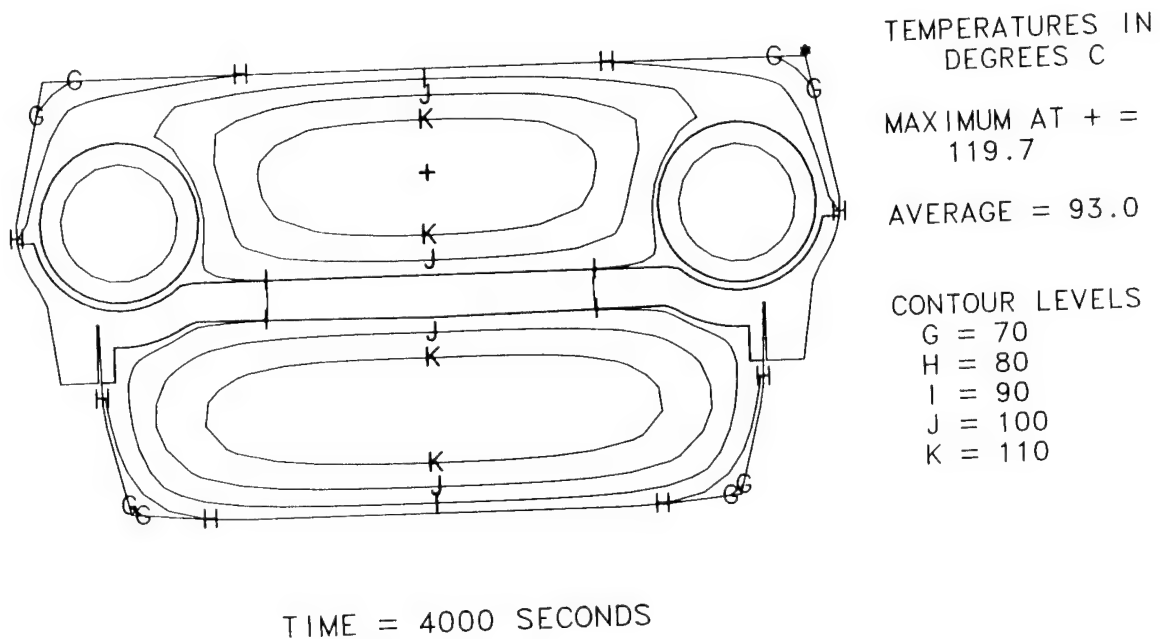


Figure 42 Contours of constant temperature after 4,000 s (1.11 hr.) at
32 km/hr (20 MPH)

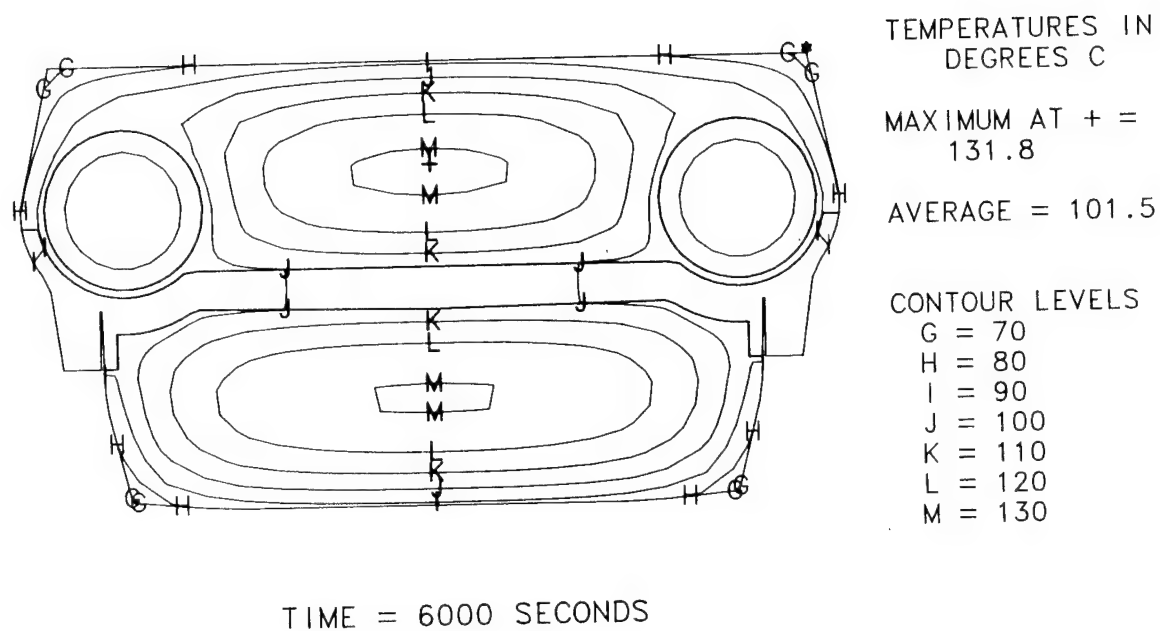


Figure 43 Contours of constant temperature after 6,000 s (1.67 hr.) at 32 km/hr (20 MPH)

after 2,000 s (0.56 hr), 120°C (248°F) after 4,000 s (1.11 hr), and 132°C (270°F) after 6,000 s (1.67 hr). The temperature profiles across the pad between the bottom surface and the steel backing plate are given in Figures 44, 45, and 46. The results show the substantial temperature gradient that is developed across the pad with time. In Figures 47 and 48, we show the temperature-time response for three points within the pad (nodes 10, 37, and 97 -- identified in Figure 49). The curves in Figures 47 and 48 also show the temperature-time response for nodes 406 and 503 within the roadwheel path and node 202 which is within the steel backing plate. Notice that nodes 37, 97, 202, and 406 which are found more to the interior of the assembly show temperature-time curves which are still rising after 6,000 s (1.67 hr). Thus, with additional running time, one can expect higher maximum temperatures at the center of the pad.

The thermal model presented above does a good job of simulating the temperature-time data derived in the field. Improvement of the model can be obtained by recognizing that the heat transfer coefficient can vary with temperature (and thus time). As a first approximation to this problem, the coefficient was assumed to increase in a linear manner from 0 at zero time to 17 W/m²°C (3.0 Btu/hr ft²°F) at 2,000 s (0.56 hr) and 17 W/m²°C for all subsequent time. The TACO code was applied to the thermal model using this variable h. The surface temperature obtained is shown in Figure 50 and is compared to results obtained with a constant h. Notice that the temperature obtained with a constant value of h appears to agree with measured temperatures at later times but is somewhat low at early times. The surface temperature-time behavior for variable h shows good agreement for all times.

3-2b. Structural Response

3-2b(1). Analysis: The structural model completed in FY 80 represented a significant refinement over the preliminary model completed in FY 79. The influence of the roadwheel transmitting the weight of the tank to the roadwheel path has been incorporated into the analysis. The finite element mesh

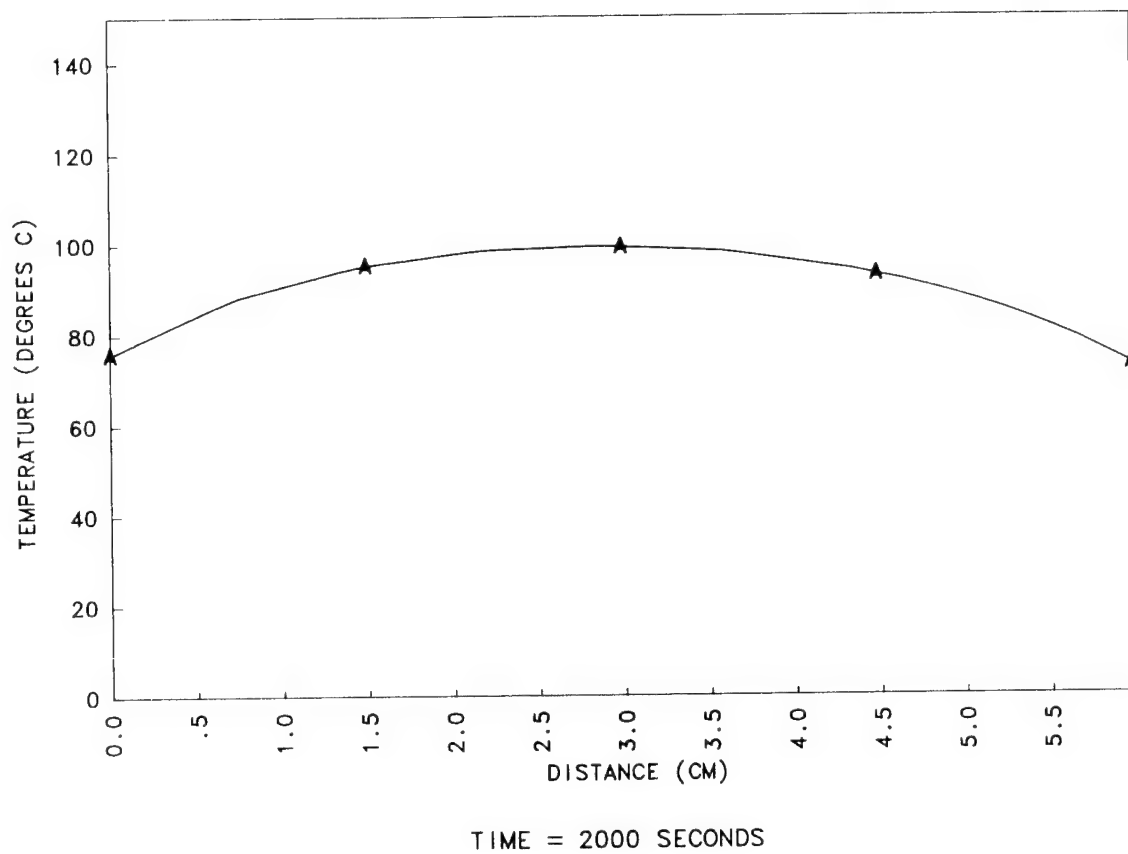


Figure 44 Temperature profile across the pad from the bottom of the pad to the steel backing plate. Profile is for pad after 2,000 s (0.56 hr.) at 32 km/hr (20 MPH)

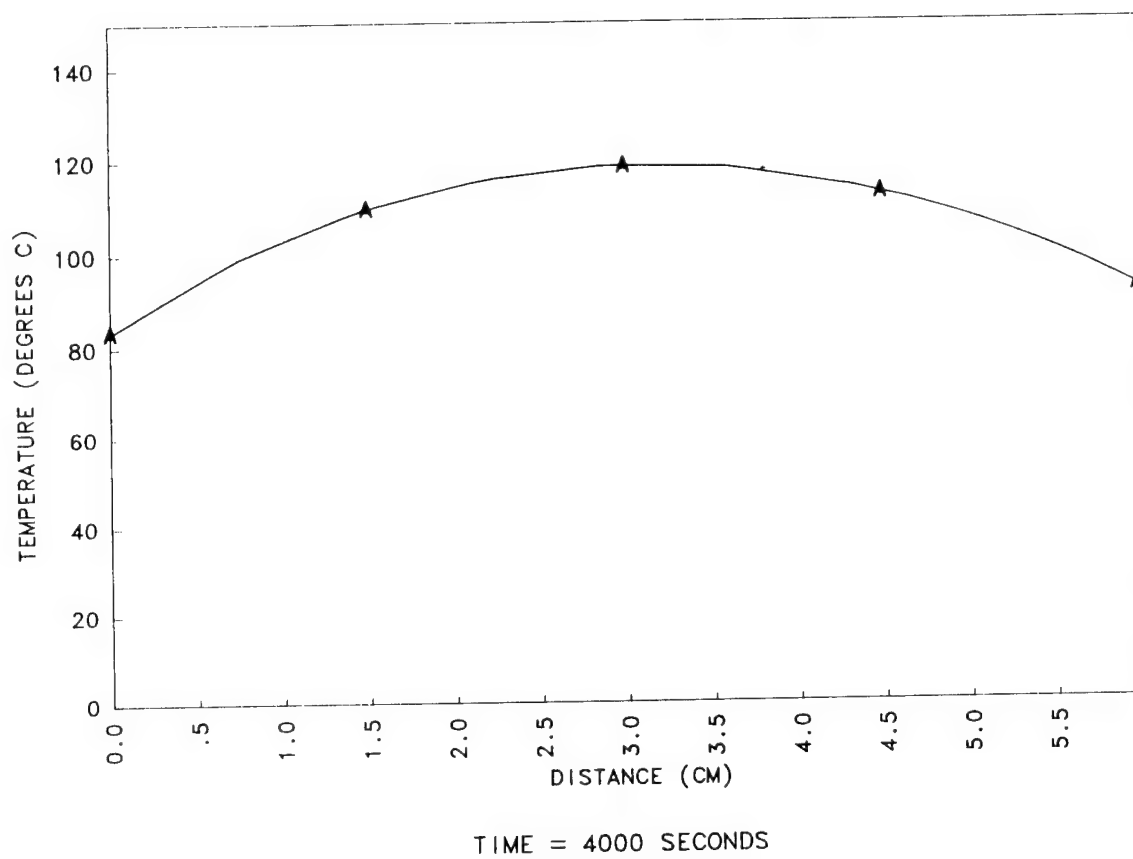


Figure 45 Temperature profile across the pad after 4000 s (1.11 hr).

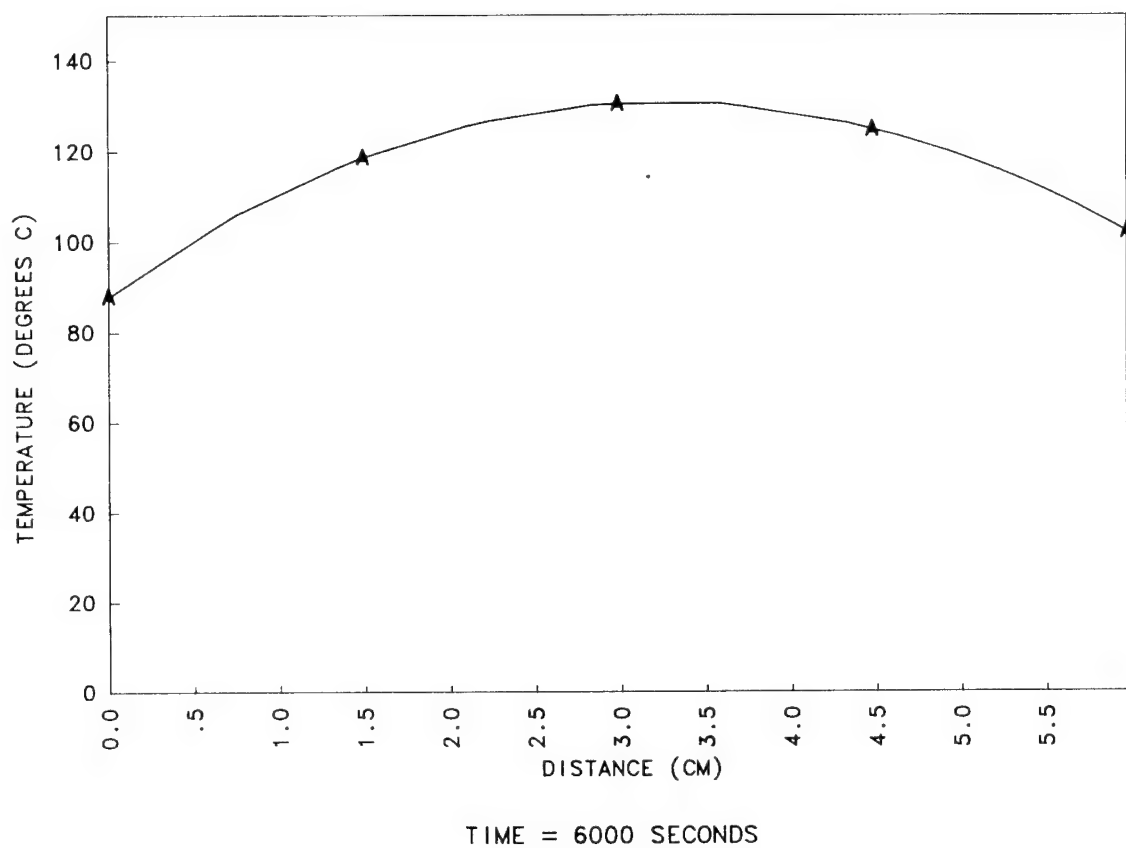


Figure 46 Temperature profile across the pad after 6000 s (1.67 hr).

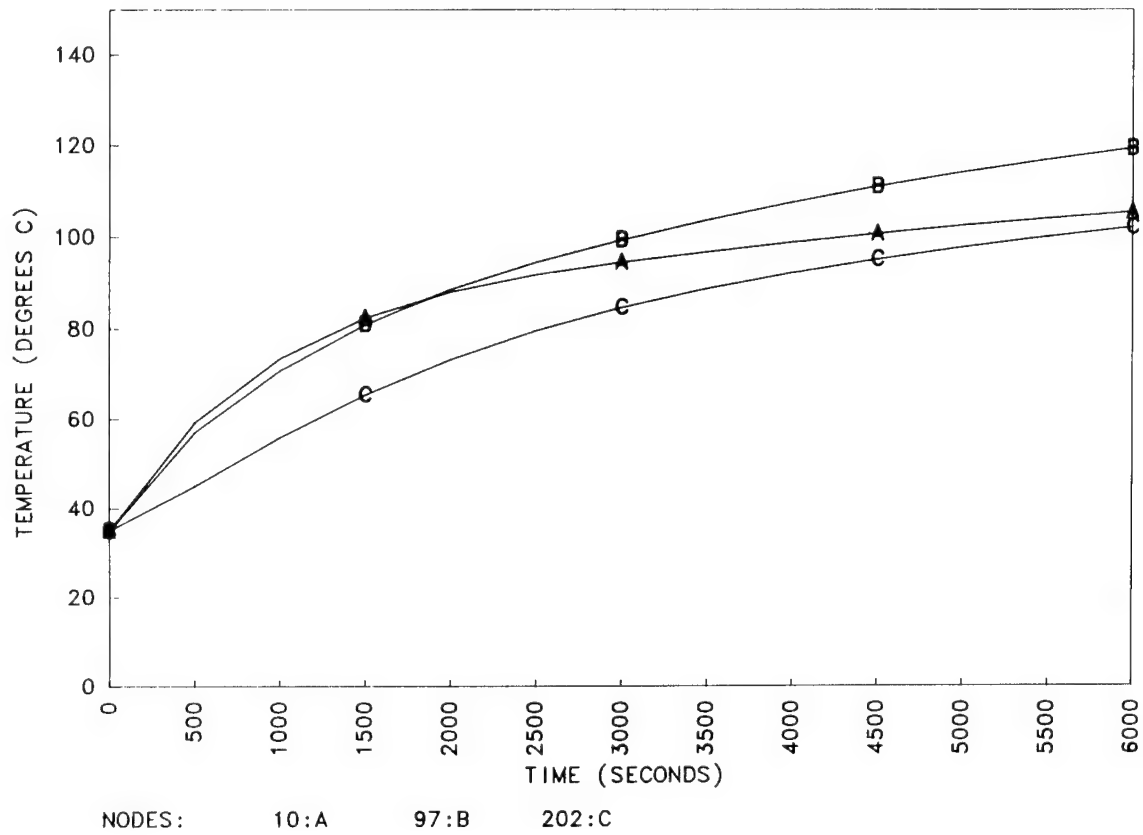


Figure 47 Temperature-time response for nodes 10, 97, and 202. Nodes are identified in Figure 49.

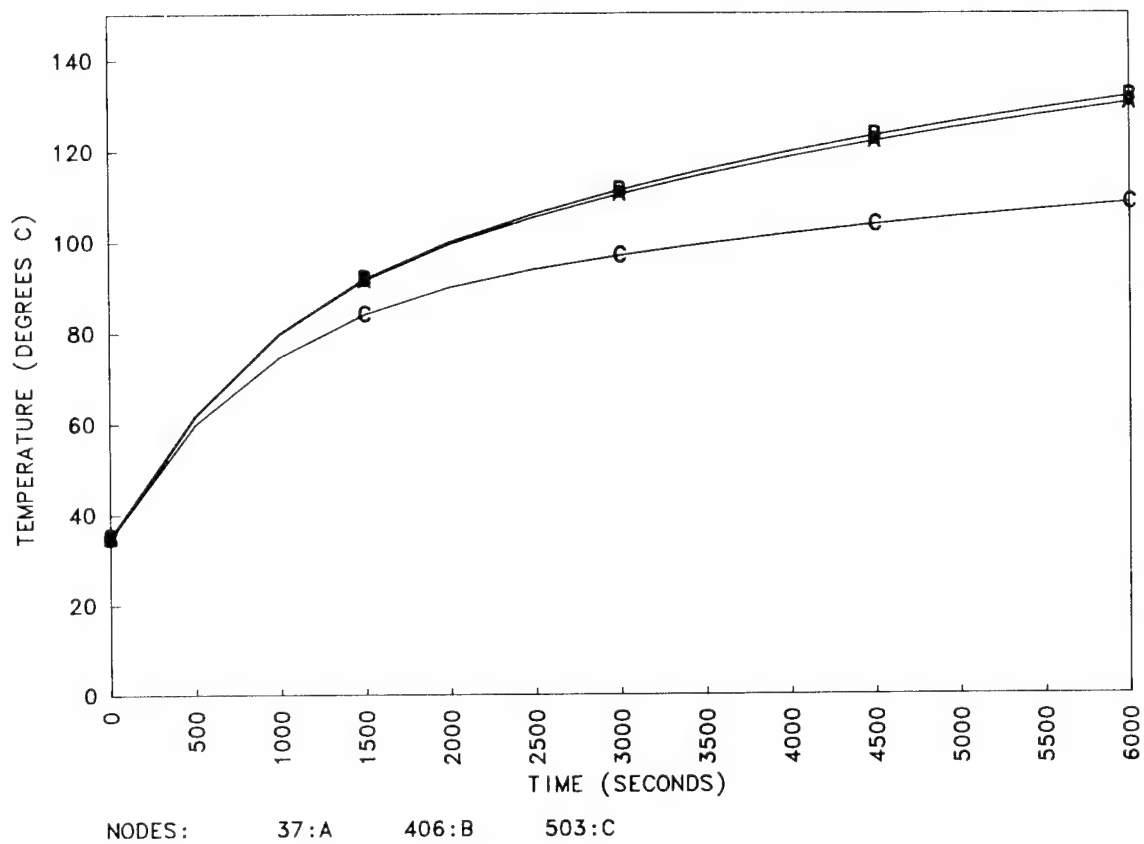


Figure 48 Temperature-time response for nodes 37, 406, and 503. Nodes are identified in Figure 49.

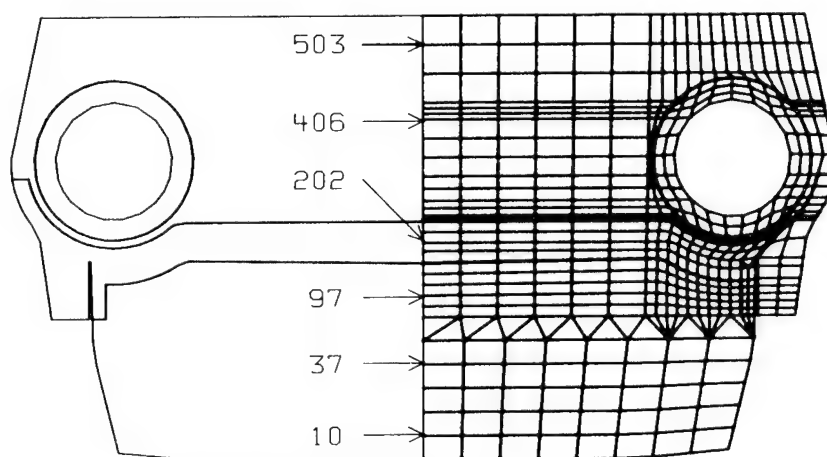


Figure 49 Location of nodes whose temperature-time response is shown in Figures 47 and 48.

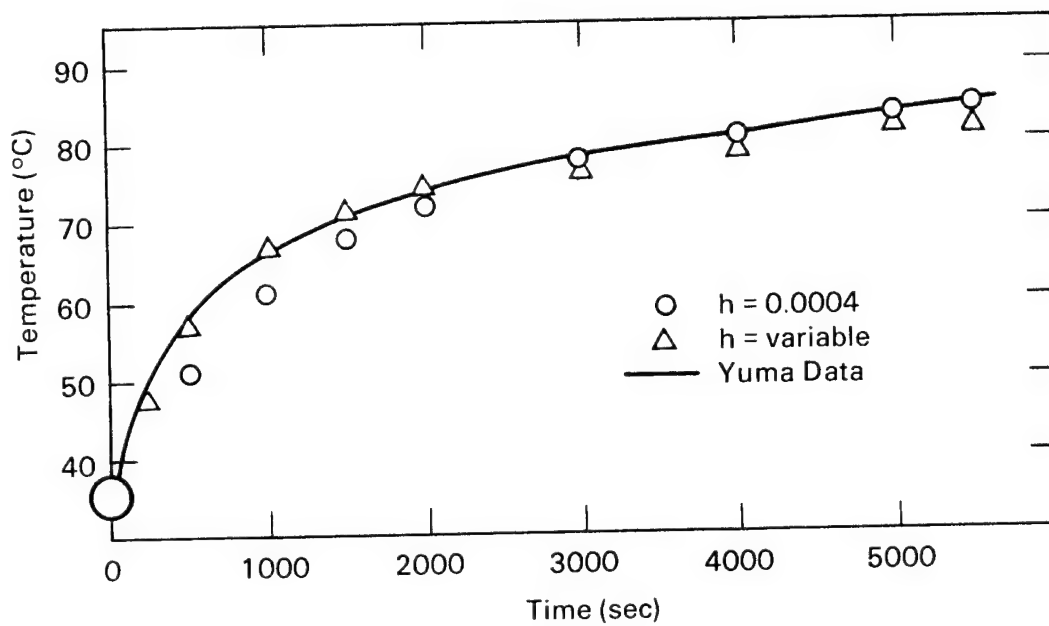


Figure 50 Temperature-time response for the surface of the pad assuming constant and variable heat transfer coefficients (h). Results are compared with actual field data.

used in this analysis is shown in Figure 51. The problem was solved in plane strain. Thus any strains out of the z-y plane shown in Figure 51 are zero -- i.e., $\epsilon_{xx} = \epsilon_{xy} = \epsilon_{xz} = 0$. Obviously, a problem with such complex geometrical and loading characteristics will have three dimensional strains. However, relative to the tank track shoe much more deformation was expected in the section taken than in other possible sections -- xy or xz.

The materials incorporated into this analysis are delineated in Figure 52. The elastic material model available in NIKE2D was used for steel components with a Young's modulus of 2.07 GPa (30×10^6 psi) and a Poisson's ratio of 0.33. The mechanical response of the rubber components was represented by the linear viscoelastic model available in NIKE2D. The density and bulk modulus used here were given earlier in the report. The relaxation modulus in shear was determined from Equation No. 1. As mentioned in Section 2-2, the parameters in this equation can be evaluated from the storage and loss modulus in shear and $\tan \delta$. However, this procedure involves solving algebraically complex equations. A much more direct method is illustrated in Figure 53, which shows a typical load-displacement loop for a viscoelastic material. The short-time and long-time shear moduli can be obtained from the tangent moduli shown in Figure 53. The decay constant can be adjusted to give the correct shape of the loop. Following this procedure, the data in Figure 34 was analyzed to give the shear relaxation modulus parameters shown in Table 12.

The loading conditions for this analysis are shown in Figure 51. The pad has been assumed to be on a rigid flat surface -- thus, the bottom surface of the pad was fixed. Realistic track tensions are available from a previous study of track dynamics.³ This study showed that the track tension depends on a number of factors, some of the most relevant of which are the track pretension (typically 53.4 kN (12,000 lbs)) and obstacles in the path of the track. As illustrated in Figure 54, the maximum track tension will be experienced between the sprocket and the first roadwheel. This tension in the track will decrease as one moves away from the sprocket towards the idler. For the purpose of this analysis, track tension values at front and rear binoculars, for a section of track under a centrally located roadwheel, were

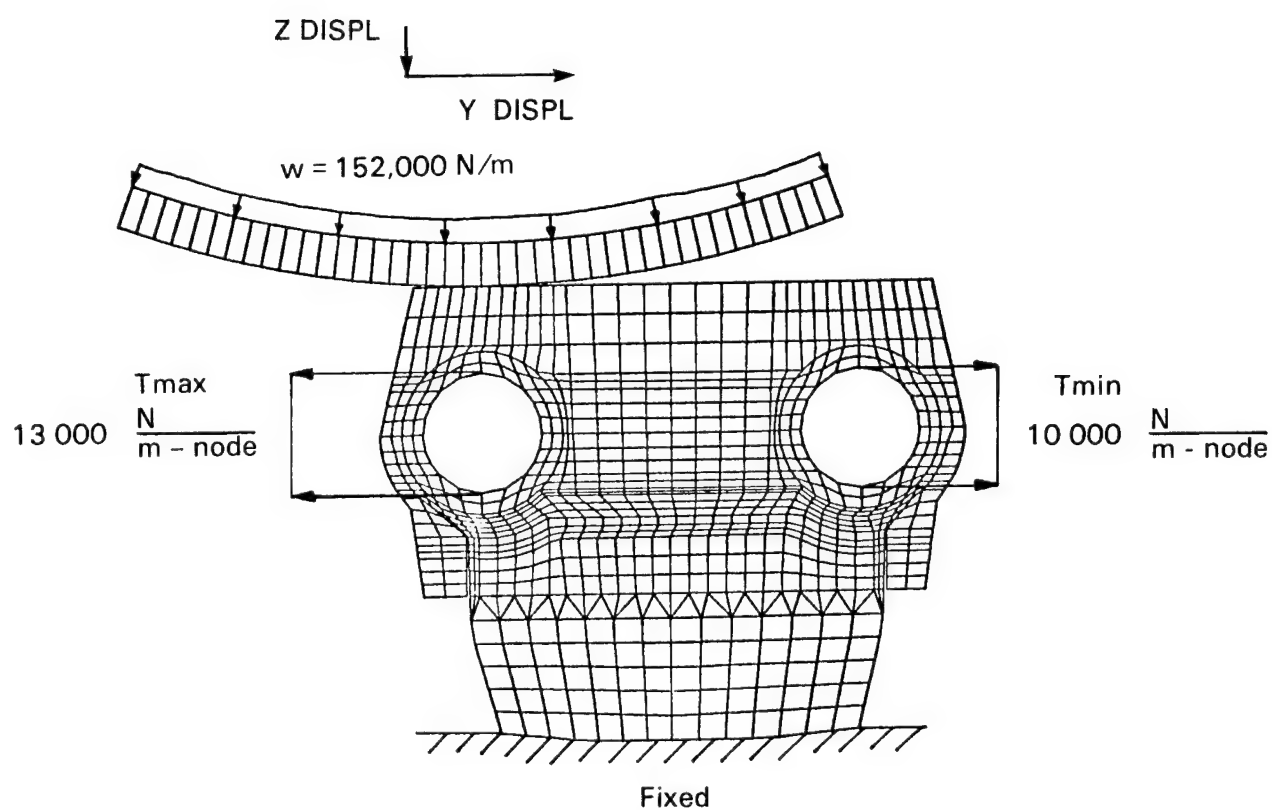


Figure 51 Finite element mesh used in the FY 80 mechanical model. The influence of the roadwheel has been incorporated into the analysis. Loading conditions are shown in the figure.

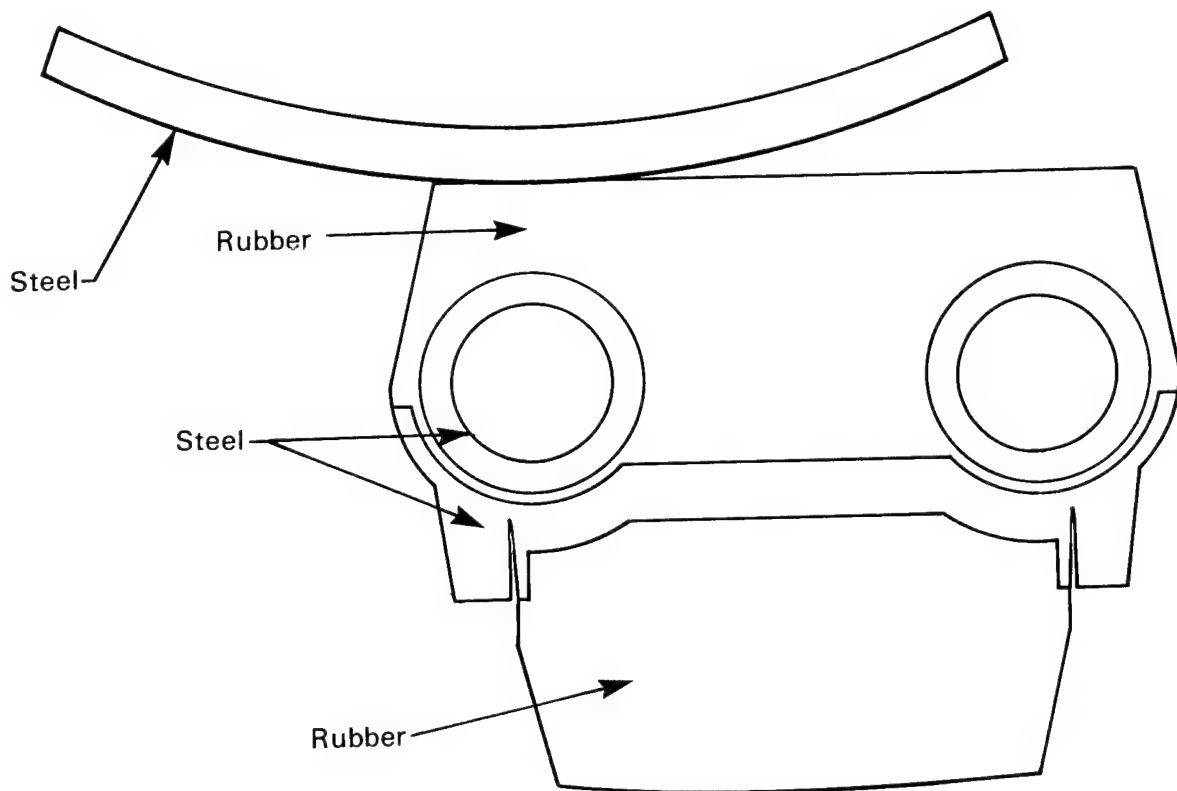


Figure 52 Outline of the finite element mesh shown in Figure 43 showing the materials used in the analysis.

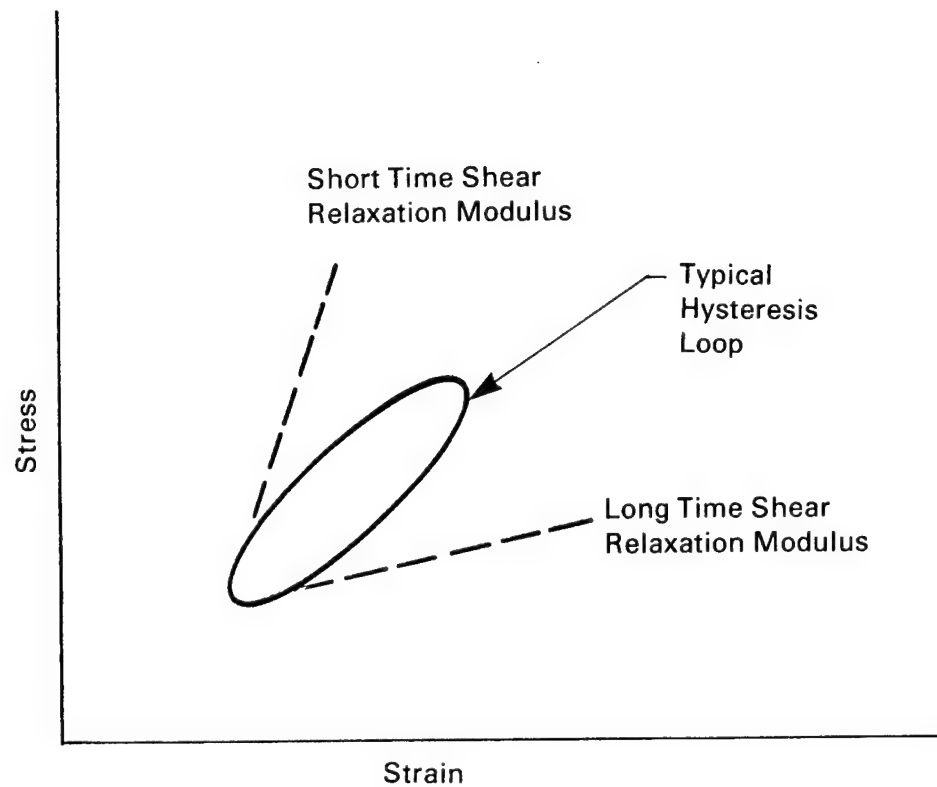


Figure 53 Typical stress-strain loop for a viscoelastic material showing the short-time and long-time shear relaxation moduli.

TABLE 12

SHEAR RELAXATION MODULUS PARAMETERS

<u>Parameter</u>	<u>Value</u>
Short-time Shear Relaxation Modulus	4.14 MPa
Long-time Shear Relaxation Modulus	2.76 MPa
Decay Constant	0.25

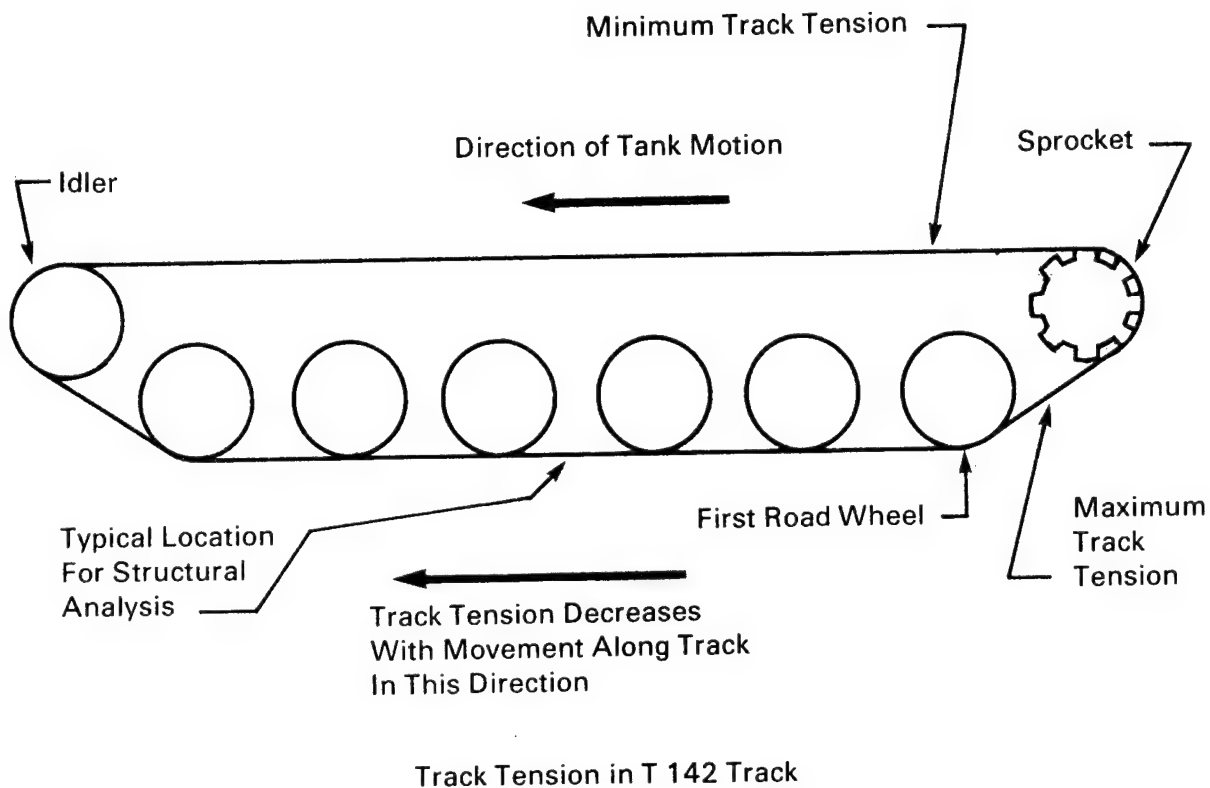


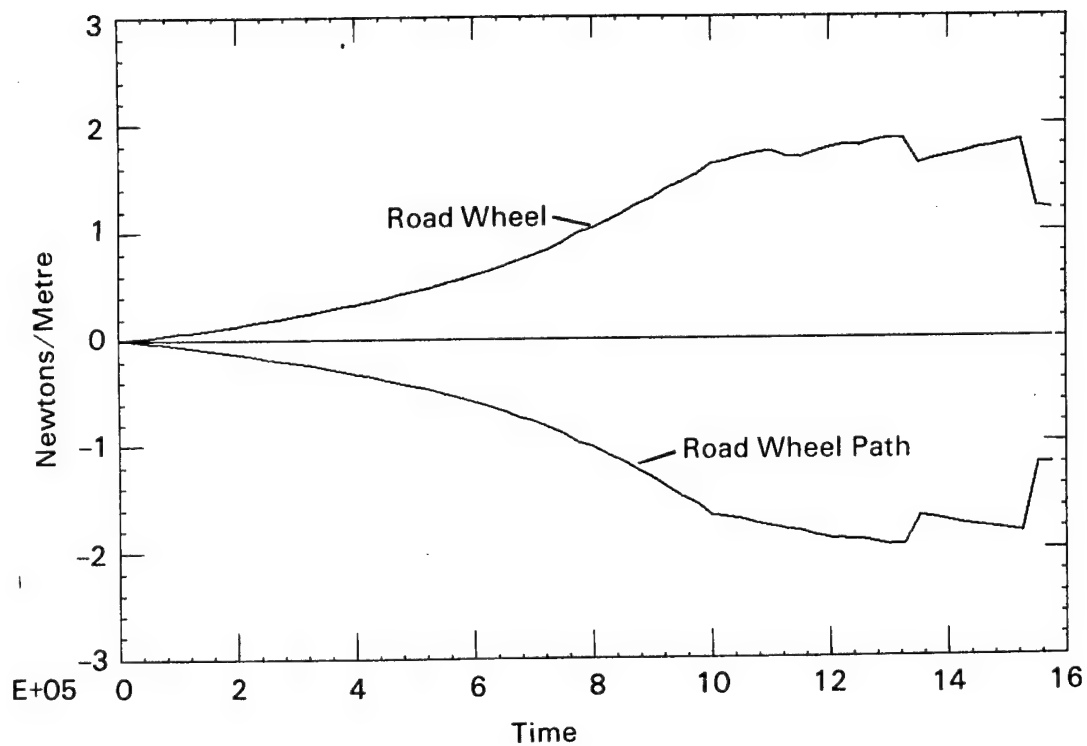
Figure 54 Schematic diagram of the track on the M60 tank showing variation in tension along the track.

taken as 40.0 kN (9,000 lbs) and 30.7 kN (6,900 lbs), respectively. These values represent reasonable estimates for constant velocity operation over flat surfaces. These tensions were calculated per unit depth of track and distributed over eleven nodes each, as shown in Figure 51.

The weight of the tank (taken as 489 kN (110,000 lbs)) was assumed to be uniformly distributed between 24 roadwheels and applied uniformly to the roadwheel as shown in Figure 51. The roadwheel would be displaced downward until the weight of the tank was supported. The roadwheel could then be displaced horizontally across the roadwheel path; thus, simulating motion of the roadwheel over a section of track. This methodology was applied. The interfacial pressure between the roadwheel and the roadwheel path is shown in Figure 55. The pressure increases until the weight of the tank is supported. This occurs at step 10. Computation difficulties were encountered when the roadwheel was displaced horizontally (time steps greater than 10). The solution is well behaved out to step 12.

3-2b(2). Results: The displaced geometry for the shoe and the section of track analyzed are shown in Figure 56. Notice that the tank track pad has undergone significant amounts of distortion. Contours of the normal stress σ_{zz} and the effective stress are presented in Figures 57 and 58, respectively. All stress values are in megapascals. Notice that the largest compressive stress (11.9 MPa) (1,730 psi) is found in the lower left corner of the shoe and is designated by an "N." However this stress is highly localized. A more reasonable estimate of the stress levels found over any significant volume of material can be taken as the P contour level shown (2.5 MPa) (360 psi). The effective stress also reaches a maximum (3.6 MPa) (520 psi) in the lower left corner of the shoe. Contour "E" shown in Figure 58 represents an equivalent stress level of 2 MPa (290 psi).

There are several important observations to be made in these two figures. The first is that the highest compressive stresses are found in the tank track pad. The second observation is that the stresses are quite low relative to stresses that one might expect for fracture. The reason for this is that the shoe is supported over its entire bottom section. This, in effect, simulates



•The dual plot shows that equilibrium has been achieved out to step 12

Figure 55 Interfacial pressure between the roadwheel and the roadwheel path generated as the roadwheel is displaced downward.

Magnification Factor = 1.E+00

Time = 1.00E+01

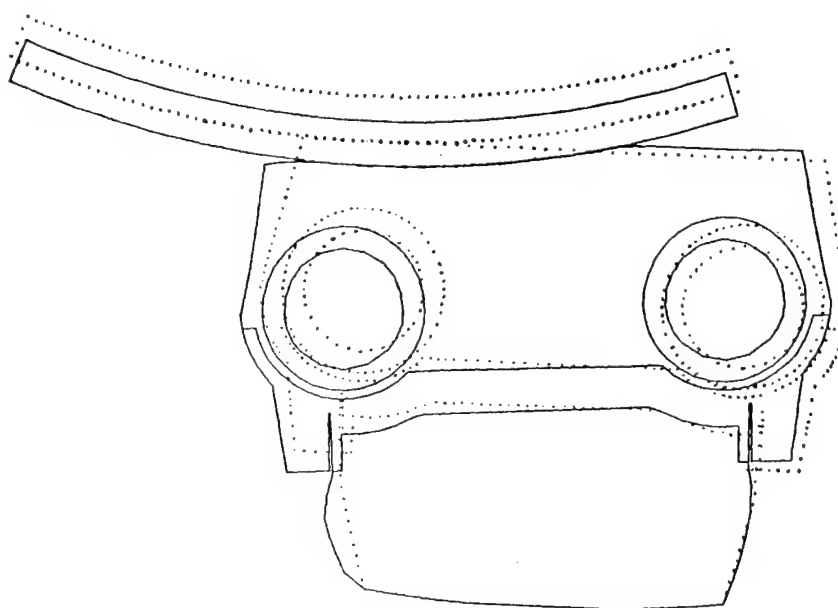


Figure 56 Deformation produced in the tank track shoe and related track components due to the full applied load of the roadwheel.

Time=1.00E+01
 Min(N)=1.19E+07 Pa
 Max(X)=6.85E+06 Pa

Contours of σ_{zz}

Contour Levels (MPa)

O = -3.0
 P = -2.5
 Q = -2.0
 R = -1.5
 S = -1.0
 T = -0.5
 U = 0.0

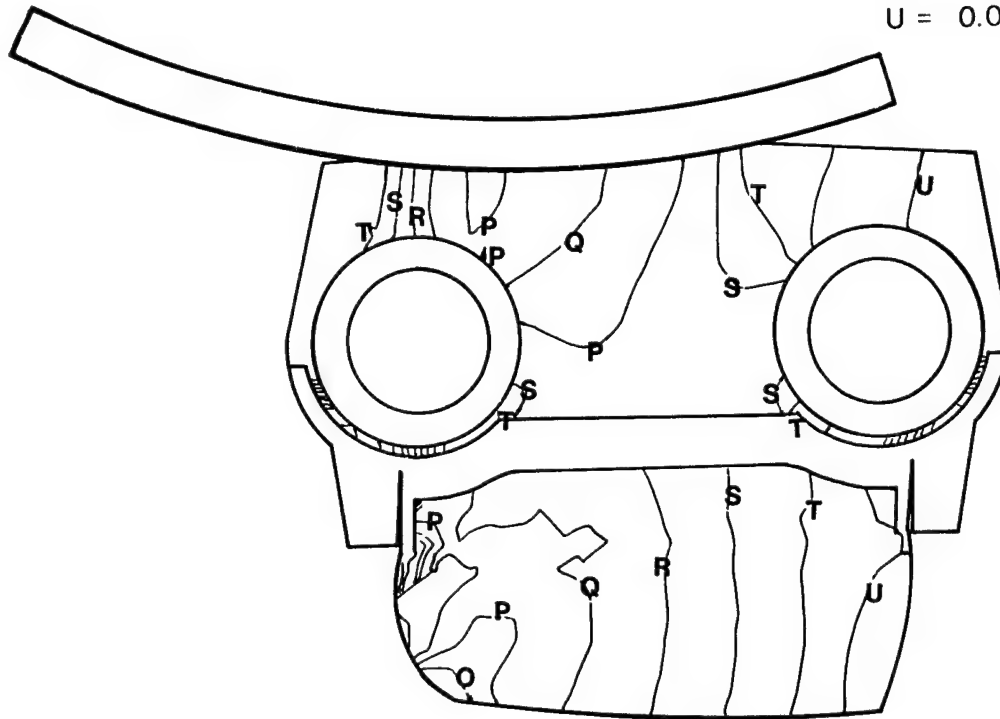


Figure 57 Contours of constant normal stress σ_{zz} produced in the tank track shoe and roadwheel path due to the full applied load of the roadwheel.

Time=1.00E+01
Min(N)=1.94E+04 Pa
Max(X)=3.61E+06 Pa

Contours of Effective Stress

Contour Levels (MPa)

A = 0.0
B = 0.5
C = 1.0
D = 1.5
E = 2.0

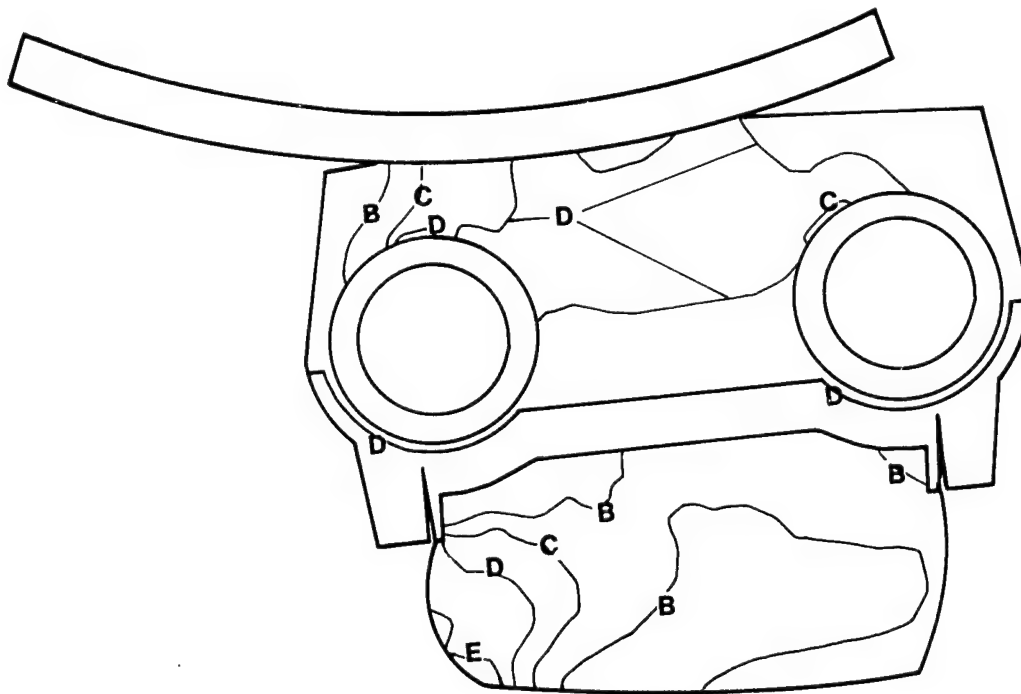


Figure 58 Contours of constant effective stress produced in the tank track shoe and roadwheel path due to the full applied load of the roadwheel.

tank operation on a paved surface. Realistic estimates of stress levels and deformation produced in cross-country operations can be obtained by placing the pad in contact with surfaces having sharp projections and non-smooth surfaces.

3.3. Experimental Work

3-3a. Chemical Characterization: Results reported in this section and the next section were done in coordination with tests done at the Yuma Proving Grounds. These field tests were run under the guidance of TARADCOM. The tests consist of running a tank with T-142 track on one of three test courses established at Yuma. The testing was done using an M48 A5 tank. Tank track shoes from the four different manufacturers were mounted on the track. The performance of these shoes was then assessed as a function of mileage. The three courses were a paved course, a gravel course and a cross-country course. During a field trip to Yuma, the following observations were made:

3-3a(1). The paved course was just under 8 km (5 miles) in length. It consisted of one long traight track segment with loops on either end:



While the condition of the track was good, the surface was somewhat rougher than a typical street. Approximately 6.4 km (4 miles) of gravel road (2 coming, 2 going) were traveled each day to get to and from the paved track.

3-3a(2). The gravel and rough terrain courses were similar in that the road surface was hard packed dirt with loose top. Gravel was on the order of 3.2 mm to 19 mm (1/8 in. to 3/4 in.) in diameter. The courses differed in that the gravel course was level; whereas, the rough course was cross country and therefore very hilly. As a point of reference, a 4-wheel drive pick-up was capable of driving rough terrain without excessive difficulty.

Chemical characterization has been completed on virgin SBR from the four tank track shoe manufacturers. The objective here is to delineate significant chemical differences between pads from various manufacturers. These differences may then provide a basis for understanding differences in observed performance.

Elemental analyses of the tread for both nonmetals and metals has been achieved. The elemental analysis for nonmetals are given in Table 13. The elemental analysis of trace metals was based on flame ionization spectroscopy, and the results are given in Table 14. Interesting differences include the presence of Ba, Pb, and Cd in the pad from Vender A; high concentrations of Ni, V, and Cu in the pad from Vender B; and significant amounts of Sb in the pad from Vender D.

Extraction studies were also carried out to evaluate the percent extractables, percent styrene, and the average molecular weight between crosslinks. The extraction studies were carried out in accordance with ASTM D 297, Section 17.3. UV spectroscopy was used to evaluate the percentage of bound styrene in accordance with Section 56 of the above ASTM specification. The average molecular weight between crosslinks was evaluated using swelling measurements performed in chloroform according to a simple extension of the Flory-Rehner Equation:

$$M_x = -\rho_2 V_1 \left(\phi_2^{1/3} - 2\phi_2/f \right) / \left[\ln (1 - \phi_2) + \phi_2 + \chi_1 \phi_2^2 \right] \quad (8)$$

where M_x , is the average molecular weight between crosslinks, ρ_2 is the polymer density (0.91 Mg/m³) (62.43 lb/ft³), ϕ_2 is the volume fraction of polymer, f is the functionality of the crosslink (4), V_1 is the molar volume of solvent, and χ_1 is the polymer-solvent interaction parameter (0.433). Table 15 lists the results of these measurements.

TABLE 13

CONCENTRATION OF NONMETALS AS PERCENT BY WEIGHT

	% N	% C	% H	% S
VENDER A	0.34	85.9	6.33	1.8
VENDER B	0.43	85.2	6.77	1.9
VENDER C	0.29	87.9	6.72	1.7
VENDER D	0.42	83.7	7.08	1.9

TABLE 14

CONCENTRATION OF METALS (AS PPM) IN NEW TANK TREAD RUBBERS
FROM DIFFERENT MANUFACTURERS

Element	Vender A	Vender B	Vender C	Vender D
Zn	20,000	25,000	20,000	40,000
Ca	150	100	600	200
Si	1000	1500	400	6000
Fe	125	80	300	100
Al	1000	1500	150	400
Mg	125	400	150	100
Ti	100	100	20	40
Ba	25	1	8	ND
Ni	15	300	8	4
Mn	9	2	5	2
V	3	25	5	ND
Cr	15	4	3	2
Cu	3	15	3	6
Pb	25	4	3	4
Sr	2.5	2	3	1
B	1.5	0.8	2	0.6
Sb	ND	ND	ND	60
Mo	1.0	0.8	0.5	ND
Ag	0.3	0.4	0.3	0.6
Cd	6	ND	ND	ND
Sn	ND	1	ND	ND
Co	ND	1	ND	ND

ND - indicates that none of this metal was detected.

TABLE 15

EXTRACTABLES, STYRENE CONTENT IN SBR'S AND MOLECULAR WEIGHTS BETWEEN
CROSSLINKS IN NEW TANK TREAD RUBBERS FROM VARIOUS MANUFACTURERS

	Vender A	Vender B	Vender C	Vender D
% Extractable	12.4 \pm 0.9	15.9 \pm 0.2	13.7 \pm 0.2	15.0 \pm 2.0
% Styrene	17.22	21.75	24.69	21.00
M $\times 10^3$	4.60	4.63	3.31	3.47
(1/2 M) $\times 10^{-4}$	1.10	1.08	1.51	1.44

The infrared spectra of the pyrolyzates of the various treads were obtained from the residue of small pieces of extracted tread that condensed on the sides of a pyrex test tube heated over a Bunsen burner. The condensate was sandwiched between salt plates and analyzed on a Perkin-Elmer 457 IR spectrometer. The spectra of pyrolyzates from new treads are shown in Figures 59 through 62. Based on this IR spectra, the treads of all vendors were found to be SBR random copolymers. The absorption peak assignments are identified in Table 16.

The additives in the extract were separated by gas chromatography (GC) and identified by mass spectroscopy of each GC peak. Table 17 lists the identities and relative concentrations of each species in the extract.

3-3b. Effect of Terrain on Physical Properties and Chemical Characteristics:

The influence of terrain on the physical properties and chemical characteristics of the tread rubber is to be evaluated from tank track shoes that have been run on one of the three courses described in the last section. Shoes that have been run on the paved course are available for 800 km (500 miles), 1,600 km (1,000 miles), and 2,400 km (1,500 miles) total accumulated distance. Shoes that were run on the gravel or cross-country course have respective 1,600 km (1,000 miles) and 400 km (250 miles) total accumulated distance. The experimental procedure here was to take pads that have been tested on the various courses, remove appropriate samples, and evaluate the properties outlined below.

Chemical characterization employed techniques that would enable us to identify degradation of the shoe rubber under field conditions. The methods being employed are:

- o swelling behavior in chloroform
- o IR of the pyrolyzate
- o gas chromatography and mass spectroscopy

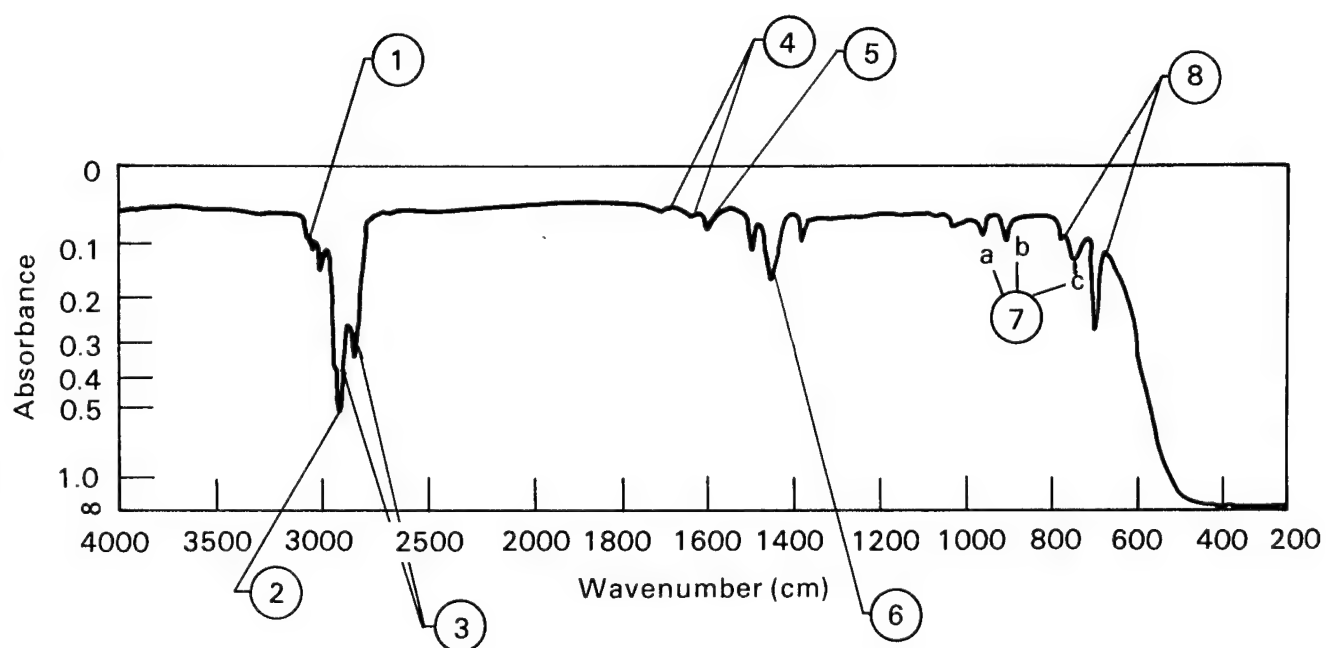


Figure 59 Infrared spectra of the pyrolyzates from new from vender B tread.

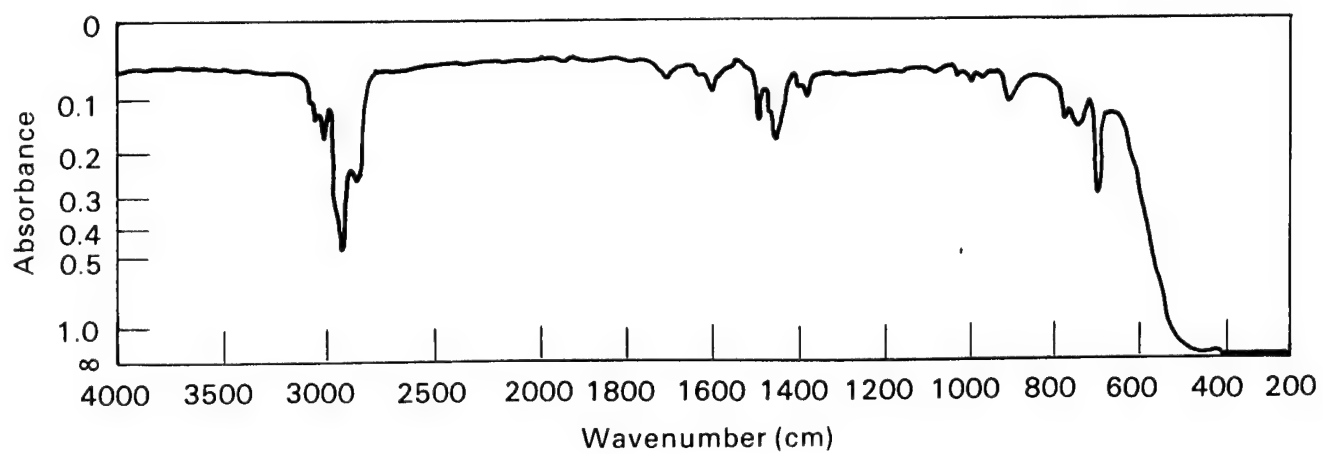


Figure 60 Infrared spectra of the pyrolyzates from new from vender A tread.

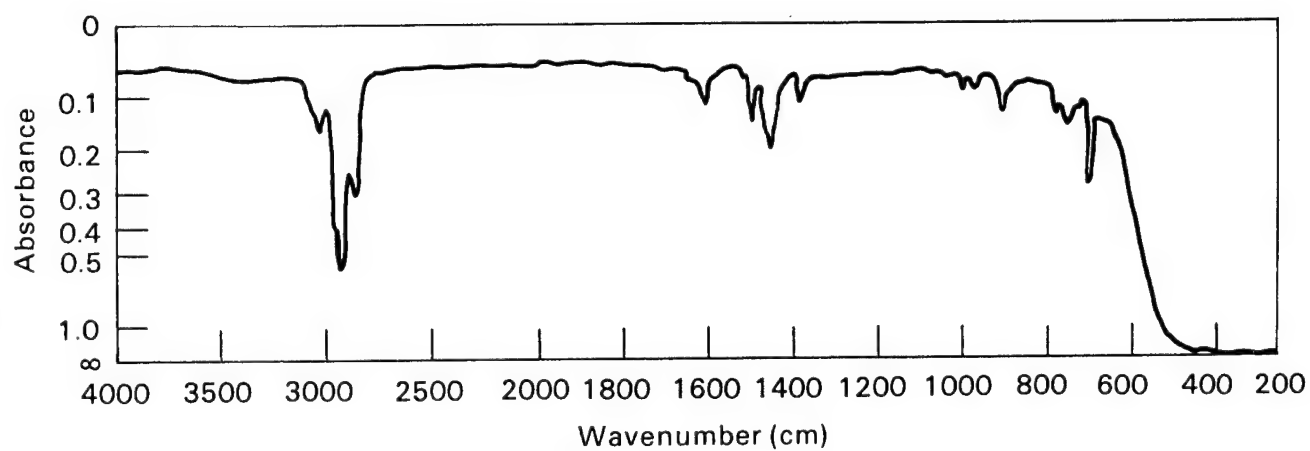


Figure 61 Infrared spectra of the pyrolyzates from new from vender D tread.

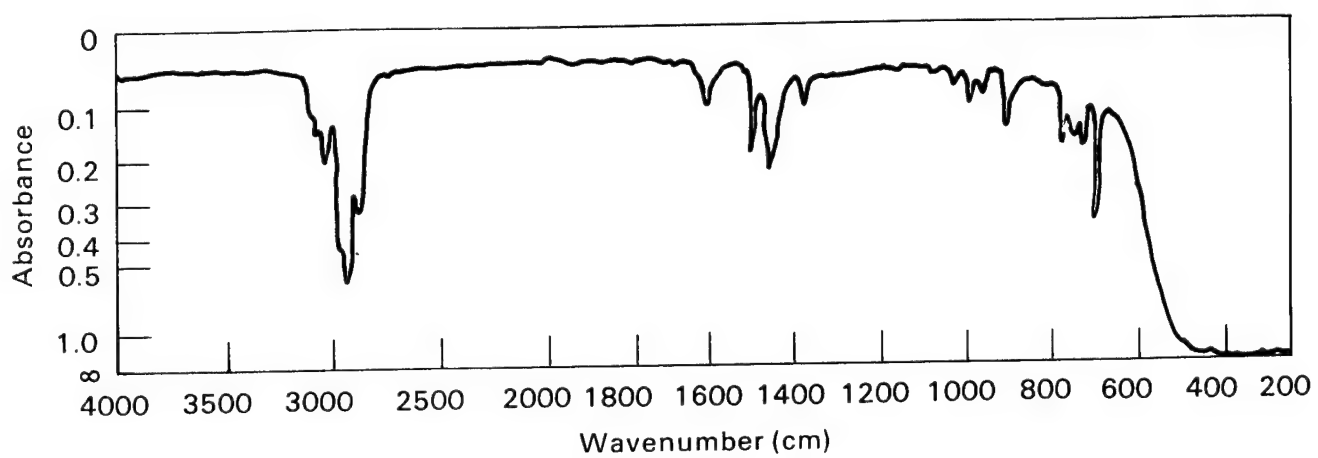


Figure 62 Infrared spectra of the pyrolyzates from new from vender C tread.

TABLE 16

ABSORPTION PEAK ASSIGNMENTS FOR INFRARED SPECTRA
OF PYROLYZATES OF TREADS

1. 3080, 3060, and 3030 cm^{-1} are due to aromatic and vinyl hydrogen stretching vibrations.
2. 2925 and 2860 cm^{-1} doublet is associated with methylene hydrogen asymmetric and symmetric stretching vibrations, respectively.
3. 2960 and 2872 cm^{-1} shoulders are probably due to methyl hydrogen asymmetric and symmetric stretching vibrations, respectively.
4. 1770 and 1640 cm^{-1} are double bond vibrations.
5. 1600 cm^{-1} is an in-plane aromatic skeletal vibration.
6. 1490, 1450, and 1375 cm^{-1} are the result of CH_3 - and $-\text{CH}_2$ - bending vibrations.
7. Absorption peaks below 1000 cm^{-1} are associated with particular geometric isomers, i.e.
 - a. 980-960 cm^{-1} from trans unsaturation
 - b. 910 cm^{-1} from vinyl unsaturation
 - c. 735 cm^{-1} from cis unsaturation.
8. 760 and 700 cm^{-1} arise from monosubstituted phenyl out of plane bending vibrations.

TABLE 17
CONSTITUENTS IN THE CHLOROFORM-ACETONE EXTRACT IDENTIFIED BY GC-MS

Retention Time	Sample ID	Vender			
		A	C	B	D
3.42	toluene				
4.08	tetrachloroethylene	1.16			
4.25	diacetone alcohol	18.14	14.0	25.23	23.28
4.57	Xylenes	1.22		1.49	3.04
4.67					
4.92					
5.95				2.10	
7.62				1.50	
7.75	3-phenyl-4-methyl syndrone		2.05		
7.87		0.83			
9.40	Benzothiazole	3.21	8.00	0.53	1.53
9.73		2.75			
10.55	tripropylamine			1.07	
10.92	tripropylene glycols			1.35	
11.02			1.08		
12.62	2,2,4-trimethyl-1,2- hydroquinoline	8.56	34.87	17.88	23.67
12.75	second quinoline	0.92	8.00	2.63	
13.37	n-pentadione		1.13		1.11
14.70	n-hexadecane - C ₁₆				
14.82	diphenylamine	1.14	13.41	2.73	4.98
15.25	n-methyl diphenylamine			5.27	

TABLE 17 (CONTINUED)

CONSTITUENTS IN THE CHLOROFORM-ACETONE EXTRACT IDENTIFIED BY GC-MS

Retention Time	Sample ID	<u>Vender</u>			
		A	C	B	D
15.32					1.55
15.87	n-pentadecane C ₁₅				3.24
15.97	n-tridecane C ₁₃				2.57
16.22	(3,4'-dimethyl biphenyl)			0.81	
16.32	methyl dibenzothiophene			0.86	
16.43	methyl dibenzothiophene			0.42	
(17.38)	methyl dibenzothiophene	0.34			
16.97	m-Octadiene C ₁₈				2.17
17.10	m-pentacosene				1.29
17.92	2-methyl carbazole		4.77		
18.00	2-anilino-2-phenyl acetonitrile				2.22
18.05	C ₁₉ + 2-anilino-2 phenyl acetonitrile			1.4	
18.10	2-methyl carbazole + methylantracene	2.32			
18.17	C ₂₀ alkane	1.50			
18.78				0.88	
19.93				0.81	
19.03	C ₂₁ alkane			0.74	
19.18	hexamethyl-s-hydrdecene		3.80		
19.95	2-t-butyl-6-phenyl-	7.91		6.68	

TABLE 17 (CONTINUED)
 CONSTITUENTS IN THE CHLOROFORM-ACETONE EXTRACT IDENTIFIED BY GC-MS

Retention Time	Sample ID	<u>Vender</u>			
		A	C	B	D
20.12	C ₂₂ alkane	1.10			
20.28	2,5-hexanedione and n-methoxy succinimide			1.25	
21.88	C ₂₄ alkane	0.68			
21.95	methylcallistate			0.52	4.26
22.73	C ₂₅ alkane	0.79			
22.92	allyl benzoate and phthalate			1.04	
23.53	C ₂₆ alkane	0.69			
24.07			1.78		
24.48	C ₂₇ alkane	0.77			
24.63	2,4-dimethyl-1,8-naphtidene				7.95
24.73				1.51	
24.79				1.11	
25.35				2.56	
25.58	C ₂₈	0.85			
25.77			1.71		
26.80	C ₂₉ hydrocarbon	0.76			7.95
26.94	C ₂₉ hydrocarbon			0.78	
28.63	C ₃₀ hydrocarbon	0.69		1.07	0.91

Baseline data (determined on as-manufactured pads) were reported in the last section.

The physical properties examined include those that influence the temperature buildup or reflect the residual mechanical properties of the pads. The following properties are being examined:

- o density
- o thermal diffusivity
- o heat capacity
- o tear strength
- o storage modulus, loss modulus and $\tan \delta$.

Evaluation of the density, thermal diffusivity and tear strength for shoes tested in various terrains were completed in FY 80. The other data is in progress.

The density data is reported in Table 18. No significant differences exist between data for as-manufactured pads and data for pads used in the various courses.

The thermal diffusivity data are shown in Table 19. The accumulated mileage has had a rather pronounced effect on the thermal diffusivity. Using the data from Vender A as a basis for comparison, the accumulated mileage has decreased the thermal diffusivity by 24% for the 2,400 km (1,500 mile) paved road test and 16% for the cross-country test. The thermal diffusivity for pads used on the gravel course is unchanged. The magnitudes of these changes are not firmly established due to limited data. However, the trend is clearly established. Decreasing the thermal diffusivity would result in higher temperatures at the center of the pad during hysteretic heat generation.

TABLE 18

EFFECT OF FIELD TESTING ON DENSITY OF TANK TREAD SBR

Test Course	Vender	Sample Number	Density Mg/m ³	Temp (°C)
As Manufactured	A	1	1.186	21.2
	A	2	1.184	21.2
	A	3	1.186	21.2
	A	4	1.192	20.1
	A	5	1.190	20.1
	A	6	1.192	20.1
	A	7	1.191	20.1
	A	8	1.190	20.1
	B	1	1.587	22.4
	B	2	1.594	22.4
1500 Miles Paved	A	1	1.179	21.8
	A	2	1.179	21.8
	A	3	1.181	21.8
	B	1	1.158	21.8
	B	2	1.159	21.8
	B	3	1.160	21.9
1000 Miles Gravel	A	1	1.185	22.4
	B	1	1.160	21.6
250 Miles Cross Country	A	1	1.187	21.4
	B	1	1.162	22.4

TABLE 19
EFFECT OF FIELD TESTING ON THE THERMAL DIFFUSIVITY
OF TANK TREAD SBR

Test Course	Vender	Sample Number	Thermal Diffusivity mm ² /s
As Manufactured	A	1	2.19×10^{-1}
	A	2	2.01×10^{-1}
1500 miles paved	A	1 (run 1)	1.61×10^{-1}
	A	1 (run 2)	1.60×10^{-1}
	B	1 (run 1)	1.62×10^{-1}
	B	1 (run 2)	1.65×10^{-1}
1000 miles	A	1	2.15×10^{-1}
Gravel Course	B	1	1.76×10^{-1}
250 miles	A	1	1.85×10^{-1}
Cross-Country	B	1	1.58×10^{-1}

The tear strength was evaluated at room temperature and 204°C (400°F). Results are given in Tables 20 and 21. The tear strength at 204°C is higher for the pads from Vender A than Vender B. Also, the pads from Vender A appear to have experienced a small increase in tear strength over that for the as-manufactured pads for all three courses. However, the increase here is small, and data at this point is somewhat limited. The data taken at room temperature is more revealing. Pads tested for 2,400 km (1,500 miles) paved and on the cross-country course show a significant decrease in tear strength. Using the data on pads from Vender A as a basis for comparison, the decrease amounts to almost 30% for pads tested on the cross-country course and 20% for pads tested for 2,400 km (1,500 miles) paved. The tear strength of pads from Vender A tested on the gravel course shows a much smaller decrease. There is also a significant difference in the gravel course data obtained on pads from Venders A and B. Thus, there appears to be significant amounts of damage that can be introduced into pads by their service history. This damage probably makes the pads more susceptible to cutting and chunking in the field. The origin of this damage and whether it is chemical or mechanical in nature is important to understand. Knowledge here could be used to improve the life of tank track pads.

TABLE 20

TEAR RESISTANCE OF FIELD TESTED PADS
 TESTING TEMPERATURE = 22°C

Terrain	Vender and Pad Identification	Specimen Number	Tear Resistance N/mm
1500 miles paved	Vender A Pad 19	1	43.3
		2	38.5
		3	37.5
	Vender B Pad 20	1	35.9
		2	38.4
		3	44.5
1000 miles gravel	Vender A	1	43.8
		2	46.4
		3	42.9
		4	55.1
	Vender B Pad 54	1	32.8
		2	40.9
		3	38.1
		4	35.2
250 miles cross country	Vender A Pad 51	1	38.0
		2	36.1
		3	34.8
	Vender B Pad 44	1	34.6
		2	37.7
		3	31.9
		4	32.1

Average tear resistance of as-manufactured pad
 from Vender A = 49.9 N/mm.

TABLE 21

TEAR RESISTANCE OF FIELD TESTED PADS
 TESTING TEMPERATURE = 204°C

Terrain	Vender and Pad Identification	Specimen Number	Tear Resistance N/mm
1500 miles paved	Vender A	<u>4</u>	16.6
	Pad 19	5	15.0
	Vender B	4	11.6
	Pad 20	5	11.0
1000 miles gravel	Vender A	5	16.7
		6	18.8
	Vender B	5	11.6
	Pad 65	6	15.0
250 miles cross country	Vender A	4	18.2
	Pad 51	5	19.8
	Vender B	5	12.9
	Pad 44		

Average tear resistance of as-manufactured pad
 from Vender A = 13.7 N/mm

REFERENCES

1. Batelle Columbus Division, Second Quarterly Report for Tank Dynamics Program, CLIN 0002 TASK No. 77-1 (from the Advanced Concepts Laboratory--Contract Number DAAE 07-76-C-0165, June 24, 1977) p. 36.
2. I. M. Ward, Mechanical Properties of Solid Polymers, Wiley-Interscience, London, 1971, p. 97.
3. Batelle Columbus Division, Sixth Quarterly Technical Report on the Track Dynamics Program, CLIN 0002 Task No. 77-1 (from the Advanced Concepts Laboratory--Contract Number DAAE 07-76-C-0165, July 28, 1978).

APPENDIX A

EXPERIMENTAL METHODS

A-1. Density: The density of SBR was evaluated using a hydrostatic weighing technique in which a sample of pad is weighed in air and then again in a water bath. The density of the sample can then be determined from the expression

$$\rho_s = \frac{W_a \rho_w}{(W_a - W_w)} \quad (A1)$$

where

ρ_s = sample density
 W_a = sample weight in air
 W_w = sample weight in water
 ρ_w = water density

A-2. Thermal Diffusivity by Flash Laser Method: A thin disc of SBR has a foil thermocouple mounted on one side of the sample. The other side of the sample receives a flash laser beam pulse that deposits about 2 J of energy into the surface of the sample. The experimental arrangement is shown in Figure A.1. From the temperature-time record and the thickness of the disc the thermal diffusivity can be calculated.

A-3. Thermal Conductivity Using Unguarded Hot Plate Method: In this method two SBR discs 4 inches in diameter and 1/4 inches thick were placed on opposite sides of a heater. The outer sides of the SBR discs were then placed between cold plates. The experimental arrangement is shown in Figure A.2. Two thermocouples were placed between each specimen surface and hot and cold temperatures of the sample were recorded. The amount of power supplied to the heater was monitored. The thermal conductivity was determined from the following expression:

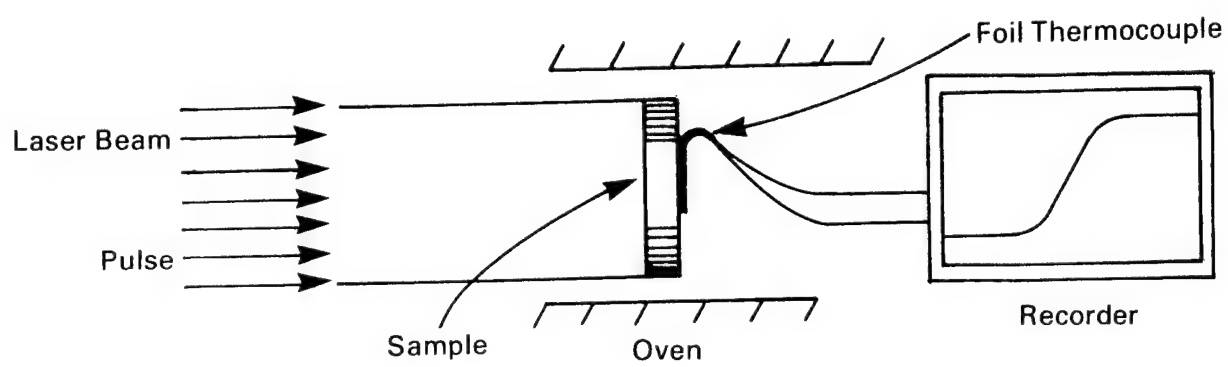


Figure A.1

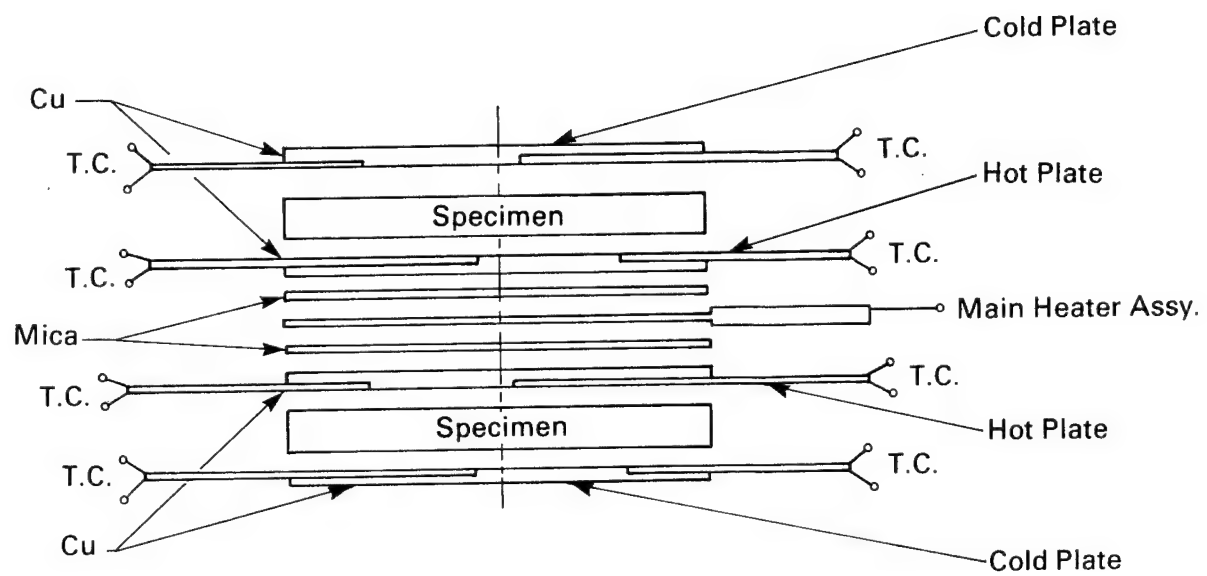


Figure A.2

$$K = qL/A(T_1 - T_2) \quad (A2)$$

where:

- K = thermal conductivity
- A = surface area of test specimens
- L = average thickness of test specimen
- q = heater input power
- T₁ = temperature of specimen cold surface
- T₂ = temperature of specimen hot surface

A-4. Differential Scanning Calorimetry: A Perkin-Elmer differential scanning calorimeter was used in this work. This instrument has two platinum alloy sample holders each of which contains a heater and a sensor. One sample holder contains the sample and the other a reference -- in this case, an empty pan. As the sample holders are heated, a high-gain closed-loop electronic system provides differential power to the heaters to keep both sample and reference sides at the same temperature. This differential power is read on a recorder directly as millicalories per second and is equivalent to the energy absorbed or evolved by the sample.

A-5. Thermogravimetric Analysis: A Perkin-Elmer TGA system was used in this study. The apparatus contains a small furnace and environmental chamber which is suspended from one arm of a microbalance. Thus, the weight change of the sample can be recorded as the sample is heated at some specified rate. This system was used to study the thermal degradation of the tread rubber and the amount of carbon black present in the tread. The first test involves heating a sample at a constant rate in a nitrogen atmosphere. The percentage weight loss was then obtained as described in the text.

The percentage of carbon black was determined by heating a sample of thread rubber in a nitrogen atmosphere at a rate of 80°C/minute to 650°C. The samples were held at this temperature until a constant weight was achieved. Oxygen was then introduced into the environmental chamber until all the carbon was oxidized and the samples had reached a constant weight. The percent weight lost in oxygen is the amount of carbon black in the rubber. Results were given in the text.

A-6. Heat Generation Rate: The heat generation rate was evaluated by loading a cylindrical sample in compression-compression fatigue. The specimen had a diameter of 13 mm (0.5 in.) and was 25 mm (1 in.) long. Loading of the sample was done between compression platens using a servohydraulic test machine under load control. Experimental details are shown in Figure A.3. The load was varied in a sinusoidal manner at a frequency of 2 Hz. The internal temperature increase of the sample was measured using an embedded thermocouple. The load-displacement response was recorded on an X-Y recorder. Additional details are available in the text.

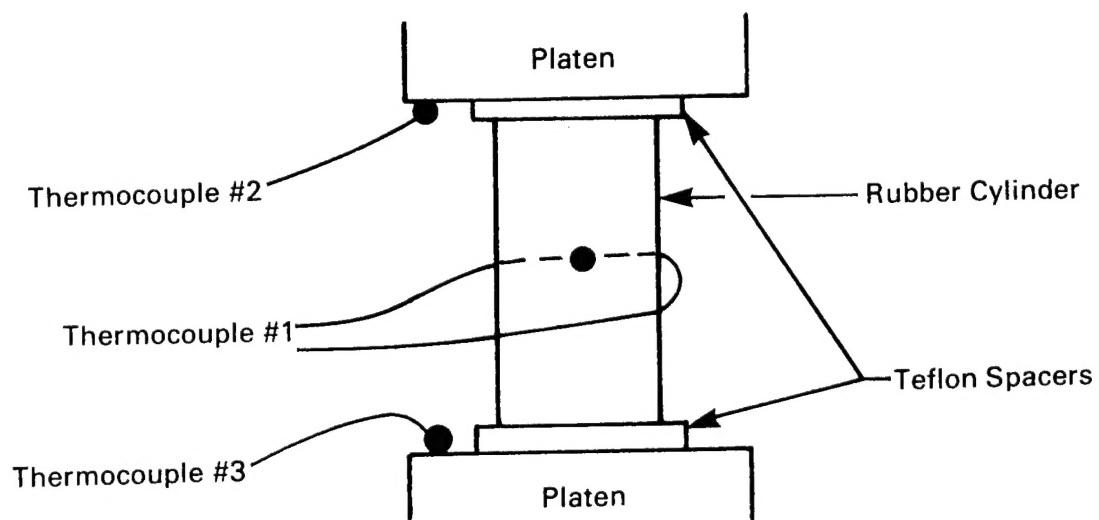


Figure A.3

APPENDIX B

CONVERSION FACTORS

The conversion factors given below should be helpful in converting the SI units appearing in the tables to English units.

Conversion Factors

<u>Quantity</u>	<u>Conversion Factor</u>
heat generation rate	$1 \text{ kW/m}^3 = 96.7 \text{ Btu/hr ft}^3$
thermal conductivity	$1 \text{ W/m } ^\circ\text{C} = 0.578 \text{ Btu/hr ft } ^\circ\text{F}$
heat transfer coefficient	$1 \text{ W/m}^2 \text{ } ^\circ\text{C} = 0.176 \text{ Btu/hr ft}^2$
pressure or stress	$1 \text{ MPa} = 1.45 \times 10^2 \text{ psi}$
velocity	$1 \text{ m/s} = 2.24 \text{ miles/hr}$
heat capacity	$1 \text{ J/kg } ^\circ\text{C} = 2.39 \times 10^{-4} \text{ Btu/lb } ^\circ\text{F}$
tear strength	$1 \text{ N/mm} = 5.71 \text{ lb/in}$
length	$1 \text{ mm} = 25.4 \text{ in}$
force	$1 \text{ N} = 0.225 \text{ lb}$
velocity	$1 \text{ mm/s} = 3.94 \times 10^{-2} \text{ in/s}$
length	$1 \text{ km} = 0.621 \text{ miles}$
density	$1 \text{ Mg/m}^3 = 62.4 \text{ lb/ft}^3$
thermal diffusivity	$1 \text{ mm}^2/\text{s} = 0.00155 \text{ in}^2/\text{s}$

DISCLAIMER

This document was prepared as an account of work sponsored by an agency of the United States Government. Neither the United States Government nor the University of California nor any of their employees, makes any warranty, express or implied, or assumes any legal liability or responsibility for the accuracy, completeness, or usefulness of any information, apparatus, product, or process disclosed, or represents that its use would not infringe privately owned rights. Reference herein to any specific commercial products, process, or service by trade name, trademark, manufacturer, or otherwise, does not necessarily constitute or imply its endorsement, recommendation, or favoring by the United States Government or the University of California. The views and opinions of authors expressed herein do not necessarily state or reflect those of the United States Government thereof, and shall not be used for advertising or product endorsement purposes.